AFIT/DS/ENP/95-04

Experimental Investigation and Computer Modeling
of Optical Switching in Distributed Bragg Reflector
and Vertical Cavity Surface Emitting Laser Structures

DISSERTATION
Richard J. Bagnell
Major, USAF

AFIT/DS/ENP/95-04

AFIT/DS/ENP/95-04

Experimental Investigation and Computer Modeling

of Optical Switching in Distributed Bragg Reflector

and Vertical Cavity Surface Emitting Laser Structures

DISSERTATION

Presented to the Faculty of the School of Engineering

of the Air Force Institute of Technology

Air University

In Partial Fulfillment of the

Requirements for the Degree of

Doctor of Philosophy

Richard J. Bagnell, B.A., B.S.E.E., M.S.E.E.

Major, USAF

December, 1995

AFIT/DS/ENP/95-04

Experimental Investigation and Computer Modeling of Optical Switching in
Distributed Bragg Reflector and Vertical Cavity Surface Emitting Laser Structures

Richard J. Bagnell, B.A., B.S.E.E., M.S.E.E.

Major, USAF

Approved:

Jeffrey W. Grantham, Capt, USAF	Date
Chairman, Advisory Committee	

Won B. Roh, Committee Member	Date
Member, Advisory Committee	

James A. Lott, Capt, USAF	Date
Member, Advisory Committee	

Dennis W. Quinn	Date
Dean's Representative	

Accepted:

Robert A. Calico, Jr.
Dean, Graduate School of Engineering

Preface

This research examined the switching capabilities of Distributed Bragg Reflectors (DBRs) and Vertical Cavity Surface Emitting Lasers (VCSELs). I was fortunate in having the opportunity to research these devices as they are relatively advanced photonic structures with wide ranging applications. The combination of experimental demonstration of switching/optical bistability and mathematical modeling of the behavior was enthralling as a research project. Both the computational problem and its real-life experimental counterpart were challenging, and both contribute to the understanding of the dynamics of the DBR/VCSEL operation.

Table of Contents

List of Figures

AFIT/DS/ENP/95-04

Abstract

The optical switching capabilities of Distributed Bragg Reflector (DBR) structures, including Vertical Cavity Surface Emitting Lasers (VCSELs) are examined. Reflectivity switching in the DBR/VCSELs is demonstrated using both thermal and carrier-generated effects to alter the mirror layers' refractive indices. Optical bistability in the DBR and VCSELs is demonstrated at room temperature, under CW photo-pumped excitation. The optical bistability is exhibited when the DBR/VCSEL is photo-pumped at the short wavelength edge of the high reflectivity band (stop band) of each device. In the DBR, reflectivity bistability is evidenced as the pump intensity is increased/decreased. The optical bistability hysteresis is controllable by spectral location of the pump on the stop band edge. In the VCSEL, which consists of a bulk GaAs gain region sandwiched by DBR mirrors, reflective bistability is also evidenced; additionally, this bistability is accompanied by a bistability in the VCSEL lasing output intensity, its laser spot size, and in its wavelength. Modeling of the DBR/VCSEL thermally-induced bistability was accomplished using an iterative, three dimensional Green's function solution to the laser-induced heat equation. The model reliably predicts thermally generated bistability, indicating a wavelength dependence, reflectivity jump, self-focusing induced spot size change, and wavelength jump commensurate with the experimental data. Reflectivity switching due to carrier effects is also demonstrated, the DBR and VCSELs exhibiting sub-picosecond switching speeds and contrast ratios of 3:1. Carrier heating, two-photon absorption, and thermal components of the reflectivity switching capabilities are examined and found to be consistent with measured nonlinear response characteristics for the refractive index in AlGaAs.

Experimental Investigation and Computer Modeling

of Optical Switching in Distributed Bragg Reflector

and Vertical Cavity Surface Emitting Laser Structures

I. Introduction

1.1 Motivation

The Air Force has been investigating the use of optoelectronics to improve warfighting capabilities for several decades. Progress in this arena is conventionally defined as an increase in the speed of the devices, decreases in their size, or decreases in their power requirements. Rapidly evolving design and fabrication technology has brought a tremendous increase in device speeds, and decreases in power requirements and size since the first devices of the mid 60's. Many of these improvements have stemmed from the incorporation of a greater ratio of optical to electronic components in the device. The development of optical components provides the optoelectronic system designer with greater flexibility; the optical solution often provides a more acceptable combination of speed, size, and power requirements than its electronic counterpart. As optical technology improves, its share of the work in the typical optoelectronic device will increase.

The capabilities of electronics switching in terms of power usage and switch speed has, until recent years, been unsurpassed. This thesis explores the optical switching capabilities of distributed Bragg reflector (DBR) structures. Explicitly, the use of optical nonlinearities in the constituents of the DBR can be used to effect an optical switch. The attributes of the switch (*e.g.* speed, power requirements) are shown to depend on the type of nonlinearity exploited. Experimentally, the ability to employ one type of nonlinearity and exclude others is demonstrated, enabling the characterization and possible future exploitation of each nonlinearity's advantages. Reflectivity switching speeds in the sub-picosecond range are demonstrated via pump-probe experiments. In addition, optical bistability

in the reflectivity of a DBR, as well as in the lasing power, wavelength, and beam divergence of a lasing VCSEL are demonstrated and mathematically modeled.

1.2 Background

1.2.1 The DBR Structure.   The root phenomenon to be examined in this research is the nonlinear response of III-V materials in the DBR structure. The construction of the DBR is key to the design of many photonic devices. Briefly, the DBR consists of a set of periodic layers, alternating high and low refractive index materials. The minor reflections at each of the interfaces (see figure 1) constructively interfere at the design wavelength, λ_d, producing a high reflectance band centered at λ_d. An example of the distinctive spectral reflectance curve is shown in figure 1, for which $\lambda_d = 920$ nm. Some of the simplest DBR designs use quarter-wave ($\lambda/4$) layers, in which each of the layers
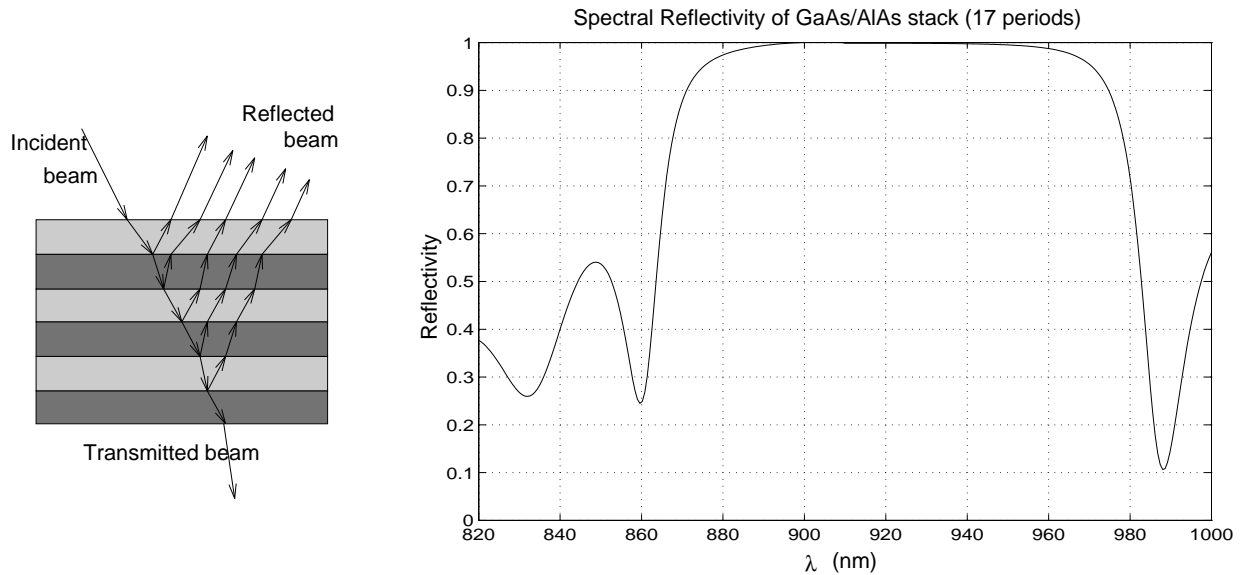
Figure 1. DBR Stack Configuration and Typical Spectral Reflectivity

is, optically, one-quarter of the design wavelength thick. In practice, exact $\lambda/4$ optical thicknesses are difficult to achieve. Often, one or both layers is aberrant. The periodicity of the layered structure, though, still attains a high reflectivity with the band centered at:

$$\lambda_d = 2\left(n_l d_l + n_h d_h\right) \tag{1}$$

2

with: $d_{l,h}$ thickness of the low/high index layers
$n_{l,h}$ index of the low/high index layers

1.2.2 The VCSEL Structure. The Vertical Cavity Surface Emitting Lasers (VCSELs) used in this thesis involve the incorporation of two DBR mirrors sandwiching a gain region. The mirrors and gain region form a laser cavity. When photo-pumped at an appropriate wavelength this cavity forms the necessary population inversion for onset of lasing. A schematic of a typical VCSEL and its spectral reflectivity is included in figure 2 below.
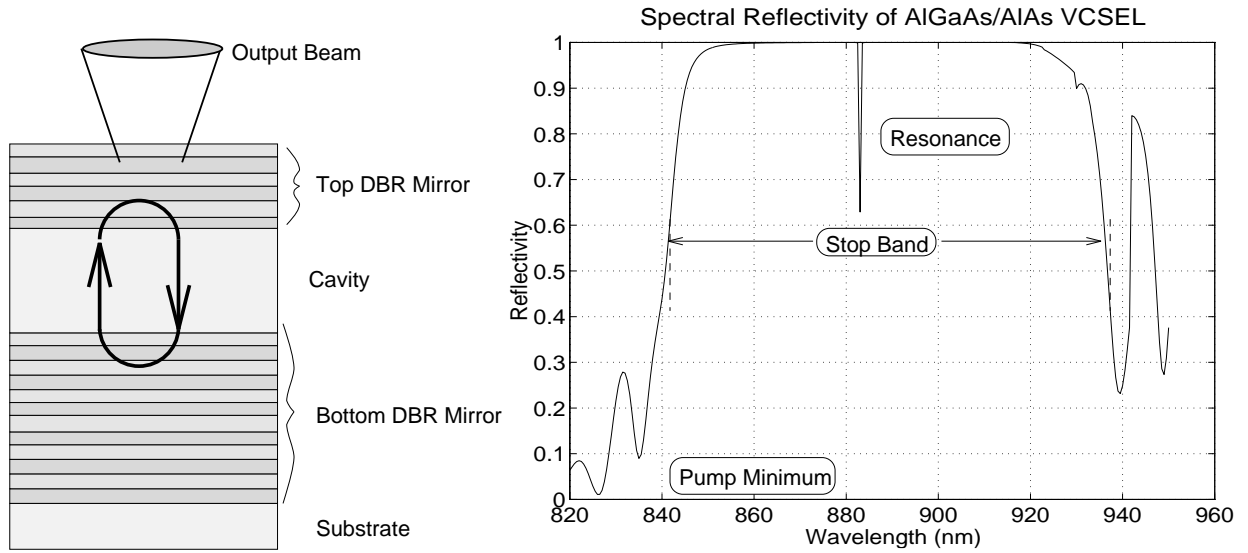
Figure 2. VCSEL Structure and Reflectivity Plot

In both the DBR and VCSEL reflectivity plots the "stop band" is known as the region of wavelengths where there is a near-constant high reflectivity. At the edges of the stop band, there is a sharp drop in reflectivity. The first minimum to the short wavelength side of the stop band is known as the pump minimum, because in photo-pumping VCSELs, the pump wavelength is usually spectrally located here, so that the energy of the pump exceeds that of the band gap of the gain region (cavity) and so that the low reflectivity allows greater penetration of pump intensity into the cavity. In the plot for the VCSEL reflectivity, the juxtaposition of the two highly reflective DBR mirrors forms a Fabry-Perot cavity, which produces the resonant dip in reflectivity (shown in figure 2 at

3

approximately 884 nm). The position of this dip is dependent on the cavity optical length, and its position selects the lasing wavelength of the VCSEL.

The calculation of the spectral reflectivity for these devices is accomplished via matrix methods to be discussed in chapter II. The primary aim of this study is that by inducing a change in the refractive index of the DBR and VCSEL mirror layers, we may switch their reflectivity at a given wavelength from low to high, or vice-versa.

1.2.3   AlGaAs Refractive Index Nonlinearities.   For the present, we can group the refractive index nonlinearities to be examined into two areas. The first we will be concerned with is the thermal nonlinear mechanism. It is driven by the heating of the semiconductor lattice by the incident pump. This heating results in a positive change in the refractive index of the materials in the DBR/VCSEL. It acts in a relatively slow manner (on the order of 1μsec). The second group are the index nonlinearities produced by the interaction of the carriers (electrons/holes) in the conduction/valence bands with each other, the semiconductor lattice, and the incident fields. These carrier-generated nonlinearities, although of a weaker nature than the thermal nonlinearity, act in a much faster time scale (from fsec to psec). The experiments to be detailed in chapter III employ the thermal nonlinearity, and those in chapter IV exploit the carrier-generated nonlinearity. The physics behind the refractive index nonlinearities explored in this research will be discussed in chapter II.

1.2.4   Optical Bistability.   A dramatic example of the capability of optical switching is the bistable optical device. A system is optically bistable if it has two stable states for a given set of input conditions. An optically bistable component has several desirable features for the device designer, including optical switching, memory, and logic gating. Alterations in the feedback of the bistable device can produce regions of differential gain (optical amplification), and output limiting (transistor action) [37].

The discovery of optical bistability in semiconductors first provided the means of incorporating an optical switch in optoelectronic devices. The first demonstration of optical bistability in GaAs etalons was found by Gibbs [16] in 1979. Since then, the bulk of the research on optical bistability has been in passive devices (see for examples, Gibbs [15]); although a segmented cavity laser (active

4

device) was proposed by Lasher as early as 1964 [27], and demonstrated a year later by Nathan *et al* [36]. As will be discussed in chapter III through chapter V, the passive bistability demonstrated and modeled in this research involves a pump intensity controlled switch from high to low reflectivity and vice-versa. The active bistability evident in the VCSEL output is shown to be driven by this passive switching capability.

Methods similar to those discussed here have been used to achieve bistability in other periodic structures [19], most notably in a hybrid DBR/linear mirror design [1], which employed a DBR mirror atop a second mirror, with a phase matching layer between. The phase matching layer and second mirror were used to enhance the fields in the DBR mirror to accentuate the nonlinear response. The switching in this research is the first demonstration of optically-controlled bistability in a non-hybrid DBR design and the first in a VCSEL.

1.2.5   Experimental Overview.   Both CW and pulsed optical excitation of the DBR and VCSELs were performed. Pulsed excitation experiments used a Coherent Mira 900 titanium:sapphire (TiS) system, configurable to emit CW, in ~2 picosecond pulses, or <200 femtosecond pulses, at a 76 MHz rate. This excitation source, in a pump-probe configuration, measured the ultrafast (carrier generated) response of the DBR/VCSELs. The experimental configuration and results for the ultrafast nonlinearities are contained in chapter IV.

The thermal nonlinear mechanism was detectable with either pulsed or CW input, however CW excitation provided many advantages: namely,

- the system input would allow steady state modeling.

- after an initial transient, the carrier-generated mechanisms would not compete with the observation of the thermal response.

- detection was simplified, as relatively inexpensive photodiodes could be used to collect the input/output of the experiment.

The experimental configurations and method of collection are discussed in chapter III. Experimental results for the DBR and VCSELs are also contained in that chapter.

5

1.2.6 Mathematical Overview. The thermally induced switching of the DBR/VCSEL was first observed at AFIT in December of 1993 as part of this dissertation work. It was encountered as sudden power surges in the output power of a sample VCSEL. The thermal nature of the phenomenon was evident, as it was controllable by temperature (on thermo-electrically cooled VCSELs), as well as input power, and wavelength. An early challenge was to see if this phenomenon could be adequately modeled to explain the multifaceted bistability in the VCSEL power surge.

The incident pump, through absorption of photons by the DBR layers, can change the individual layer refractive indices. This can occur thermally, due to phonon relaxation as the excited carriers relax in the conduction band, or by carrier generated nonlinear effects, induced by the displacement and interaction of the electron/hole populations themselves. A uniformly heated stack would produce a uniform shift in the optical path lengths of each layer, as pictured in figure 3. The red shift (shift
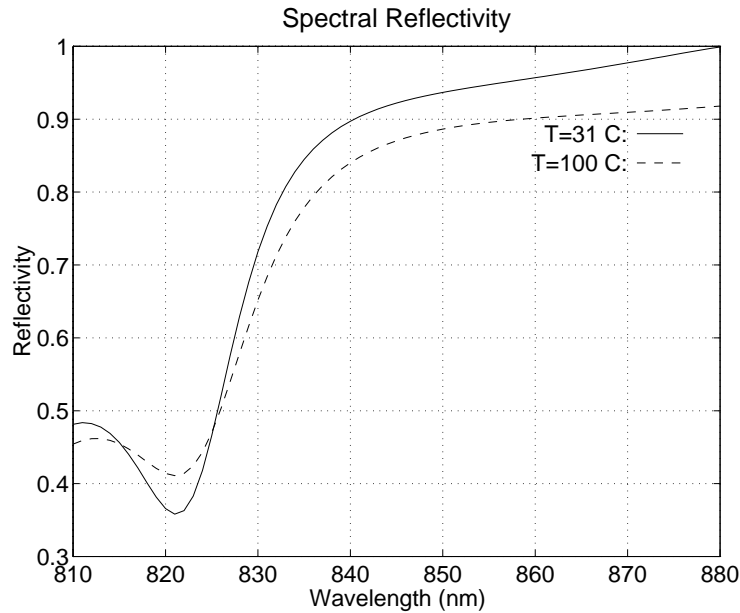
Figure 3. Spectral Reflectivity Change with Uniform Stack Heating

to longer wavelengths) is due to the refractive index change (Δn), which is positive for increasing temperatures (T). There is some thermal expansion component, which changes the physical length of the cavity, but its effect is negligible with respect to the that of Δn. The distortion of the amplitude is from the change in the extinction coefficient (Δk) which is also positive for increasing T. The

extinction coefficient is part of the complex refractive index $\tilde{n} = n + ik$; k is related to the absorption coefficient (α) for the medium through the relation: $\alpha = \frac{4\pi k}{\lambda}$ (see, for example, Pankove [39]). Both n and k are temperature dependent, and affect the reflectivity spectrum significantly.

    1.2.6.1 Nonuniform Heat Profile. The spatial profile of the field intensity in the stack is not uniform, either in the z direction (depth in the stack), or in the radial direction, because the typical pump beam has a Gaussian intensity profile. Consequently, the temperature profile can't be expected to be uniform. Calculations based on the solution to the heat equation for laser induced heating in a multi-layered structure are detailed in Chapter 4, and indicate how the centerline temperature profile depends on the make-up of the DBR layers. If the DBR layers are absorptive, the temperature is elevated near the surface. If they are non–absorptive and the substrate is absorptive, the heating propagates up from the substrate, elevating the temperature of the lower layers. Three temperature distributions for a DBR mirror with absorptive layers are shown in figure 4 as well as their resultant spectral reflectivity profiles. The uniform temperature distribution is a constant 100° C; there is a tapered profile which averages 100° C over the layers; and a third distribution which tapers to 100° C at the substrate. An assumed Gaussian taper was used for these calculations as an example of the influence of the tapered temperature profile's effect on the reflectivity. The GaAs/AlAs stack of 34 layers, heated by an 838 nm focused pump beam, has a structure similar to that used in the experiment. The difference in spectral profiles indicates the temperature distribution can appreciably alter the spectral reflectivity of the stack. At the pump wavelength, 838 nm, at room temperature, $R = .89$ (see figure 3). The reflectivity at that wavelength falls to $R = .79$ for uniform heating of the structure, but the fall is a larger for tapered heat: $R = .72$.

    One difficulty in constructing a mathematical model for the heating of the mirror stack is presented by its resonant structure. A plot of the electric field structure in the DBR is shown in figure 5. The two distributions shown are taken at the wavelengths corresponding to the peak of the DBR reflectivity (middle of the stop band) and at the pump minimum. It is easy to infer that the tapered profile in figure 4 is likely closer to the real heat profile in the DBR than a uniform heat distribution, although the Gaussian taper is not a precise match to the real heat profile either. The
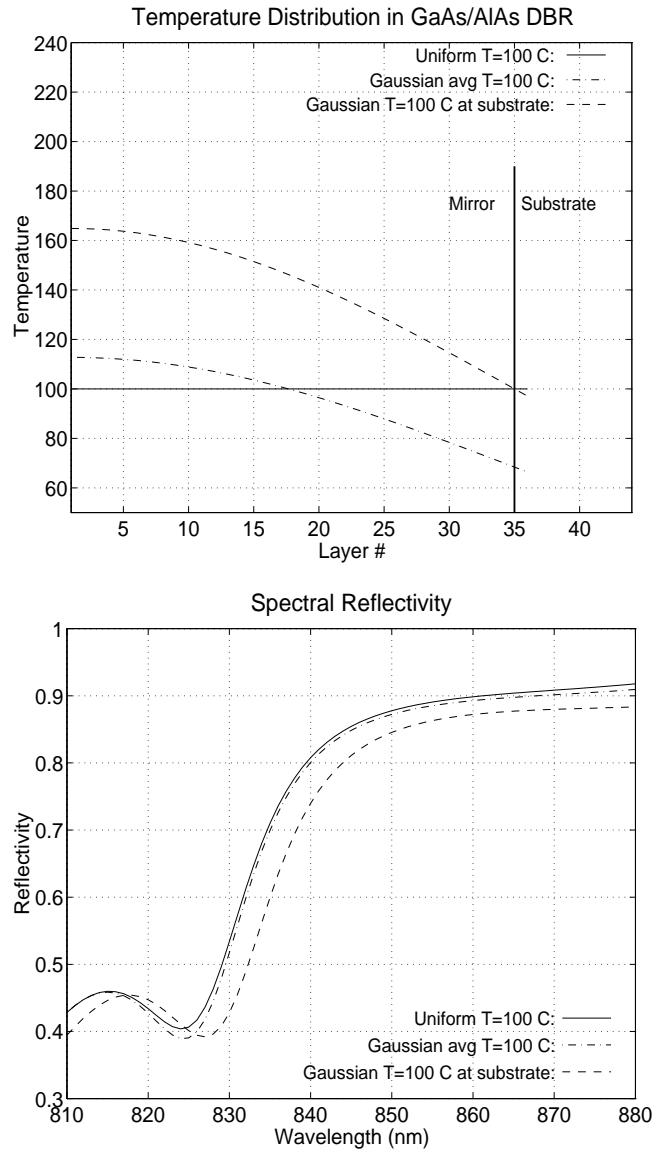
Figure 4. Effect of Various Temperature Distributions on Spectral Reflectivity of a DBR Mirror

field distribution at the pump minimum (see figure 5 bottom) is not a strictly decreasing taper and it is the stack's absorption of these fields coupled with the heat propagation between layers that produces the heat profile. The nonuniform intensity of the fields in each mirror layer means the absorption of the pump will be nonuniform, and consequently, so will the laser-heating in the layers. The resultant nonuniform temperature distribution individually alters the index in each layer, shifting and warping the spectral reflectivity curve.

Field Strength in DBR mirror at λ_{design}

Mirror   Substrate

Field strength (normalized to incident)

Layer #

Field Strength in DBR mirror at $\lambda_{pump\ min}$

Mirror   Substrate

Field strength (normalized to incident)

Layer #
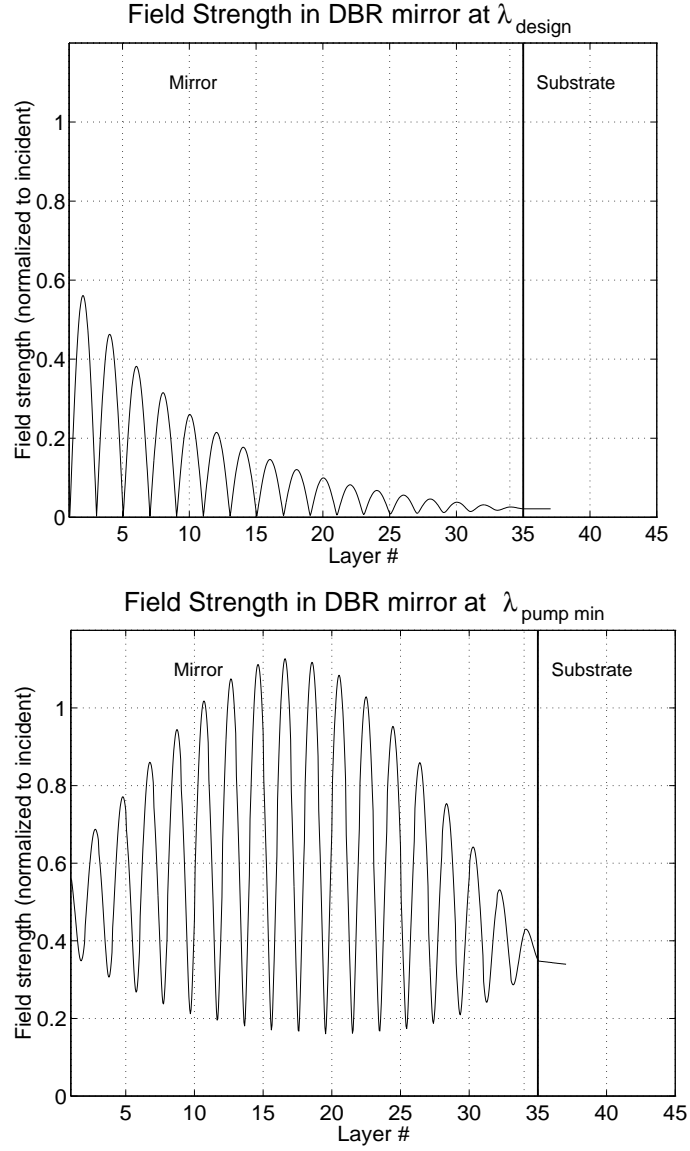
Figure 5. Electric Field Distribution in DBR

1.2.6.2   Thermal Lensing.   An additional mathematical model complication is the radial profile of the heating. In the VCSEL, which is a more complicated structure than the DBR, the bistability presents itself as more than a mere reflectivity change. Photo-pumping the VCSEL at the wavelengths concerned produces a lasing output in the VCSEL; and the reflectivity switch from high reflectivity to low produces a sudden increase in the pump intensity reaching the gain region/cavity. As this higher pump intensity is absorbed, the cavity temperature increases, producing a positive

9

index shift in the cavity ($+\Delta n$). This accounts for the power surge and the detectable wavelength shift (up to $+$ 9 nm) in the output of the VCSEL. There is also evident a change in the spot size emitted from the VCSEL. The spot size jump was attributed to the radial temperature profile of the photo-pumped VCSEL. The Gaussian intensity profile of the pump input induces a Gaussian-like heat profile in the mirror layers and cavity. The refractive index distribution results in a self-focusing in the VCSEL, tightening the focus of the incident pump, and increasing the pump intensity per unit volume in the gain region.

The radially symmetric pump profile, coupled with the nonuniform field distribution/absorption as the pump penetrated the DBR/VCSEL prompted the necessity of the use of a model which accounted for the time-dependent heating of a multi-layer structure in two-dimensions. Fortunately, this type of problem is common to many current interests, as it is nearly the same as that for designers of magneto-optic disk recording systems [42], and photothermal deflection experimenters [34]. An additional complexity is added in this problem: the temperature dependence of many of the material parameters (refractive index, thermal conductivity, diffusivity, absorption) must be incorporated to allow the nonlinear mechanism to describe the bistable response. Chapter V describes the Green's function solution to this problem, and the resultant mathematical verification of the heat-induced bistability in the DBR/VCSEL structures.

1.3   Presentation

Chapter II reviews the mechanisms for refractive index nonlinearities. The experimental results for the thermally induced optical switching are contained in chapter III for the DBR mirror and for the VCSELs. The carrier-generated optical switching along with the pump-probe method of collection is discussed in chapter IV. Chapter V contains an explanation of the mathematical model for the thermally-induced bistable switching behavior. Conclusions and future avenues to be researched are laid out in chapter VI.

II. **Optical Properties of the Al$_x$Ga$_{1-x}$As DBR/VCSEL Structures**

This chapter collects several topics which help to explain the physical processes responsible for the optical switching behavior observed in the experimental and mathematical modeling of the DBR/VCSELs in this research. A description of the DBR structure and the method used for calculating its spectral reflectivity is first undertaken. From this discussion, it is readily apparent that the refractive index of the constituent layers is critical to the response of the structure. Methods for manipulating the refractive index by influencing the gain spectrum by thermal means and by electronic means are then discussed. Finally, simplified models for the refractive index behavior in Al$_x$Ga$_{1-x}$As due to thermal and carrier-generated optical processes are introduced. These models help to explain the experimental results in chapters III and IV.

2.1   The DBR Structure and Reflectivity

We are interested in the response of the DBR stack to an incident "pump" beam (see figure 6). The reflectivity of the stack is an easily obtained externally measurable parameter, requiring only the measurement of incident light (I_{in}) and reflected light (I_r), and determining the ratio of the two at the given wavelength. The methods for calculating the wavelength-dependent reflectivity of the DBR stack are well established [31]. Typically referred to as the matrix method, this model provides not only the spectral reflectivity of the stack, but can be used to determine the field distribution inside the stack. This distribution will be essential to estimating the nonlinear response of the DBR layers to the excitation.

2.1.1   Field Calculations.   We begin by approximating the focused pump beam in figure 6 as normally incident. We follow the matrix approach as described by Grosse & Wynands [17]. In calculating the field distribution [17] in the DBR (see figure 7), the matrix approach starts with the construction of a mathematical expression for the counter-propagating waves in the stack at an interface:

$$\begin{pmatrix} E_{j-1}^{(+)} \\ E_{j-1}^{(-)} \end{pmatrix} = \frac{1}{\tau_{j-1,j}} \begin{pmatrix} 1 & \rho_{j-1,j} \\ \rho_{j-1,j} & 1 \end{pmatrix} \begin{pmatrix} E_j^{(+)} \\ E_j^{(-)} \end{pmatrix} \tag{2}$$
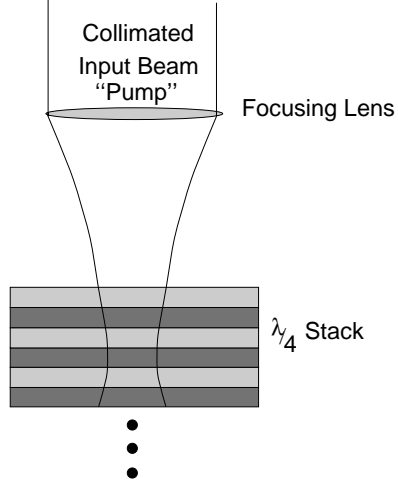
Figure 6. Collimated Pump Input Beam Incident on DBR Stack

with: $\rho_{i,j} = \frac{\tilde{n}_i - \tilde{n}_j}{\tilde{n}_i + \tilde{n}_j}$, $\tau_{i,j} = \frac{2\tilde{n}_i}{\tilde{n}_i + \tilde{n}_j}$ being the Fresnel amplitude reflection and transmission coefficients for the electromagnetic wave, at perpendicular incidence from medium i to j; and the complex refractive index, $\tilde{n} = n + ik$. For the remainder of this dissertation, we will refer to the real part of $\tilde{n}$ as the refractive index (n) and the imaginary part as the extinction coefficient (k).
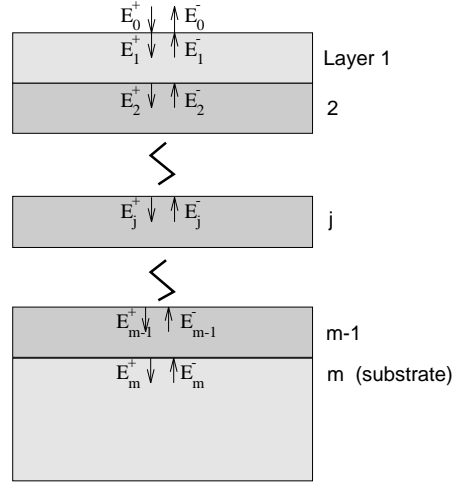
Figure 7. Geometry for Field Calculations in DBR

In this manner, the fields incident at one side of the thin-film interface are related to those at the other. Multiplying by a matrix representing the phase and amplitude change the waves undergo as they traverse each layer, we can describe the field arriving at the opposite interface:

$$
\begin{pmatrix} E^{(+)} \\ E^{(-)} \end{pmatrix}_{z=0} = \begin{pmatrix} \phi^{-1}(d) & 0 \\ 0 & \phi(d) \end{pmatrix} \begin{pmatrix} E^{(+)} \\ E^{(-)} \end{pmatrix}_{z=d}
\tag{3}
$$

d being the layer thickness, and $\phi(z) = e^{i 2\pi(n+ik)z/\lambda}$ the phase and amplitude change in traversing the layer. By cascading these matrices we may describe the relationship of the fields entering the stack in terms of the fields exiting (into the substrate):

$$
\begin{aligned}
\begin{pmatrix} E_0^{(+)} \\ E_0^{(-)} \end{pmatrix} &= \frac{1}{\tau_{01}} \begin{pmatrix} 1 & \rho_{01} \\ \rho_{01} & 1 \end{pmatrix} \begin{pmatrix} \phi_1^{-1}(d_1) & 0 \\ 0 & \phi_1(d_1) \end{pmatrix} \\
&\quad \cdots \frac{1}{\tau_{m-1,m}} \begin{pmatrix} 1 & \rho_{m-1,m} \\ \rho_{m-1,m} & 1 \end{pmatrix} \begin{pmatrix} E_m^{(+)} \\ E_m^{(-)} \end{pmatrix} \\
&= \begin{pmatrix} T_{11} & T_{12} \\ T_{21} & T_{22} \end{pmatrix} \begin{pmatrix} E_m^{(+)} \\ E_m^{(-)} \end{pmatrix}
\end{aligned}
\tag{4}
$$

If we now divide by the incident wave's amplitude $E_0^{(+)}$ and recognize that in the substrate there is no reverse traveling field ($E_m^{(-)} = 0$):

$$
\begin{pmatrix} 1 \\ r_{0m} \end{pmatrix} = \begin{pmatrix} T_{11} & T_{12} \\ T_{21} & T_{22} \end{pmatrix} \begin{pmatrix} t_{0m} \\ 0 \end{pmatrix}
\tag{5}
$$

$r_{0m} = \frac{E_0^{(-)}}{E_0^{(+)}}$ is the amplitude reflection coefficient and $t_{0m} = \frac{E_m^{(+)}}{E_0^{(+)}}$ the amplitude transmission coefficient; solving equation 5 for these produces $t_{0m} = 1/T_{11}$ and $r_{0m} = T_{21}/T_{11}$. To determine the power reflectivity, we can take $|r_{0m}|^2$. This result is very useful: to calculate the field anywhere in the stack, we multiply all the transfer matrices from layer m back to the layer of interest, producing a 2×2 matrix M, and at position z in this j^{th} layer, the normalized fields are:

13

$$\begin{pmatrix} \alpha_j(z) \\ \eta_j(z) \end{pmatrix} = \begin{pmatrix} \phi_j(z-d_j) & 0 \\ 0 & \phi_j(-z+d_j) \end{pmatrix} \cdot M \cdot \begin{pmatrix} t_{0m} \\ 0 \end{pmatrix} \tag{6}$$

d_j being the thickness of the jth layer and z the position in that layer as measured from its top surface. The fields at point z are then determined by $E_0^{(+)}\alpha_j(z)$ (the forward travelling wave) and $E_0^{(+)}\eta_j(z)$ (the backward travelling wave). An example of the calculation of the fields in the DBR at varying wavelengths was provided in chapter I, figure 5. In the VCSEL, the added resonance provided by the cavity/gain region further perturbs the field distribution. Examples of its field distribution are shown in figure 8, at the pump minimum ($\lambda = 839$ nm), short wavelength edge of the stop band ($\lambda = 842$ nm), and design resonance ($\lambda = 884$ nm). It is evident from these plots that the spectral location of the pump on the reflectivity plot can present very different field distributions as the changing index profile shifts/warps the reflectivity curve.

2.1.2   Influence of Refractive Index on Spectral Reflectivity.   The layers of a distributed Bragg reflector can be likened to a cascaded set of Fabry-Perot resonators. In a single Fabry-Perot cavity, the optical path length of the cavity plays the dominant role in its response [18]. The optical path length in the presence of nonlinearities is given by:

$$\frac{\Delta(nD)}{nD} = \frac{1}{n}\frac{\partial n}{\partial N}\Delta N + \left(\frac{1}{n}\frac{\partial n}{\partial T} + \frac{1}{D}\frac{\partial D}{\partial T}\right)\Delta T \tag{7}$$

with:

$$\begin{array}{rl} nD & \text{optical path length (n refractive index)} \\ T, \Delta T & \text{temperature, change in temperature} \\ D & \text{physical path length} \\ N, \Delta N & \text{carrier population, change in carrier population} \end{array}$$

The first term on the right hand side of equation 7 results from the change in carrier population and its effect on the refractive index $\partial n/\partial N$. The second term accounts for the change in index with temperature, and is generally several orders of magnitude larger than the third term, which reflects the change in the physical length of the cavity from thermal expansion [7]. In actuality, this equation is both dispersive and absorptive, as the temperature increase (and its index change) is produced from
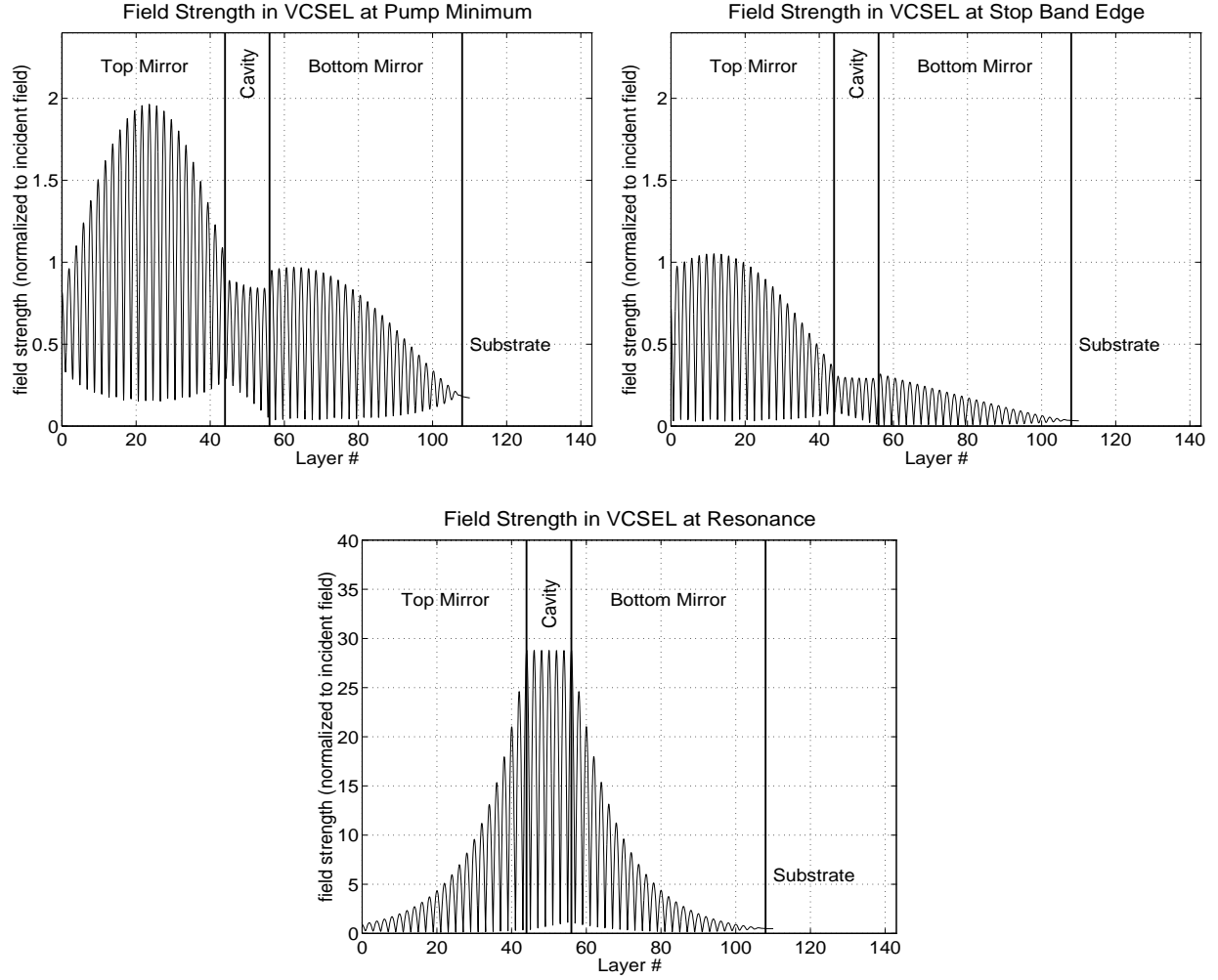
Figure 8. Field Distribution in VCSEL at Various Wavelengths

the absorption of the incident light. We are most interested in this study in describing the processes affecting the terms $\frac{\partial n}{\partial N}$ and $\frac{\partial n}{\partial T}$.

2.2 *Gain in AlGaAs*

Studying the gain behavior of AlGaAs under excitation can lead to a better grip on the behavior of the refractive index in this semiconductor. The development of the gain expression as a function of energy is well established [8, 26]. For now, we are most concerned with how the gain is affected by temperature, addition of carriers, and varying x concentrations in the ternary $Al_xGa_{1-x}As$. The

expression for gain in this system is [8]:

$$g(E) = -\alpha(E) = \frac{\pi e^2 \hbar}{\epsilon_0 m_v m_c c n E} \int_{-\infty}^{\infty} \rho_c(E_1 + E) \rho_v(E_1) |M|^2 \left(f_c(E_1 + E) - f_v(E_1) \right) dE_1 \quad (8)$$

with:

e	electron charge
h	Planck's constant
$\hbar$	$h/2\pi$
ϵ_0	permittivity of free space
m_c, m_v	effective masses of the electrons (m_c), and holes (m_v)
n	refractive index at gap energy
$|M|$	Momentum matrix element
ρ_v, ρ_c	density of states for the valence (ρ_v) and conduction (ρ_c) bands
f_c, f_v	Fermi functions for the respective bands

M, the momentum matrix element, describes the coupling strength between the wavefunctions of the upper and lower states of the transition [8]. The densities-of-states (ρ_v, ρ_c) for bulk semiconductors are given by:

$$\rho_c(E - E_c) = \frac{1}{2\pi^2} \left(2m_c/\hbar^2 \right)^{3/2} \sqrt{E - E_c} \qquad E \geq E_c$$

and ...

$$\rho_v(E_v - E) = \frac{1}{2\pi^2} \left(2m_v/\hbar^2 \right)^{3/2} \sqrt{E_v - E} \qquad E \leq E_v \qquad (9)$$

...where E_c is the conduction band minimum, and E_v the valence band maximum. The dependence of the gain on the energy gap $E_c - E_v$ is apparent through these equations; for values of E less than E_c, $\rho_c( ) = 0$, while $\rho_v( ) = 0$ for values of E greater than E_v. As a result, these forbidden energies produce no gain. The Fermi functions represent the probability that a state in the conduction/valence band is occupied. Their form is:

$$f_c(E, T_c) = \frac{1}{1 + e^{(E - \mu_c)/kT_c}} \qquad f_v(E, T_v) = \frac{1}{1 + e^{(E - \mu_v)/kT_v}} \qquad (10)$$

...T_c and T_v being the carrier temperatures in the conduction/valence bands, and μ_c, μ_v, the quasi-Fermi energies. In calculating the gain spectrum, these quasi-Fermi energies are first determined.

Assuming a carrier density in the conduction band N_c, the quasi-Fermi energy μ_c may be obtained via :

$$N_c = \int_{-\infty}^{\infty} \rho_c \left(E - E_c \right) f_c(E, T_c) dE \tag{11}$$

Solving this relation for μ_c provides the desired quasi-Fermi level. In a similar manner, μ_v may be obtained for the hole population N_h:

$$N_h = \int_{-\infty}^{\infty} \rho_v \left(E_v - E \right) f_v(E, T_v) dE \tag{12}$$

A typical gain curve is shown in figure 9 below. The curve represents calculations for GaAs. Below the gap energy, E_g, the gain is zero, indicating the medium is transparent to these photon energies. Above E_g the gain is positive for a limited spectrum, and the medium exhibits stimulated emission here. For higher energies still, the gain spectrum becomes negative, indicating for these energies, the medium is absorptive.
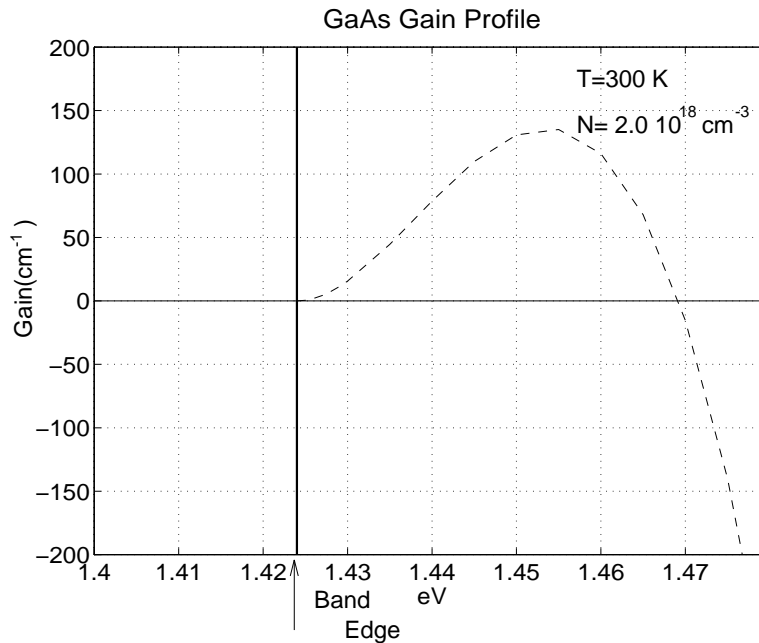
Figure 9. Calculated GaAs Gain Profile

17

Increasing the carrier densities in the conduction and valence bands further populates the energy states in the band, increasing the average energy of the states available for transition (quasi-Fermi energies), broadening the spectrum for positive gain and increasing the gain at each energy (see figure 10(left)).
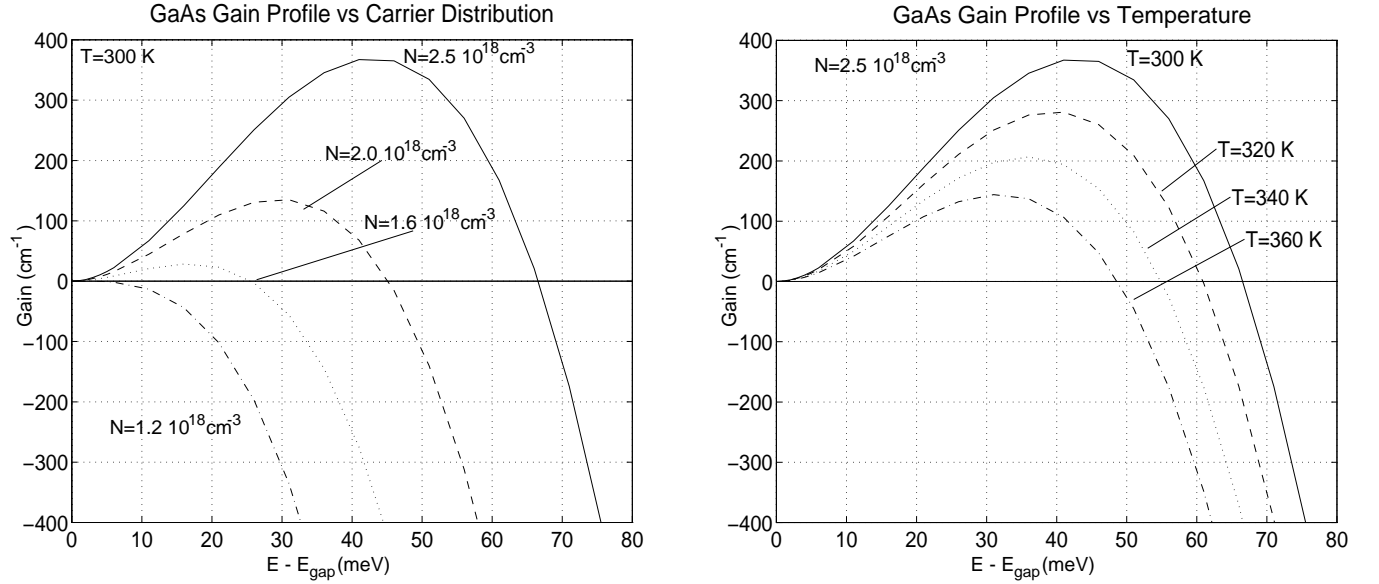
Figure 10. Effects of Carrier Density and Temperature

Raising the temperature of the carriers tends to compress the gain, as can be seen in figure 10(right). The effect of temperature change is to modify the energy spectrum at the bottom of the conduction/top of the valence band, smearing the energies, and lowering the densities of states at energies near E_g, which spectrally compresses the gain.

2.3 Kramers-Krönig Relations

The gain/absorption changes described in the previous example impact the refractive index in the material. The relationship between the absorption and refractive index is expressed by the Kramers-Krönig relations (see, for example, Pankove [39]):

$$n(E) - 1 = \frac{c\hbar}{\pi} P \left\{ \int_0^\infty \frac{\alpha(E')}{E'^2 - E^2} dE' \right\} \tag{13}$$

Where the symbol $P\{\ \}$ indicates the principal value is to be taken. The energy (E) in the equation refers to the photon energy, which relates to the wavelength by $\lambda = ch/E$. $n(E)$ is the refractive index, whose dependence on the energy, also called dispersion, is evident from the equation. $\alpha(E)$ is the absorption coefficient, which is related to the gain by $g(E) = -\alpha(E)$, c is the free space speed of light, h is Planck's constant and $\hbar = h/2\pi$. We are interested in the change in the index of refraction, $n_1(E) - n_2(E) = \Delta n(E)$. Using the gain $(g(E) = -\alpha(E))$ expressions for equation 13:

$$
\begin{aligned}
(n_2(E) - 1) - (n_1(E) - 1) &= \frac{c\hbar}{\pi} P \left\{ \int_0^\infty \frac{-g_2(E') + g_1(E')}{E'^2 - E^2} dE' \right\} \\
\Rightarrow n_2(E) - n_1(E) = \Delta n(E) &= -\frac{c\hbar}{\pi} P \left\{ \int_0^\infty \frac{\Delta g(E')}{E'^2 - E^2} dE' \right\}
\end{aligned}
\tag{14}
$$

The important result of equation 14 is that, although there is no gain change for energies below the band edge, the relationship of the refractive index $n(E)$ is to the *entire* gain spectrum. This means there can be changes in Δn at energies below the band edge from gain/absorption changes above the band edge. For example, we can compute the change in refractive index for the temperature dependent gain profiles in figure 10. Pictorially, the gain/absorption changes and calculated index changes are shown in figure 11.

Note that the index has changed at energies below the band edge, even though the gain has not. The rise in temperature has compressed the gain curve, thus the gain change Δg is negative. The Kramers-Krönig relation, applied to this $\Delta g(E)$ curve, indicates a positive index change near and below the band edge. The increase in carrier temperature increases the refractive index at these energies. In a similar manner, the changing carrier density produces a decrease in the refractive index, as (Δg) in equation 14 is positive for increasing carrier concentration. For energies near and below the AlGaAs band gap, this positive change in Δg produces a negative refractive index change.

2.4 Thermal Dependence of the Refractive Index in AlGaAs

Although the Kramers-Krönig relations and gain theory provide insight into the general behavior of the $Al_x Ga_{1-x} As$ refractive index, it is useful to have a computationally simple method of determining the index of refraction for the $Al_x Ga_{1-x} As$ mirror layers at any x concentration near
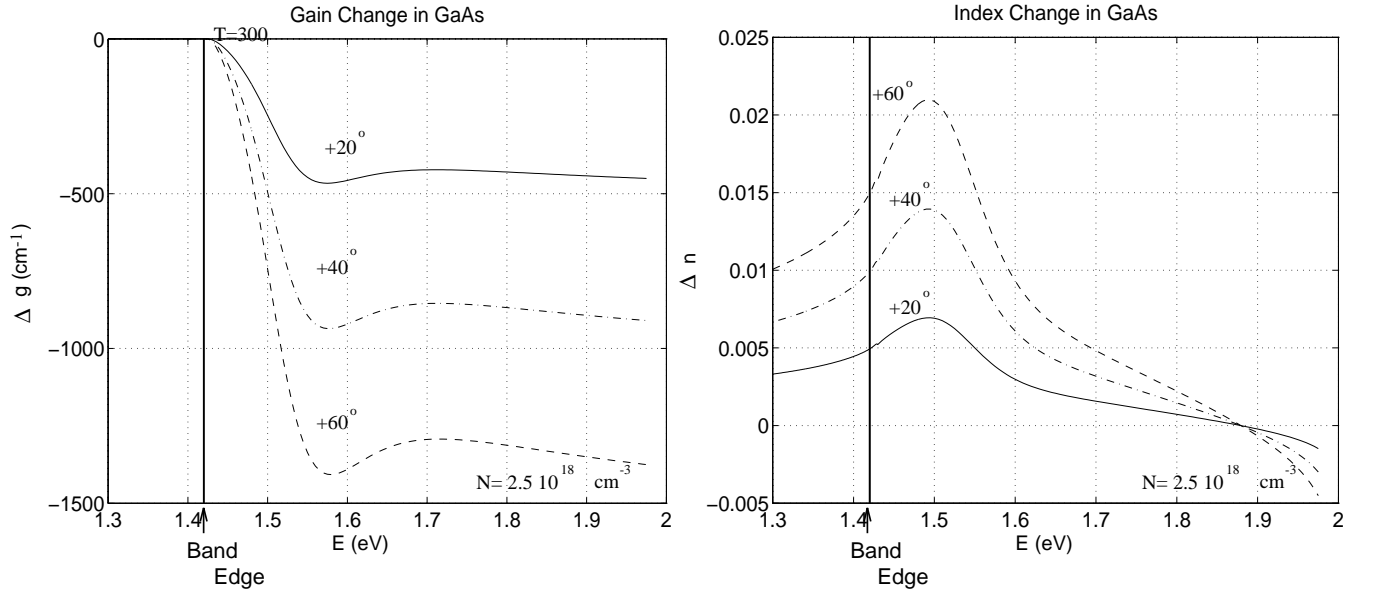
Figure 11. Effects of Temperature Increase on Gain and Refractive Index

room temperature. For GaAs, fortunately, recent ellipsometry measurements were available from experiments conducted by G.N. Maracas at Arizona State University [32]. The ellipsometry data was used to calculate both n and k for GaAs from 31C to 600C for energies ranging from 1.24 eV to 4.9 eV. No such data was available for the ternary. However, for energies below the material band gap, an approximation for the temperature dependence of the refractive index can be inferred through a method adapted by Dudley *et al* [11] from the single effective oscillator (SEO) model. Afromowitz [3] proposed the SEO model to predict the refractive index of semiconductors below the band edge. His model predicted the index via the equation:

$$n(E)^2 - 1 = \frac{E_d}{E_0} + E^2 \frac{E_d}{E_0^3} + \frac{E^4 E_d}{2 E_0^4 (E_0^2 - E_\Gamma^2)} \ln \left[\frac{2 E_0^2 - E_\Gamma^2 - E^2}{E_\Gamma^2 - E^2} \right] \qquad (15)$$

E_0 and E_d are the oscillator (SEO) parameters as described by Wemple and DiDomenico [43], E_Γ is the energy gap, and E is the photon energy. Dudley *et al* [11] modeled the temperature shift's effect by taking the derivative with respect to temperature of equation 15, and assuming parameter E_d is not dependent on the temperature.

20

$$\frac{\partial n}{\partial T} = \frac{\partial n}{\partial E_\Gamma}\frac{\partial E_\Gamma}{\partial T} + \frac{\partial n}{\partial E_0}\frac{\partial E_0}{\partial T} \tag{16}$$

This method was applied to GaAs and AlAs by Dudley. The values for the parameters used in those calculations are tabulated in table 1 below. Dudley apparently used a linear interpolation in his scheme to determine values for AlAs from parameters for GaAs for $\partial E_\Gamma/\partial T$, and $\partial E_0/\partial T$. In this respect, a similar linear interpolation for $Al_x Ga_{1-x} As$ parameters is used for calculations in this report. The results, for small temperature increases, are very good; figure 12 below compares the results of the SEO model to those obtained by Maracas' ellipsometry measurements. The indications, for both GaAs and AlAs, are that the SEO model tracks the measured ellipsometry data very well for temperatures approaching 400° C.

Table 1. Parameters used in Calculating dn/dT (after Dudley *et al*)

	E_Γ [eV]	E_0 [eV]	E_d [eV]	$\partial E_\Gamma/\partial T$ [$10^{-4}eV/°C$]	$\partial E_0/\partial T$ [$10^{-4}eV/°C$]
GaAs	1.424	3.650	36.10	3.9	5.2
AlAs	2.950	4.70	33.65	5.2	6.9
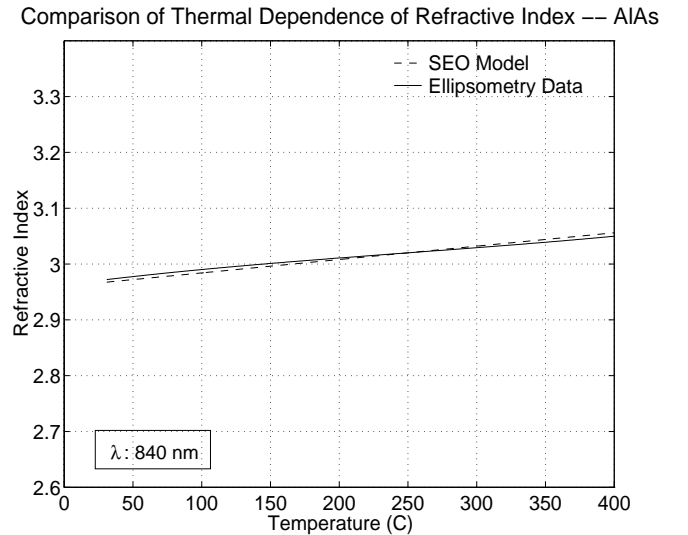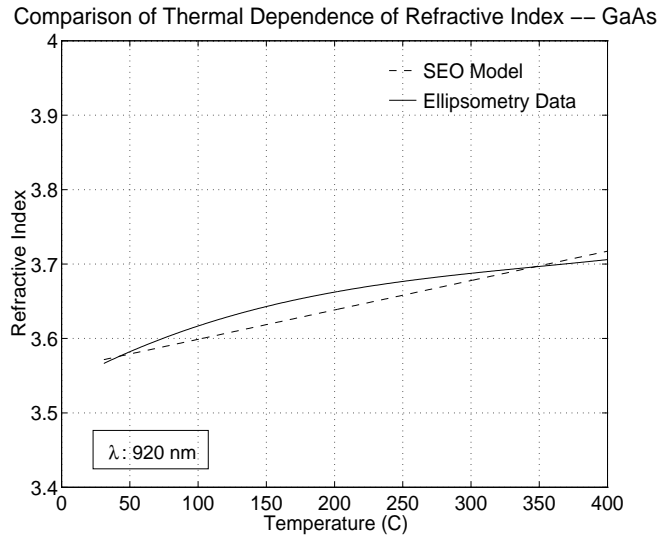
Figure 12.   Comparison of SEO Model for Temperature Dispersion to Ellipsometry Data for GaAs/AlAs

21

As can be seen from the plots, the model works well for below band AlAs and GaAs temperature dispersion. For the computations used in this thesis, however, the model was only applied when the wavelength used was located below the band edge. Ellipsometry data [32] were used for all GaAs index of refraction values, because the wavelengths used on the devices were above the GaAs band edge, where Dudley's model is not strictly valid.

2.4.0.1   Extinction Coefficient.   The extinction coefficient is less well documented for the ternary $Al_xGa_{1-x}As$. However, for GaAs, the ASU ellipsometry data, as well as tabulated data [38] were used to discern the extinction coefficient wavelength-dependence and thermal-dependence. For non-zero x concentrations, equations to determine k have been developed by Jenkins [22] and Adachi [2] for the wavelength-dependence, but no thermal data or expressions are available in the research. Fortunately, for the pump wavelengths used herein, the non-zero x concentration $Al_xGa_{1-x}As$ materials used had absorption energies well above the pump energy, so that k was negligible for $x \neq 0$ and was assumed to remain negligible as T increased.

2.5   Carrier Dependence of the Refractive Index in AlGaAs

The carrier generated nonlinearities explored later in this thesis have more diverse sources than the thermal effect. Figure 13 illustrates excitation processes in the ternary. For the present, the gaps are illustrated as direct, although the $Al_xGa_{1-x}As$ system has indirect gaps for high x values ($x > 0.6$).

The multi-layer structures employed in this thesis required that, for any reasonable excitation scheme, there would be multiple nonlinear effects. For some layers, the incident pump energy would be above the gap energy, while for others, below band excitations were involved. For example, the DBR consisted of AlAs and GaAs layers. The spectral location of the pump was at the short wavelength edge of the stop band. For the DBR, this was ~ 830 nm. This pump wavelength equates to an energy above the GaAs band edge, and below the AlAs band edge.

2.5.1   Index Nonlinearities.   Experimentally, a simple way to discern the various nonlinear effects present in the semiconductor environment is to group them by time-scale. The various time-scales are femtosecond, picosecond, nanosecond, and microsecond; they are addressed as follows.

2.5.1.1   Femtosecond Scale.

Above-Band Processes.   For energies above the band edge, the dominant optical process is *stimulated transitions* (both *stimulated emission* and *absorption*). This process is
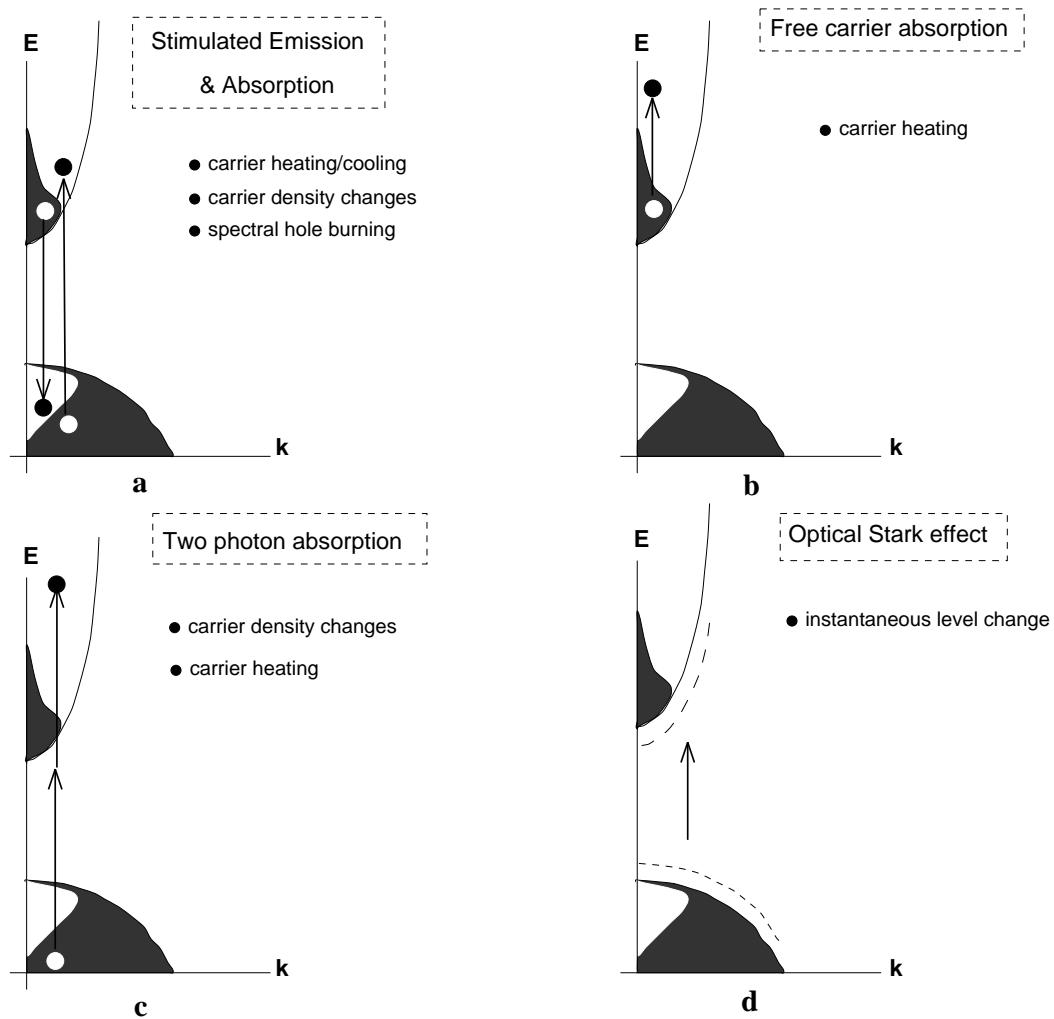
Figure 13.   Effects of Optical Processes on the Carrier Dynamics in Semiconductors (After Hultgren)

pictured in figure 13a. The addition of carriers to the bands drives a decrease in absorption (increase in gain) and produces a negative change in index. *Spectral hole burning* is nearly instantaneous ($<$ 100 fsec) and results from the delay in relaxation of the promoted carriers to lower energies. These carriers momentarily remain in a narrow spectrum matching that of the pump; before they relax they form a transient gain increase [20] producing a negative transient in the index. The *optical Stark effect* (Figure 13d) is an instantaneous response of the carriers in the bands to the electric fields (the incident pump). Its speed, and the limitations of the pulsed input in the pump-probe experiments, preclude discriminating it from other processes with the experimental configuration used in this research.

Below-Band Processes. *Two photon absorption* (Figure 13c) is the process by which below-band pump photons may promote carriers to the conduction band via virtual levels. Thus the energies of two photons combine to effect the interband transition. As for absorption, the result is a carrier density increase, which relaxes on the nsec time scale, and produces a negative index shift. The *optical Stark effect* is also present as a below the band edge process. It has, however, a resonant behavior and is much stronger as the pump wavelength approaches the band edge.

2.5.1.2 Picosecond Scale. For both above and below band excitation, the promotion of carriers into the conduction/valence bands is accompanied by phonon relaxation of the carriers to the bottom of the band. This phonon relaxation has near-immediate and long-term effects: the immediate effect is that the carriers at the bottom of the band can be excited by the phonons. This process is called *carrier heating*, it raises the effective temperature of the band and it abates on a psec time scale [20]. Along with carrier heating, the pump may promote carriers to levels below the quasi-Fermi levels; in doing so, it effectively lowers the average temperature of the band. This process is termed *carrier cooling* and usually only occurs for above band excitation. This is because two-photon absorption will deposit its carriers high into the bands, so that the effective temperature is nearly always raised (carrier heating). Carrier cooling is difficult to discern in photo-pumped experiments because it competes with carrier heating. It has been observed in electrically-pumped devices which establish an elevated carrier population and then undergo photo-pumping. *Free carrier absorption* involves the absorption of pump photons by free carriers in the valence/conduction bands (see figure 13b).

In experiments with electrically pumped AlGaAs waveguides, Hultgren [20] simultaneously photo-pumped the waveguides to determine their gain and index response (with pump–probe techniques). He found that it was possible to control the magnitude of the carrier heating $(+\Delta n)$ contribution by increasing/decreasing the current. He attributed this result to an elevated free carrier population undergoing free carrier absorption of the pump, and adding to the carrier heating of the sample. This method suggests the index/reflectivity response of the DBR can be controlled at the picosecond time scale by injecting carriers.

2.5.1.3 Nanosecond Scale. Although the experimentation in chapter IV focuses on the picosecond time scale nonlinearities, it is important to note there are effects which govern the nanosecond response of the system. The *carrier density changes* relax on a time scale governed by the recombination rate of the material (~ 1 nanosecond for $Al_xGa_{1-x}As$). This relaxation depletes the gain, thus raising the refractive index $(+\Delta n)$. *Band filling* involves the filling of states at the bottoms of the bands as the promoted carriers relax. These filled states drive absorption down, which forces a negative index change. In GaAs, band filling begins to affect the absorption spectrum on the picosecond time scale, and relaxes on the nanosecond time scale. In *bandgap renormalization*, the interaction of the excited carriers works to redistribute the filled states to lower the band's energy configuration. This increases absorption at higher band energies, producing a $+\Delta n$ change below the band edge. *Exciton screening* is a masking of the energy absorption spike due to excitonic effects. Excitons constitute pairing of electrons and holes in their respective bands in a Hydrogen-like bond. This tandem has a lower energy in the binding than without. *Exciton screening* is produced by the addition of carriers, which raises the field interaction in the bands, making it more difficult for electron–hole pairs to maintain the excitonic bond. The screening lowers absorption, which produces a negative index change.

2.5.1.4 Microsecond Time Scale. Since we are discussing time scales, it is appro-priate to mention again the thermal effect here. The long term effect of phonon relaxation is lattice heating, which raises the temperature of the device, and is removed by thermal conduction. This also raises the temperatures of the bands, producing the thermal effect on refractive index, and providing

a lingering Δn whose duration is dependent on heat sinking of the substrate. In these experiments, effects usually dissipated sufficiently for switching within $\sim 5\mu$sec.

2.5.2 Below-Band Refractive Index Change Modeling.   The nonlinear index of refraction (n_2) describes the refractive index of a nonlinear material under excitation intensity I, so that $n = n_0 + n_2I$. For semiconductors, the n_2 due to below band excitation has been modeled by Sheik-Bahae [41] using a two parabolic-band model to estimate the degenerate (and non-degenerate) absorption due to two-photon absorption and the linear and quadratic Stark effects. The model yields approximate values for n_2 (within a factor of 5 for $Al_xGa_{1-x}As$). For the purposes of this research, the model is sufficient to show a tendency for the nonlinear index, and a comparison of strengths for nonlinear indices for the varying x values in the $Al_xGa_{1-x}As$ mirror layers. Figure 14 presents calculated values for n_2 for two materials used in the samples measured for this thesis.
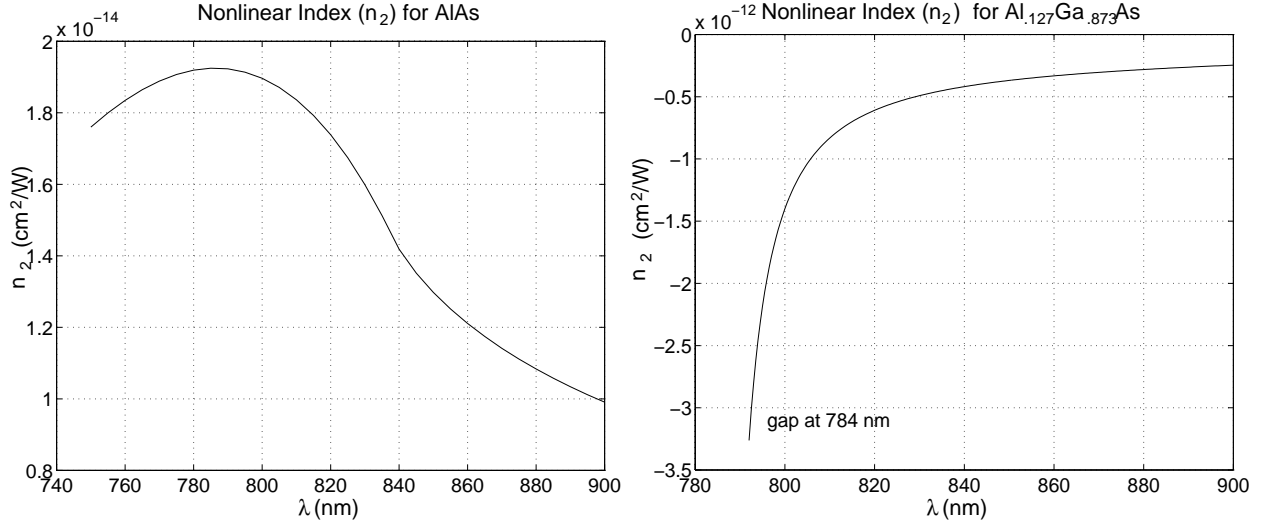
Figure 14. Calculated Nonlinear Index of Refraction (n_2) for $Al_xGa_{1-x}As$

In the experimental component of this research, the spectral region of interest is in the vicinity of the short wavelength edge of the stop band. For the $Al_xGa_{1-x}As$ structures examined, this is near the wavelength $\lambda = 830$ nm. The plots in figure 14 are useful in indicating the nonlinear index response we can expect from each material in the ultrafast regime. These plots base n_2 on the contributions of two-photon absorption and optical Stark effect only, so they apply only to these below-band

femtosecond–scale nonlinearities. For example, from the plots, at 830 nm, for an excitation of 10 kW/cm^2 (that used by He in the hybrid DBR bistability modeling mentioned in chapter 1), one expects a nonlinear index of $n_2 = 1.6 \times 10^{-14}$, and a total index change of $\Delta n = 1.6 \times 10^{-10}$ for AlAs. Similarly for Al$_{.127}$Ga$_{.873}$As, $\Delta n = -5 \times 10^{-9}$. Both of these values affect the material's total index only slightly. The plots indicate if we desire a large value for n_2, the excitation wavelength should approach the band-gap energy.

2.6   *Optical Switching of the DBR*

Effecting a switch in the DBR mirror by exploiting Δn is most readily accomplished by locating the pump wavelength on a sharp drop or rise in the reflectivity curve. These occur at wavelengths adjacent to the stop band. A positive Δn will shift the mirror reflectivity to longer wavelengths, as it increases the optical thickness of the layers $((n + \Delta n)\, d)$. This is borne out by the thermal plots shown in figure 4, showing the general shift to longer wavelengths produced by the positive index change. The short wavelength edge of the stop band is an ideal location for the expected shift to produce a large reflectivity drop. This will be demonstrated both experimentally and mathematically in chapters III and V. For the negative index shift, a blue-shift (shift to shorter wavelengths) is encountered. For this situation, locating near the reflectivity minimum, on the slope approaching the stop band, would produce a switch to higher reflectivity. These scenarios are exhibited in figure 15.

Alternatively, locating on the peak of the side-lobe should produce a reflectivity drop, as both the positive and negative changes in index $(\pm \Delta n)$ shift the reflectivity at the wavelength of interest off the sidelobe peak. As mentioned in chapter I, the minimum to the longer wavelength side of the stop band has been used to successfully switch the reflectivity of other periodic structures [19] and has been used in a DBR/linear mirror combination [1] to effect bistability. The desire to pump at the shorter wavelength side in this research stems from the prospect of being able to photo-pump the VCSEL, and at the same time, switch the reflectivity. This can effect a switch in the pump profile of the VCSEL, and is shown in chapter III to form a bistable VCSEL output.
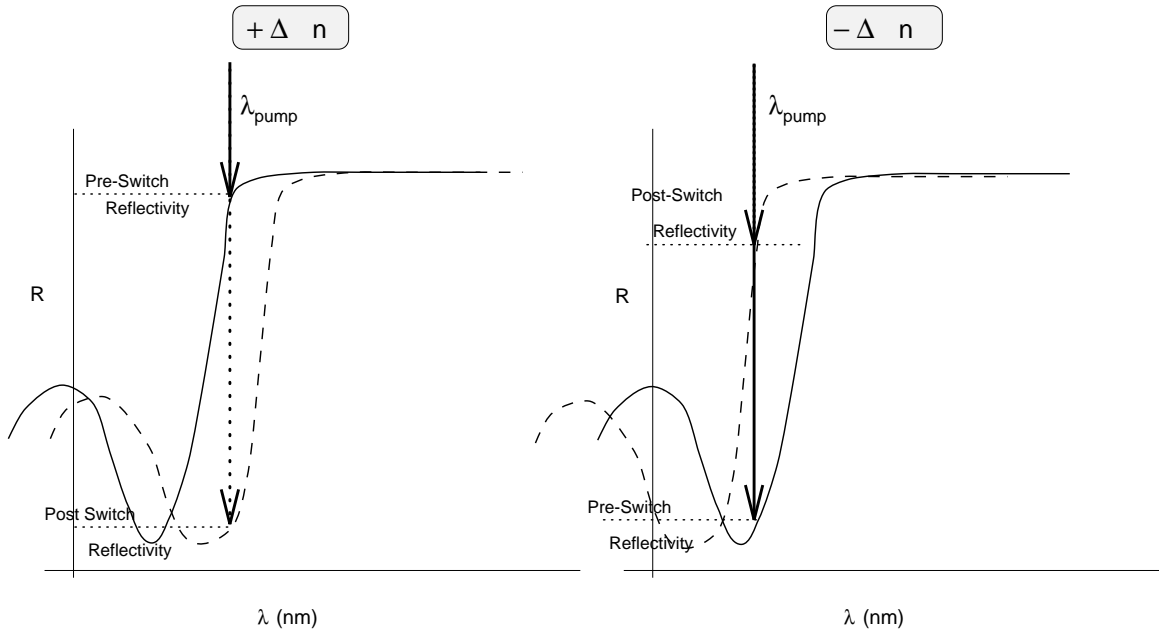
Figure 15. DBR Reflectivity Switching Schemes for Refractive Index Shifts ($\pm \Delta n$)

2.7 *Summary*

The nonlinearities discussed in this chapter each contribute to the effective change in reflectivity for the DBR/VCSEL system. Attributing a particular index/reflectivity shift to a given nonlinearity is possible because many of the effects work on different time scales. For the research conducted here, only the slowest (μsec time scale) and fastest (fsec/psec time scales) processes were examined. Before proceeding to the experiments, a summary of these nonlinearities will help to catalog their effects ($\pm \Delta n$) and time scales.

Thermal Effects.   These work on the longest time scale ($\sim \mu$sec) and affect all components (λ_{pump} above- and below-band edge); they are strongest in the high absorption layers (above-band), where the heating is greatest. The thermal effect is long-lasting (on the order of μsec to msec). It produces a relatively large $+\Delta$n in the wavelength region with which we are concerned.

Carrier Heating.   The $+\Delta$n from this process works on a psec time scale. The relaxation has been measured by Hultgren [20] as an exponential fall-off at a 1.1 psec rate for

28

$Al_xGa_{1-x}As$. That research also indicates the onset of index change from carrier heating is delayed [20]. The measured delay is on the order of 120 fsec, and Hultgren attributes the delay to a finite interaction time for the excited carriers to transfer their energy to the sea of carriers at the bottom of the bands.

Carrier Density Changes. This process (via two-photon absorption for below-band and single photon absorption for above-band excitation) produces a negative index shift $(-\Delta n)$ which acts on a femtosecond time scale, and remains until carrier recombination (~ 1 nsec) allows the depletion of the bands.

To some degree, the variation in experimental method (CW and pulsed experiments) and contrasting effects and time scales allowed the observation of lattice heating (long-term thermal refractive index change), as well as the carrier heating (identifiable by its relaxation), and carrier density changes. No variation of the experiment allowed the discrimination of the optical Stark effect or spectral hole burning from the other processes.

III. **Thermally-Driven Optical Bistability in $Al_x Ga_{1-x}As$ DBR Mirrors and VCSELs**

The examination of reflective bistability of the DBR mirror and VCSELs is the aim of this chapter. In this context, reflective bistability indicates a device's capability to have two stable reflectivities at a given incident power. The reflectivity is dependent on the history of the incident power. For example, the curve in figure 16 indicates the reflectivity can have a high or low reflectance at 280 mW of incident power, depending on which arm of the hysteresis curve the mirror is operating. The reflectivity can be switched by increasing or decreasing power to affect a switch to the other arm.
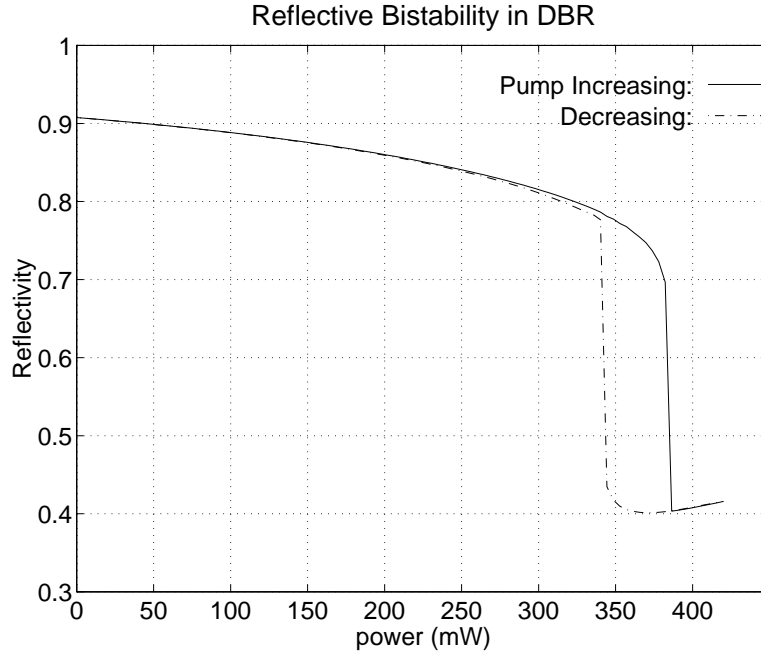
Figure 16. Reflectivity Bistability Curve

3.1 *Related Work in DBR Bistability*

Optical bistability in GaAs devices has been actively researched since the first demonstration by Gibbs *et al* in 1979 [16]. The use of Fabry-Perot etalons to enhance the nonlinear effects by operating at an optical resonance has become common practice, and the deposition of DBR mirrors in

place of the external Fabry-Perot reflectors significantly improved bistable performance [33]. Winful *et al* first proposed the capability of the distributed feedback (DFB) structure to support bistable operation, presenting a coupled-mode derivation of the operating characteristics of such a device [44] in 1979. Optical limiting in a vertical DFB structure was experimentally demonstrated in 1986 [1].

J. He, *et al* modeled [19] optical bistability in the reflectivity of a GaAs/AlAs periodic structure in 1991. Acklin [1] used this model to experimentally demonstrate optical bistability in a hybrid DBR/linear mirror arrangement in 1992. This reflectivity bistability is the closest published example of the physical mechanism occurring in the DBR bistability here. He's mathematical model accounts for the varying nonlinear index shifts in the mirror layers and predicts a distortion in the edge of the stop band for the DBR. This distortion produces a bistable jump in the reflectivity as the wavelength of an incident probe is varied (see figure 17). He *et al* plotted the spectral reflectivity in the DBR with and without the nonlinear index contribution in the DBR layers. The results plotted at figure 17(top) indicate the warping of the "linear" (no nonlinear contribution) curve at the first minimum to the longer wavelength side of the stop band.

This model considered a dominant $-\Delta n$ index shift due to carrier generated effects, so the expected reflectivity curve shift is toward shorter wavelengths (blue-shift). The reflectivity bistability at the stop band edge is evident in figure 17 (bottom), which is an expansion of the curve set to the left. This plot indicates a bistable reflectivity for wavelength tuning at a constant intensity. At $I = 18$ kW/cm^2, a probe beam, scanned spectrally from shorter to longer wavelengths, and starting at point E, would proceed through point B, then undergo a sharp drop in reflectivity to point C. If the wavelength of the incident laser is then decreased, the reflectivity would fall as the wavelength proceeds to point D, and sharply increase to point A. The jumps in reflectivity at λ_1 and λ_2 describe, in wavelength tuning, the hysteresis curve indicating the bistability. The plot indicates the intensity $I = 9$ kW/cm^2 is the threshold for this bistable reaction. This is the intensity at which wavelength tuning will produce a hysteresis with rise and fall wavelengths at the same point.

It is appropriate to note here the differences in this work to He's. The model used by He was restricted to a constant nonlinear index change, $n + n_2 I$, with n_2 independent of both field strength in the stack and wavelength. The model was two dimensional, including time-varying intensity and
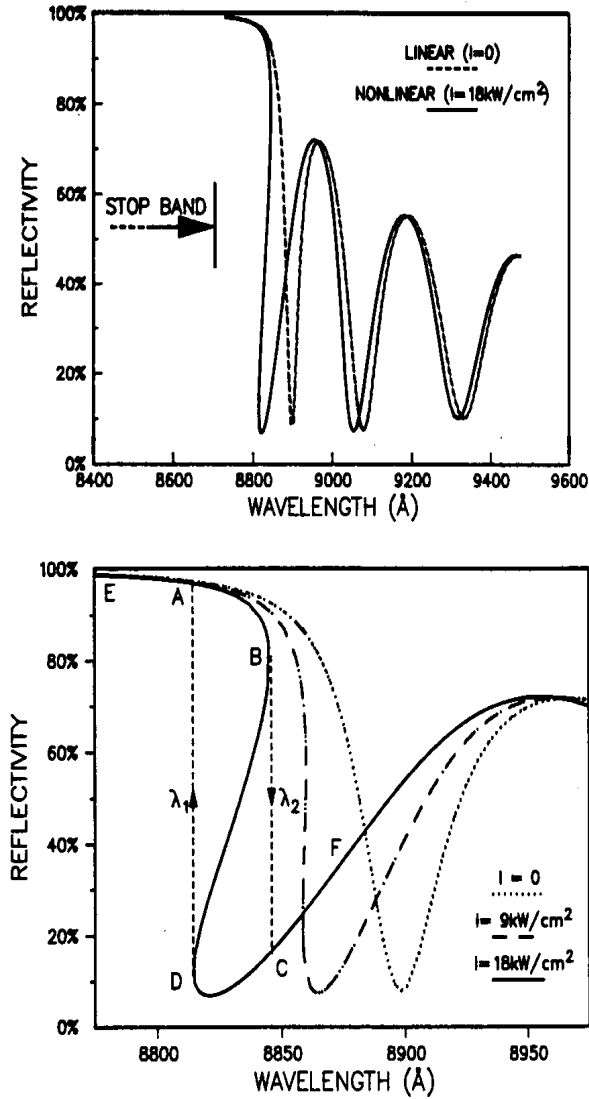
Figure 17. Plot of Linear vs Nonlinear Index Spectral Reflectivity in a DBR (top) and the Reflectivity Bistability Obtained (bottom) as Intensity is Increased (After He *et al*)

one spatial dimension (depth in the stack). The demonstration of bistability was accomplished with an added linear reflector and phase matching layer adjacent to the DBR to enhance the field strength in the DBR layers.

In contrast, this thermal model accounts for dispersion in the nonlinear index change, as well as a variation in the nonlinear effect with temperature of the layer; and works in three dimensions (time,

depth, and radial) which allows a description of the index profile which leads to the self-focusing of the pump beam as it pierces the stack. Additionally, the experimentally demonstrated bistability is attained in a monolithic structure, with no spacers or linear reflectors.

3.2 *Experimental Configuration*

The experimental part of this project involves the excitation of the sample DBR and VCSELs' structures to determine their optical switching characteristics. The configuration is depicted in figure 18. The excitation source was an argon-ion (Ar^+) pumped Titanium-Sapphire (TiS) laser. CW output from the TiS was used for thermal bistability experiments. Detailed equipment specifications are contained in appendix B.
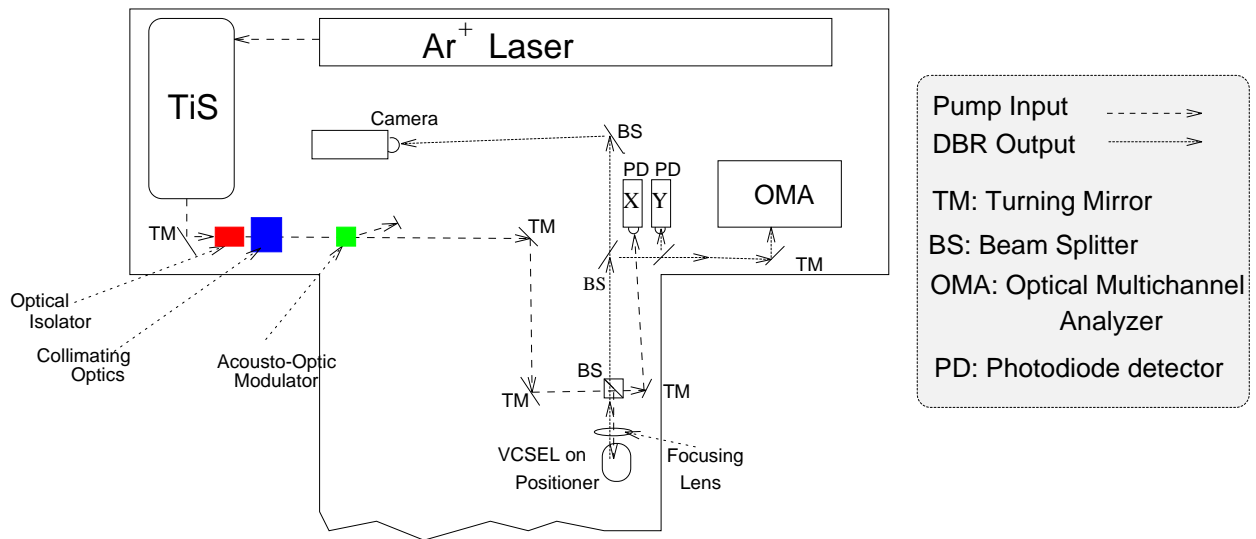
Figure 18. Experimental Configuration

The acousto-optic modulator (AOM) allowed ramping of the input intensity to plot the DBR response to the linearly increasing/decreasing pump. The TiS output was used to photo-pump the DBR, and the reflected output was collected at the diagnostic equipment: silicon photodiodes collected power input (X) and output (Y) to determine the reflectivity of the sample, an IR camera was used to monitor and align the laser spot on the DBR mirror and image the surface of the DBR, and an

Optical Multichannel Analyzer (OMA) measured the spectral content of the input pump and spectral reflectivity of the DBR/VCSEL.

3.3 DBR Bistability

The DBR mirror used for these measurements was grown by Wright Laboratories (WL/ELR) as a gauge sample to determine the fabrication quality of a Molecular Beam Epitaxy (MBE) system prior to growing a Vertical Cavity Surface Emitting Laser (VCSEL). VCSEL bistability is discussed later in this chapter. The DBR consisted of 17 periods of GaAs/AlAs layers with a 200 nm GaAs cap layer atop the mirror. These layers were deposited by MBE on a GaAs substrate ($< 100 >$ direction).

The mirror was found to satisfy the design wavelength (920 nm) and reflectivity criteria at wafer center. Unfortunately, only edge pieces of this wafer remained for this experiment. As is typical of DBR fabrication in MBE growths, the center wavelength of the mirror shifted to shorter wavelengths away from wafer center; this is due to thinning of the layers of the DBR there. The resultant reflectivity still indicated a DBR, but the center of the stop band was displaced to a shorter wavelength. The experiment required a close approximation of the actual thicknesses to reliably mathematically model the DBR reflectivity response. To determine the layer thicknesses of this DBR, Scanning Electron Microscope (SEM) measurements of the wafer layers of the sample were performed. These provided a ratio for the thicknesses of the GaAs to AlAs layers. This ratio was used to scale the wafer thicknesses in the matrix method calculations, and the layer thicknesses were adjusted in this ratio to match the spectral reflectivity measured by the OMA.

The original design prescribed layer thicknesses of 77.1 nm for the AlAs layers and 64.3 nm for the GaAs layers. The estimated thicknesses from the SEM measurement were 72.8 nm and 62.5 nm for the AlAs/GaAs layers respectively. The result is depicted in figure 19 and indicates a shift in stop band center wavelength to $\lambda_d = 886$ nm from the design of 920 nm.

3.3.1 Experimental Method. For most locations on the sample, reflective bistability was easy to achieve. Typically, the pump wavelength would be located spectrally at the short wavelength edge of the stop band as described in figure 15 for the positive Δn nonlinearity. This spectral location
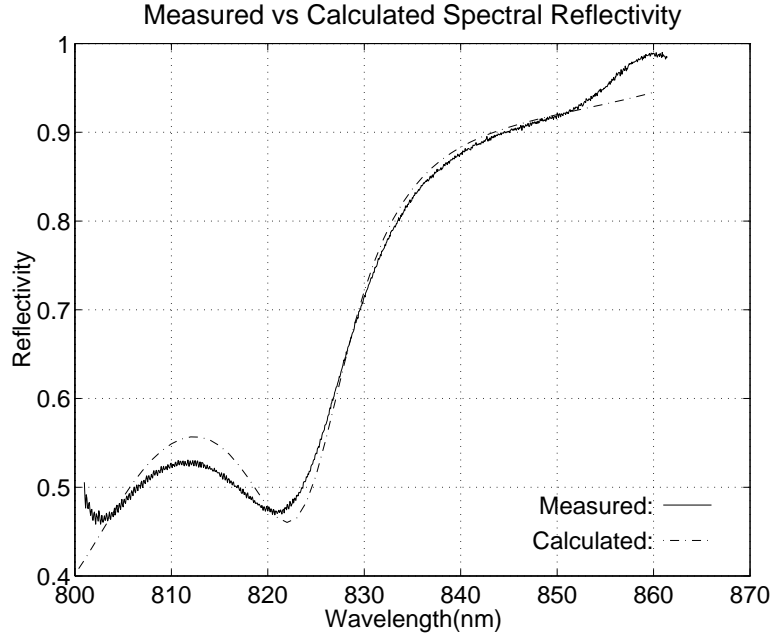
Figure 19.   Comparison of Measured to Calculated ($\lambda_d = 886$ nm) Spectral Reflectivities for 34
layer GaAs/AlAs DBR

of the pump positions it above a point of inflection on the spectral reflectivity curve. After adjusting

the pump wavelength to the desired location on the spectral reflectivity curve, pump intensity and

focus were adjusted to achieve bistability, and data collection proceeded.

3.3.1.1 Optical Switching.   Reflective bistability was obtained from a variety of

locations on the DBR wafer. Initial indications of a bistable output were detected by using a triangle-

wave input function to the AOM. All input triangle wave signals were 20 % duty cycle, to allow some

temperature settling between triangles. When referring to the duration of the triangle-wave, the intent

is the time for ramp-up and ramp-down of the triangle only. For example, in the figure below, the

triangle duration is 1 msec, although its period is 5 msec (the zero intensity part of the cycle having

been truncated).

The first order mode from the AOM was then guided to a focus on the DBR mirror, with a

spot size of $\sim 2\mu$m, gauged by imaging the spot at the camera, and inserting a USAF optical target

in place of the DBR. Line pairs then indicated the spot size. The DBR was thermoelectrically cooled

35

to maintain its substrate at room temperature; the reflected signal and incident signal were each collected by a separate fast ($\sim$ 1 nsec) photodiode detector. Optical switching was indicated by the output triangle-wave developing "kinks" on the up/down slopes, as indicated in figure 20. If optical switching were absent, the reflected output would have the same form as the input.
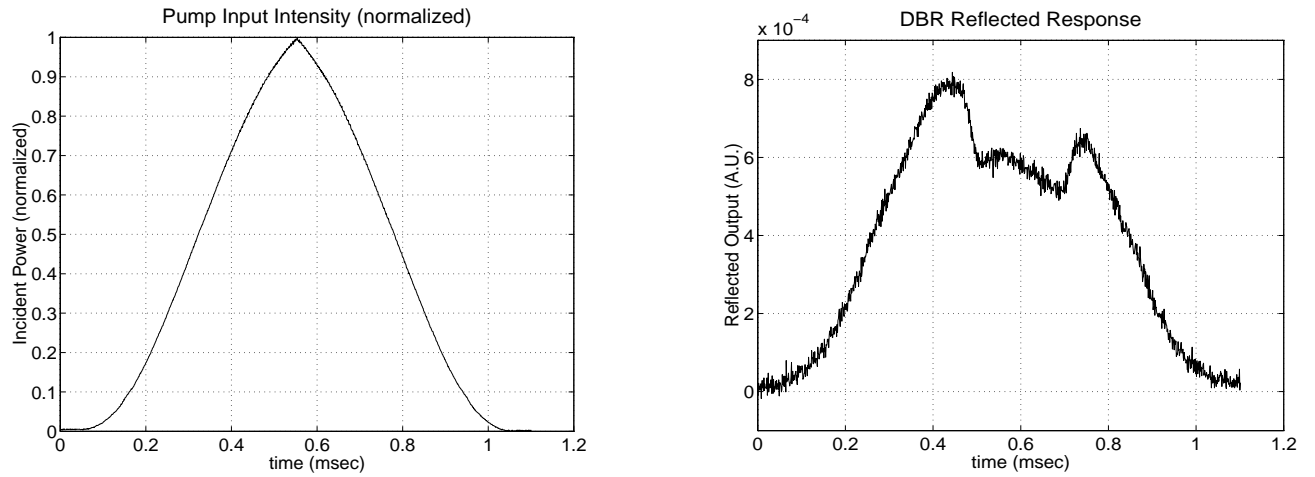
Figure 20. Input(X-Channel) and Output (Y-Channel) Waveforms for a Bistable Reflector

These "kinks" are due to the reflectivity of the mirror switching down as the thermal nonlinearity shifts the spectral reflectivity to longer wavelengths (see figure 21). The mirror switching time indicated by this shift is plotted in figure 21(right) and indicates a response time (10 to 90 %) of 38 μsec for switch-down and 30 μsec for switch-up.

3.3.1.2 Optical Bistability. Placing each photodiode output into an X-Y configured oscilloscope resulted in the typically seen bistability curve: X-input intensity and Y-output reflected intensity. The entire set-up was calibrated by replacing the DBR with a high reflectance mirror ($\sim$ 99 % reflectivity) and collecting its X-Y outputs. A resultant bistability curve is shown in figure 22 below. To determine the values for the figure, the reflected DBR Y signal (pictured in figure 20(right) above) was divided point-by-point from the reflected Y signal from the calibration standard (mirror). The result was plotted point-by-point against the input intensity (Figure 20(left)), which was the same form for both DBR and mirror. For low signal levels (early and late in the triangle) the signal to noise
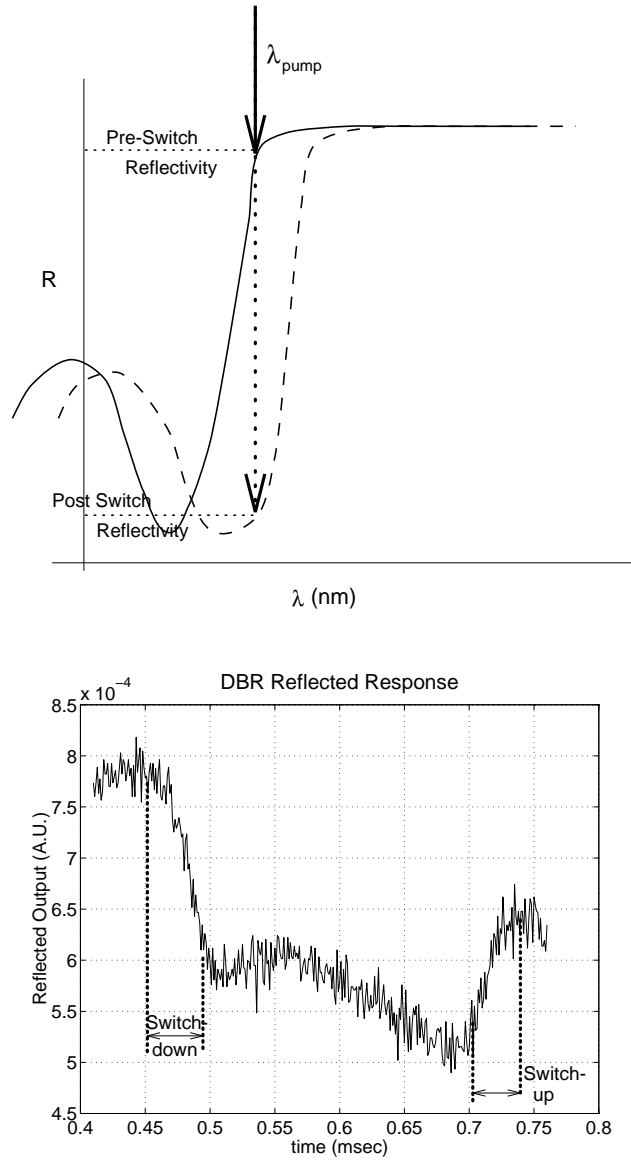
Figure 21. Pumping Scheme and Reflectivity Switching for DBR

ratio was too low to allow the division of the DBR output by the high reflector output, and it was necessary to truncate.

3.3.2   Experimental Results.   A plot of the DBR spectral reflectivity is shown in figure 23. This location exhibited bistability at pump wavelengths from 832 to 834 nm. Both wavelength and triangle-wave duration were varied to explore the effects on the bistability.
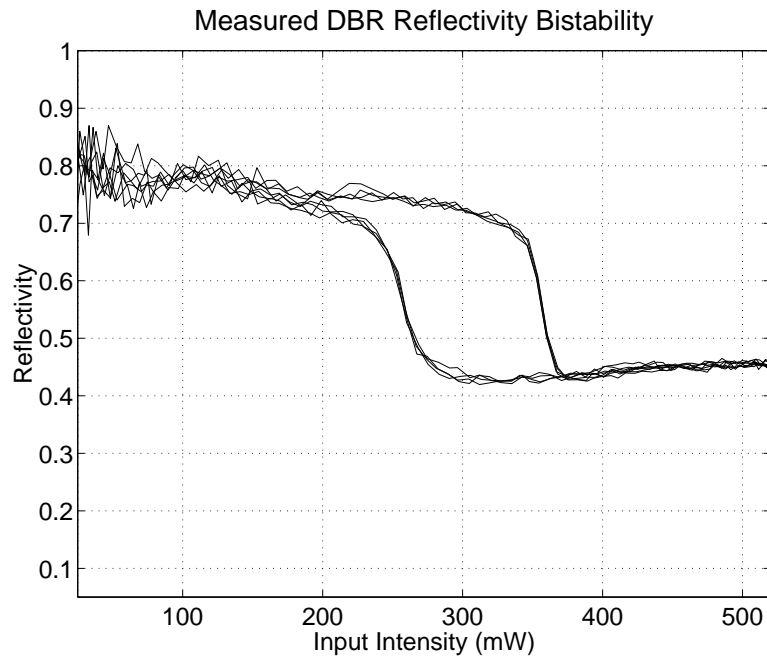
Figure 22. Typical Reflective Bistability Output after Data Reduction
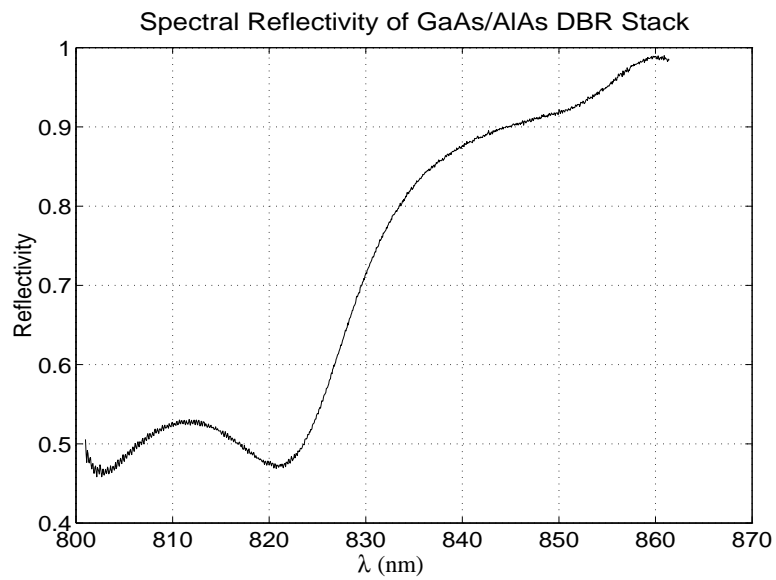
Figure 23. Spectral Reflectivity of Sample DBR Mirror

At 833 nm, the bistability for a 10 msec triangle-wave input indicates the characteristic hysteresis in figure 24 (left). Speeding up the triangle to a 1 msec duration elongates the hysteresis and shifts the switch-down intensity to higher intensity (see figure 24 (right)). This delay in switching is due to the increased speed of the ramp-up in intensity on the triangle. The increase in intensity build-up exceeds the reaction time of the structure to heat and change index. Similarly, on switch-up, the 1 msec triangle bistability curve switches up at a lower power. Again, this can be attributed to the ramp-down speed exceeding the capacity of the structure to effect the index change. As a result, the entire hysteresis spreads along the input intensity axis. The reflectivity of the bistability curve
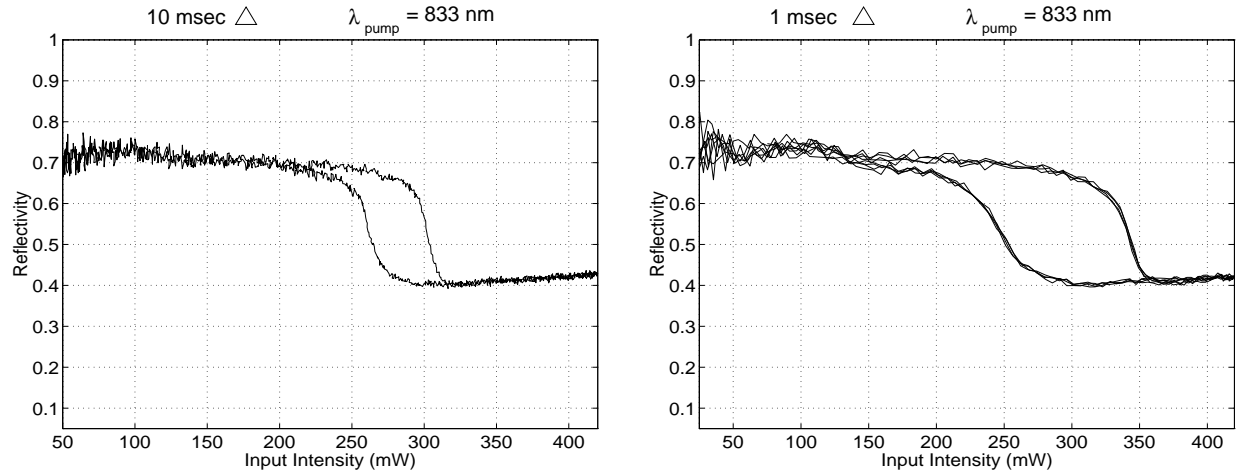
Figure 24. Reflective Bistability at 833 nm as Input Intensity Speed Increases

indicates that, at low powers, it maintains $\sim .72$ reflectivity. This agrees, roughly, with the spectral reflectivity curve shown in figure 23. The switch-down is to approximately $R = .4$ which is lower in reflectivity than the minimum adjacent to the stop band in figure 23. Of course figure 23 represents an approximation of the spectral reflectivity of the region surrounding the spot we are measuring. It was taken with a white light source, focused to the area surrounding the spot. The white light source is roughly collimated, but its spot on the wafer is still much larger ($\sim 10\times$) than that of the pump laser. Additionally, the act of focusing the light spreads the angle of incidence of the input light, this acts to convolve the spectral reflectivities gathered from the illuminated area, tending to soften the contrast, so the minima will not appear as deep.

3.3.2.1 Wavelength Tuning Effects. Tuning the pump input wavelength slightly higher corresponds to moving up the spectral reflectivity curve in figure 23. Initially, more pump intensity is reflected from the DBR, so that the internal fields are weaker than at the same input intensity at the shorter wavelength. The intensity to effect switch-down, then, should increase. Figure 25 supports this outlook, if one compares figure 25 (left) to figure 24 (left). The switch-up
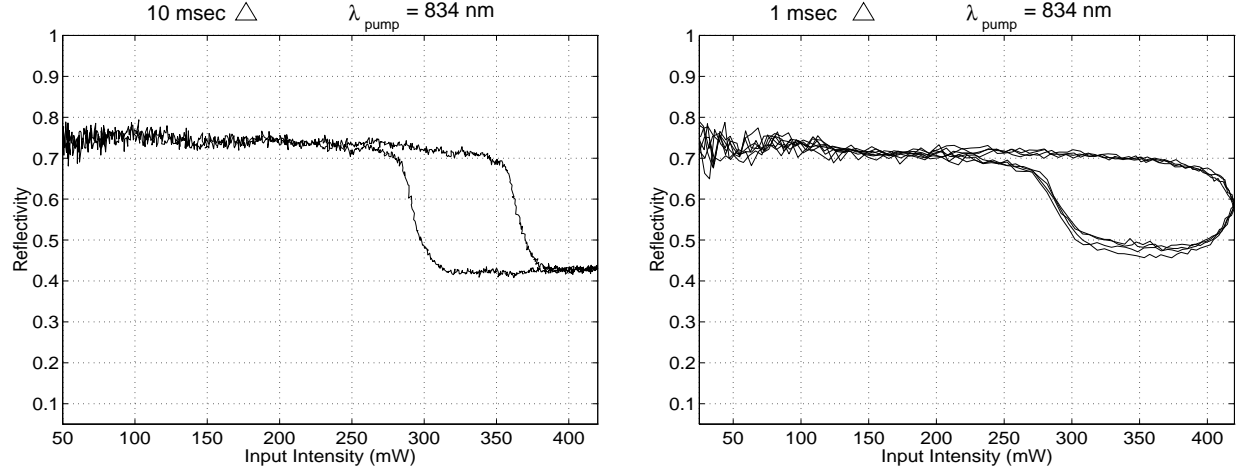
Figure 25. Reflective Bistability at 834 nm as Input Intensity Speed Increases

intensity has also increased, because the intensity necessary to maintain the fields in the DBR to keep the refractive indices of the layers elevated increases. Comparison of the 10- and 1-msec triangle-wave inputs indicates the same stretching of the hysteresis as noted at 833 nm. In addition, the hysteresis has widened in increasing the pump wavelength from $\lambda = 833$ to $\lambda = 834$ nm. Part of the widening of the hysteresis is due to a lower extinction coefficient at this longer wavelength. The lower extinction coefficient requires more field build-up to effect the same heating, so that the difference in intensities between switch-down and -up increase as the wavelength is increased.

Another aspect of the plots for the $\lambda_{pump} = 834$ nm is the distortion of the hysteresis in the 1 msec triangle plot (see figure 25(right)). To see why, compare the reflected outputs of the mirror and DBR (see Figure 26 below), which shows two successive 1 msec triangle inputs at the 20 % duty cycle. The switch-down of the DBR indicates it starts before the peak intensity and ends well after. This produces the drop in reflectivity at the peak intensity in figure 25(right) which continues to fall

as the intensity decreases, producing a rounded edge to the switch-down arm (larger intensity arm) of the hysteresis. If the peak power of the triangle were increased, or the triangle speed were slowed, the reflectivity transition would proceed before the decrease in input intensity starts, and an undistorted hysteresis would result.
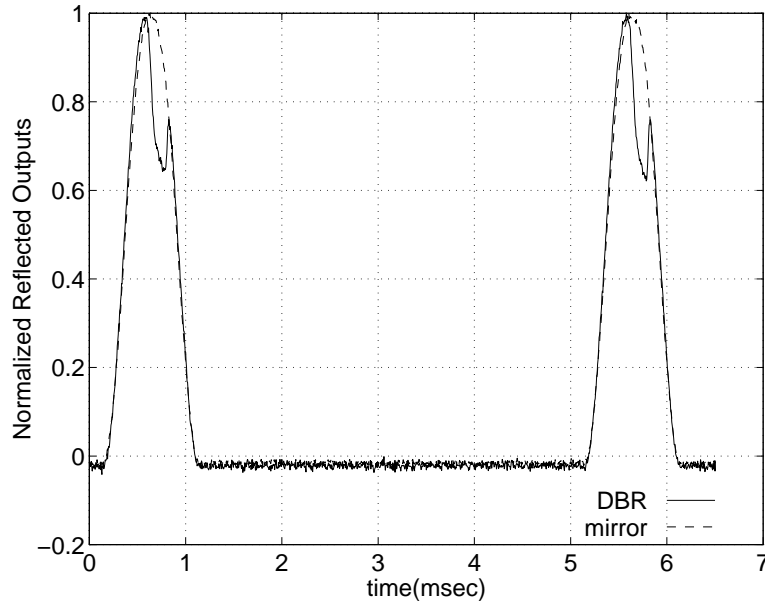
Figure 26. DBR and Mirror Reflected Outputs (normalized)

Decreasing the input wavelength has an opposite effect, as is shown in figure 27. Here the lower entry reflectivity on the spectral reflectivity curve allows more intense fields to penetrate into the stack earlier in the ramp-up, and remain later in the ramp-down, so that the switch-down and -up occur at lower powers. A plot of the bistability for triangle wave input at the same speed, but pump wavelength at $\lambda = 834$ nm is included for comparison. The hysteresis has narrowed in proceeding from $\lambda = 834$ to $\lambda = 832$ nm. As shorter wavelengths are approached, the hysteresis gradually disappears, eventually providing an optical switch without the bistable response.

3.3.3 Computer Modeling. The computer modeling of the thermal bistability uses an algorithm based on the work of McGahan and Cole [34] and Shih [42] described in Chapter V, solving for the temperature distribution at each time step in the triangle-wave. The program iterates
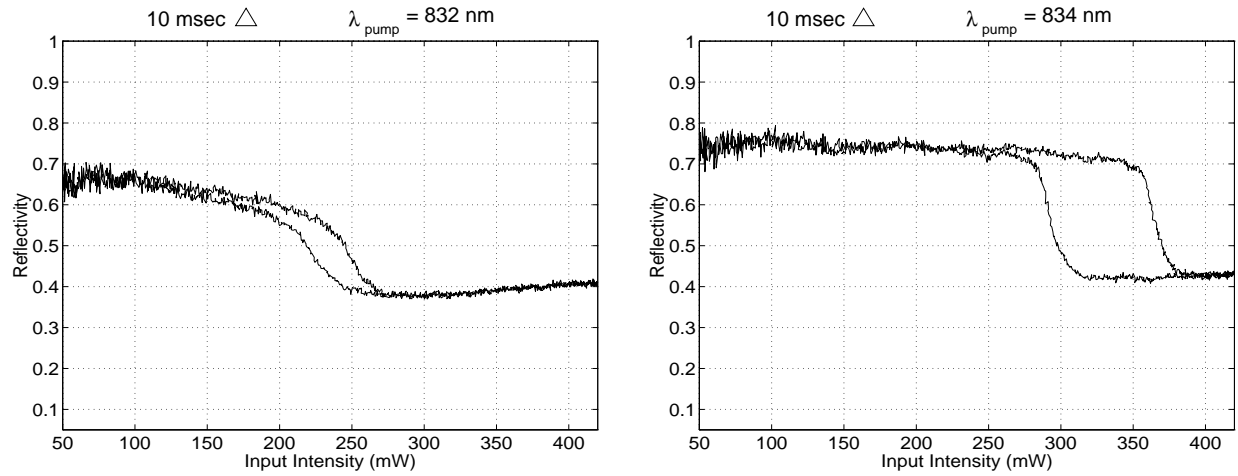
Figure 27. Reflective Bistability at 832 nm vs 834 nm

to find a stable temperature distribution, adjusting the refractive index, extinction coefficient, thermal conductivity, and thermal diffusivity at each iteration to match the temperature distribution along the centerline of the pump beam entering the stack. A typical plot of the temperature distribution along this centerline is shown in figure 28, showing the temperature profiles prior to and just after the reflectivity switch. The plots indicate a jump in temperature of nearly $180^\circ C$. For comparison, the melting point of GaAs is $1238^\circ C$ and for $Al_xGa_{1-x}As$ is $T_{MP} = 1238 - 58x + 560x^2$ for the *solidus* line (temperature at which the solid begins to liquify) [2].

3.3.3.1 Modeling Results. The model predicts a bistable output for the structure, as indicated in figure 29. The two plots indicate the increasing speed of the triangle-wave input widens the hysteresis, as in the experimental behavior. The parameters for the DBR in the model match those of the sample DBR. The resultant reflectivity curves indicate bistable behavior, as in the experiment.

The mathematical model's response also indicates a pump wavelength dependence as in the experiment. The computer model's hysteresis widens with increasing pump wavelength as shown in figure 30 below. As in the experiment, when the pump wavelength is tuned to longer values, it proceeds up the stop band, experiencing higher reflectivity and smaller absorption values. The intensity for switch-down increases. Switch-up also occurs at higher intensities for longer wavelengths. For the computer modeling, the widening of the hysteresis is best understood by the degree to which each

42
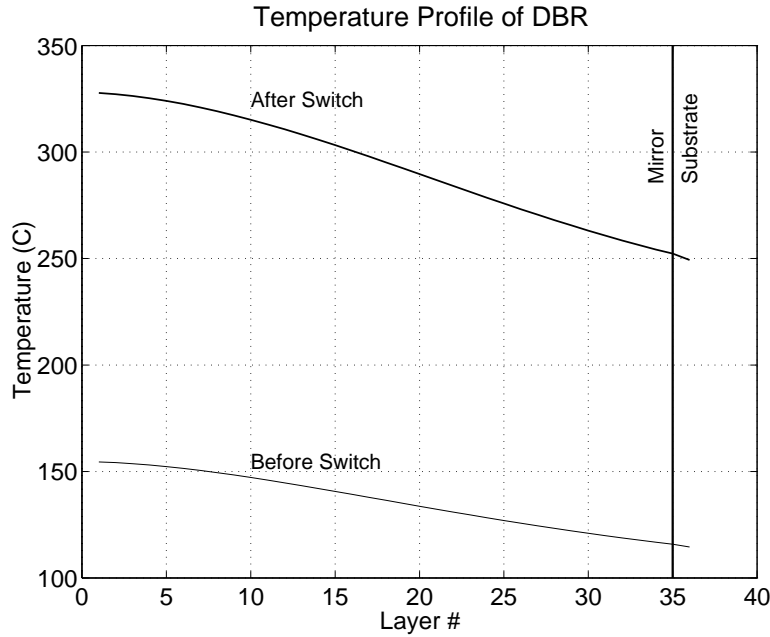
Figure 28. Temperature Distribution Along the Centerline of the DBR Stack,

spectral reflectivity curve shifts. This can be quantified by examining the pump wavelength location with respect to the change in curvature (point of inflection) of the stop band. For this set of DBR parameters (mirror layers & cavity thickness, x-concentrations of the layers, design wavelength, and pump wavelength), the series of plots in figure 31 indicates the shift in the spectral reflectivity curve for a typical build-up in temperature from laser heating.

Figure 31, when differentiated with respect to wavelength, shows that the reflectivity jump for switch-down occurs around a point of inflection on the spectral reflectivity curve. The first derivative peak, which represents the change in curvature, transitions from the short-wavelength side of the pump wavelength to the long-wavelength side after the switch-down. A plot of the first derivative is shown in figure 32.

The termination of the reflectivity switch-down varied depending on the wavelength separation $\Delta\lambda_s$ between the pump wavelength and this inflection point. This can be seen from the series of plots in figure 33 below. For larger $\Delta\lambda_s$ the pump wavelength is located higher on the stop band up-slope, and the incident power must be greater to effect the switch. When switched, this greater intensity

43
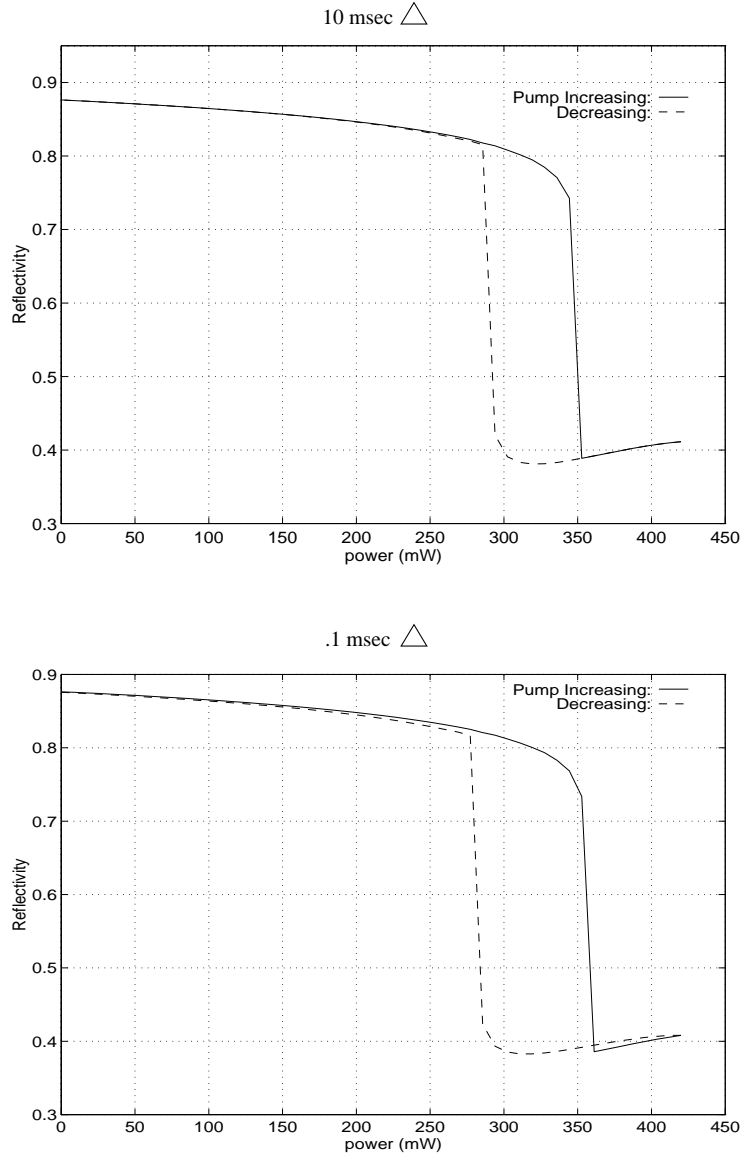
Figure 29. Effect of Increasing Triangle Speed, $\lambda_{pump} = 840$ nm

produces a larger temperature shift, which drives the reflectivity curve to longer wavelengths, moving the minimum further past the pump wavelength. In the bistability hysteresis, this results in a widening of the hysteresis. It is evident from the figures that $\lambda = 838$ nm is near the limit on bistable response from this sample (as the hysteresis is very narrow). No consistent metric was found in the model results to indicate the shortest wavelength for switching. It is likely dependent on the steepness of
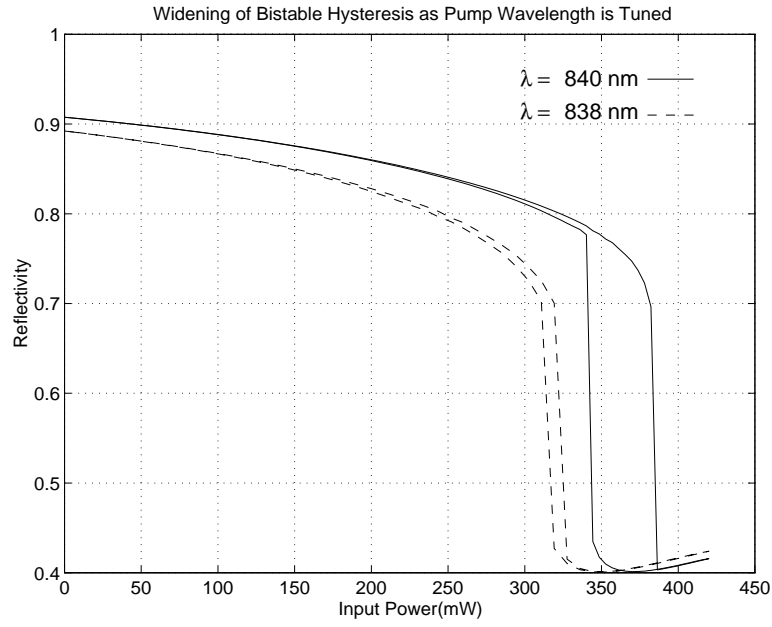
Figure 30. Widening Hysteresis in Mathematical Model Result from Pump Wavelength Change
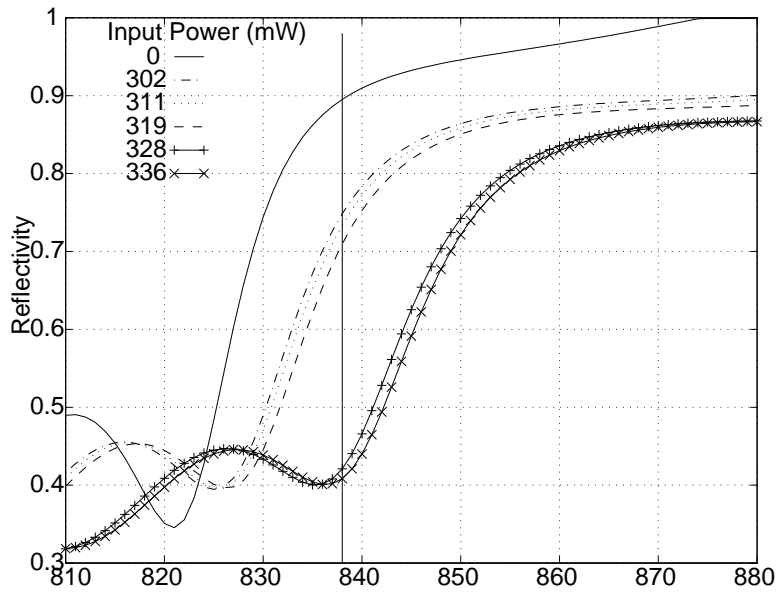
Figure 31.   Spectral Reflectivity Change of the DBR as the Reflectivity Switches Down: $\lambda_{pump} = 838$ nm
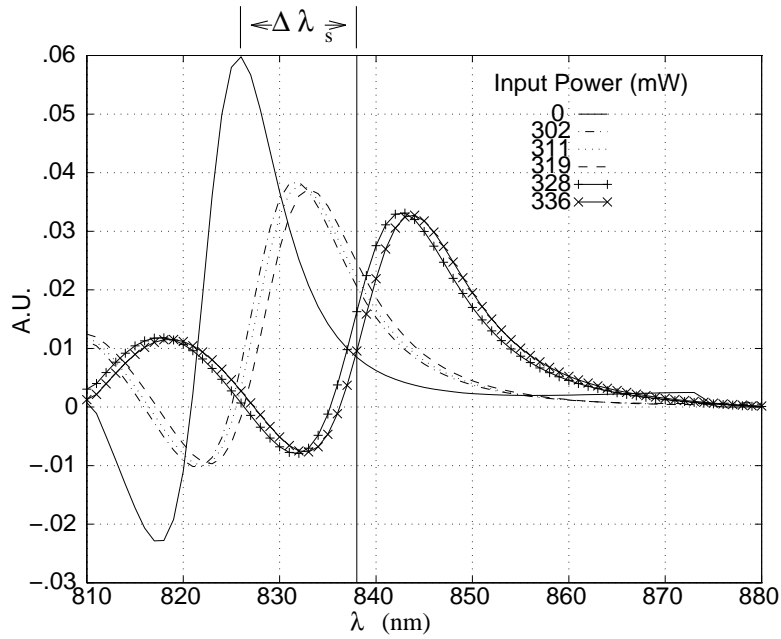
Figure 32. $\frac{\partial}{\partial \lambda}$ of Spectral Reflectivity as Reflectivity Switches Down: $\lambda_{pump} = 838$ nm

the stop-band slope, so there may be a correlation between its curvature/inflection point height and the pump wavelength.

In a similar manner, as the switch-up occurs, the point of inflection (maximum) passes through the pump wavelength as it travels to the shorter wavelengths. The spectral reflectivity plots and first derivative for the switch-up are displayed in figure 34.

3.3.3.2 Modeling Accuracy. As with any model this model's predicted results do not exactly match the experimental behavior. Bistability was obtained in this model for wavelengths ranging from 836 nm to 842.5 nm. This range is wider and resides higher on the stop band edge than that found experimentally (832-834 nm). Switch-down intensities occurred at lower intensities than in the experiment for similar wavelength locations within the range of bistable wavelengths, and switching transitions were sharper in the model. For input speed increases, hysteresis widening is not as significant in the computer model: a 10 msec triangle increased in speed to .1 msec produces a 33 % increase in width in figure 29; a 10 msec to 1 msec increase in speed in the experiment (Figure 24) produced a 90 % widening. Although the model does not exactly pattern the behavior witnessed

46
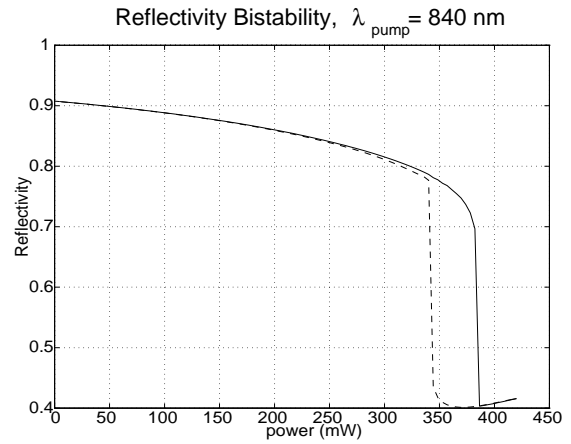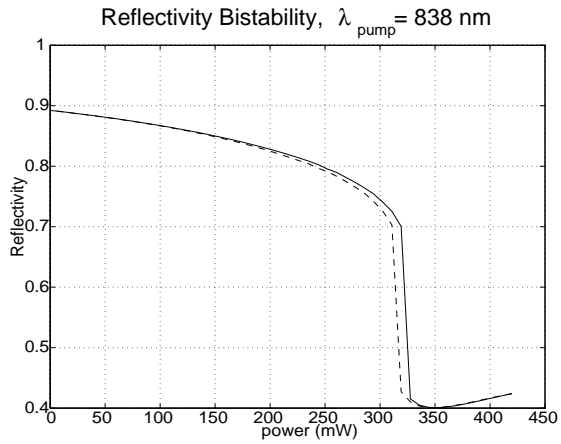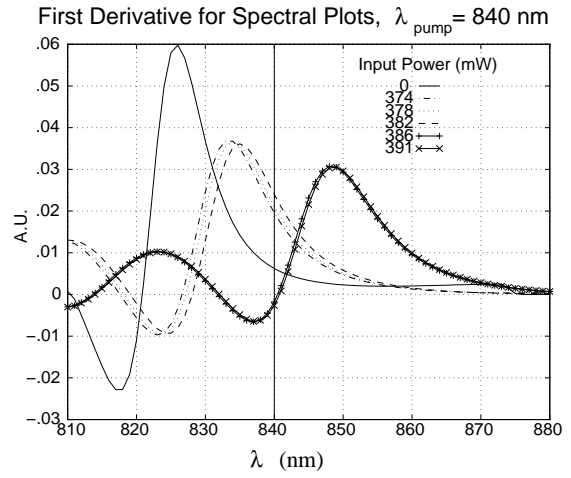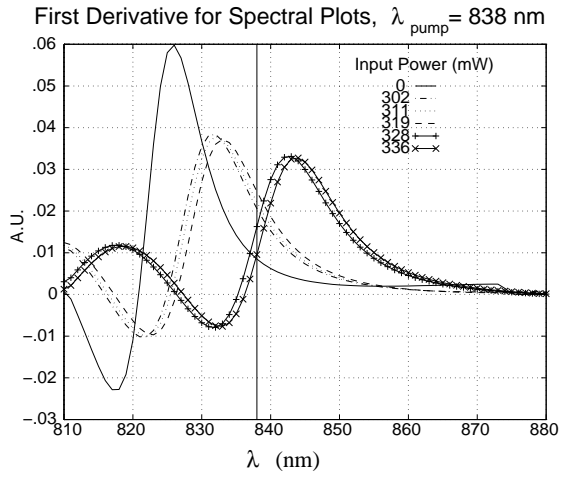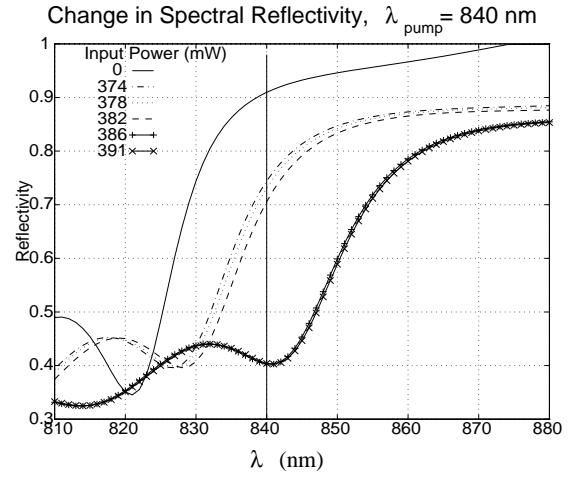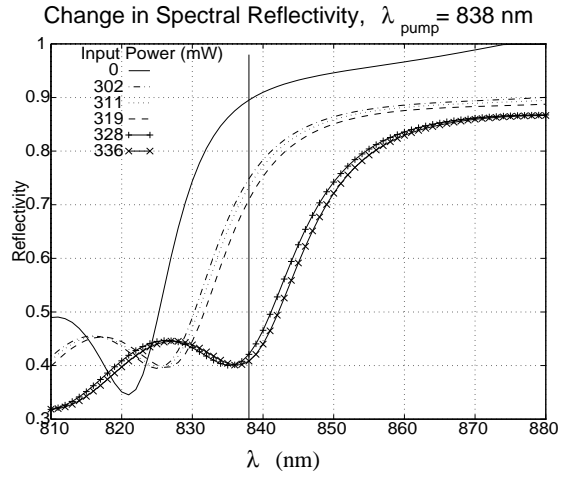
Figure 33. Switching Behavior as $\Delta\lambda_s$ is Increased

47
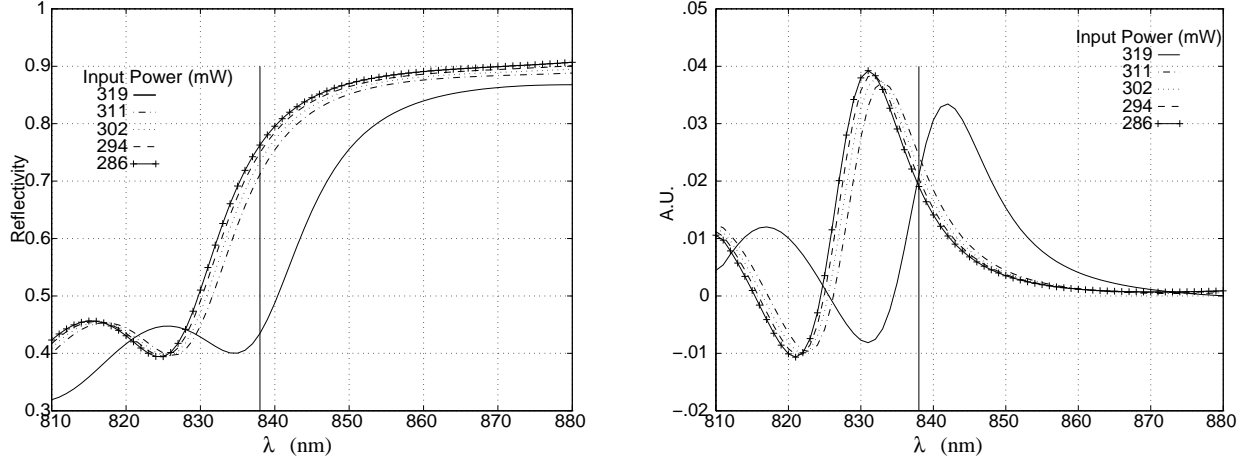
Figure 34. Spectral Reflectivity Change and First Derivative for Switch-Up: $\lambda_{pump} = 838$ nm

in the laboratory, it provides a useful means of examining the thermal drivers of the experimental results.

Many of the inefficiencies in the experiment (pump power delivery, surface scattering of the incident intensity, heat removal/cooling) are not incorporated in the model. These contribute to the elevated intensities required to effect the switching in the experiment, and the greater range of wavelengths at which bistability could be found in the model. As the model switched at lower intensities, it had increased available power to effect switching at longer wavelengths (higher up the spectral reflectivity curve stop band). Additionally, thermal lensing, although anticipated by the temperature distribution in the model, is not included. Lensing, though, should help to decrease switching intensities: it concentrates the input intensities, producing a switch-down at smaller incident powers.

The sharper transitions are a side effect of the model requiring a steady-state temperature distribution before it increments the input intensity. The sample DBR does not require a steady state condition before it responds to the elevated intensity in real-life. The model, in contrast, must adjust its temperature dependent parameters before it proceeds, to mimic the dynamics of the reflectivity, and so is limited to finding a steady state condition at each step. As a result, a transition that may have

only partially taken effect in the real DBR before it responds to the new intensity must be completed in the model DBR before it can proceed.

Finally, differences in response between model and experiment could result from inaccurate structural specifications in the DBR model. The layer thicknesses were estimated via the SEM measurement, and had a measurement accuracy of 1 nm. The resultant estimates govern the $\lambda/4$ layer thickness, so that the expected error in the actual λ_d for the DBR is $\pm$ 4 nm. This shifts the model's wavelength range within the experiment's range.

3.4 VCSEL Bistability

The reflectivity bistability seen in the DBR can be used to drive a bistable reaction in the VCSEL. By pumping the VCSEL in a similar manner (at the edge of the VCSEL stop band above the pump minimum) we could achieve photo-pumped lasing in the VCSEL, and subsequently effect the reflectivity switch, producing bistable operation in VCSEL output power, lasing wavelength, and spot size.

3.4.1 VCSEL Structures Tested. Three sample VCSEL structures were tested. All three used a bulk GaAs cavity/gain region, and all had mirror layers of $Al_{.127}Ga_{.873}As/AlAs$ mirrors. The first sample used a 3 λ_d cavity, with 51 bottom mirror layers (25 $\frac{1}{2}$ periods of $AlAs/Al_{.127}Ga_{.873}As$) and 44 top mirror layers (22 periods $Al_{.127}Ga_{.873}As/AlAs$). The physical thickness of the mirror layers was: AlAs: 73.2 nm: $Al_{.127}Ga_{.873}As$: 61.8 nm : Cavity (GaAs): 726 nm. The second sample used a less reflective set of mirrors, but stayed with a 3 λ_d cavity (top mirror: 17 periods, bottom: 22 $\frac{1}{2}$ periods), with the same physical thicknesses. The third sample used a larger cavity, expanding to 9 λ_d (2.168 μm), and remained with the same mirror structure as Sample 2. λ_d for all three samples was approximately 880 nm, but actual lasing wavelengths ranged $\pm$ 15 nm.

3.4.2 Experimental Results. As for the DBR, bistability was present for almost every undamaged section of the VCSEL samples. Spectral reflectivity for Sample 1 is shown in figure 35 below:
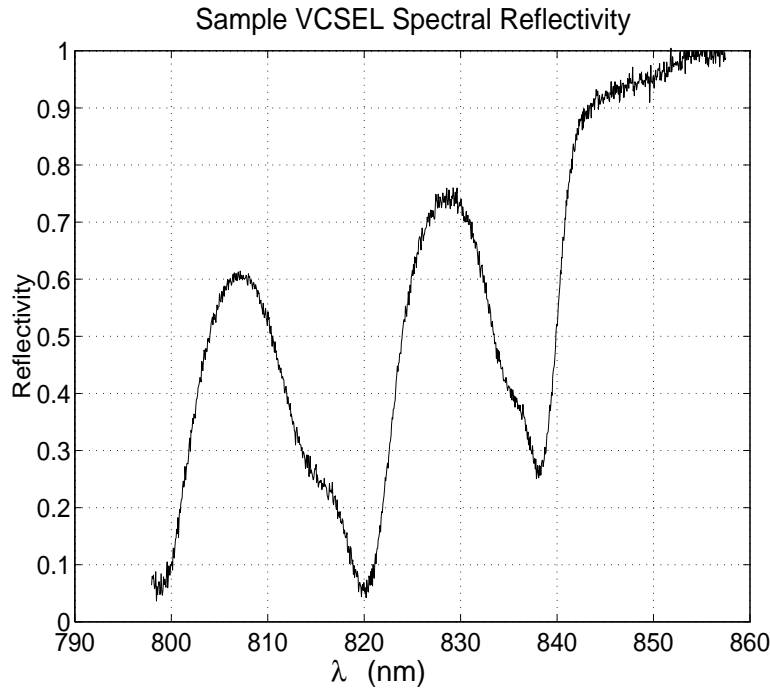
Figure 35. Spectral Reflectivity Curve for VCSEL Sample 1

3.4.2.1 Optical Switching. The VCSEL switching behavior was similar to the DBR. Sample 1 exhibited the fastest switching speeds. For this VCSEL, the fastest switch-down speed was approximately 4.1 μsec, and the longest was 7.6 μsec. A plot for the reflectivity switching is shown in figure 36. The fastest switch-up was 7.75 μsec and switch-up times ranged up to 9 μsec. These speeds were observed for a triangle duration of 0.2 μsec.

To compare switching speeds with the DBR, plots of the reflected output for each are superimposed in figure 37. The plots are for a triangle speed of 1 msec, the fastest for which both DBR and VCSEL measurements were accomplished. The VCSEL switch-down, at 15 μsec is 40 % faster than the DBR (25 μsec). Although the VCSEL has more layers than the DBR, its cavity assists in building the field strength and temperature increase for an incremental increase in incident power. The sharper stop band edge of the VCSEL results in a sharper inflection on the stop band edge. The index change necessary to shift the reflectivity curve is as a result smaller, so that the temperature change necessary for the shift should be less in the VCSEL than in the DBR. This is so: the DBR switch involved a higher temperature change ($\sim$180° see figure 28) than in the VCSEL ($\sim$110° see figure 49). The

50
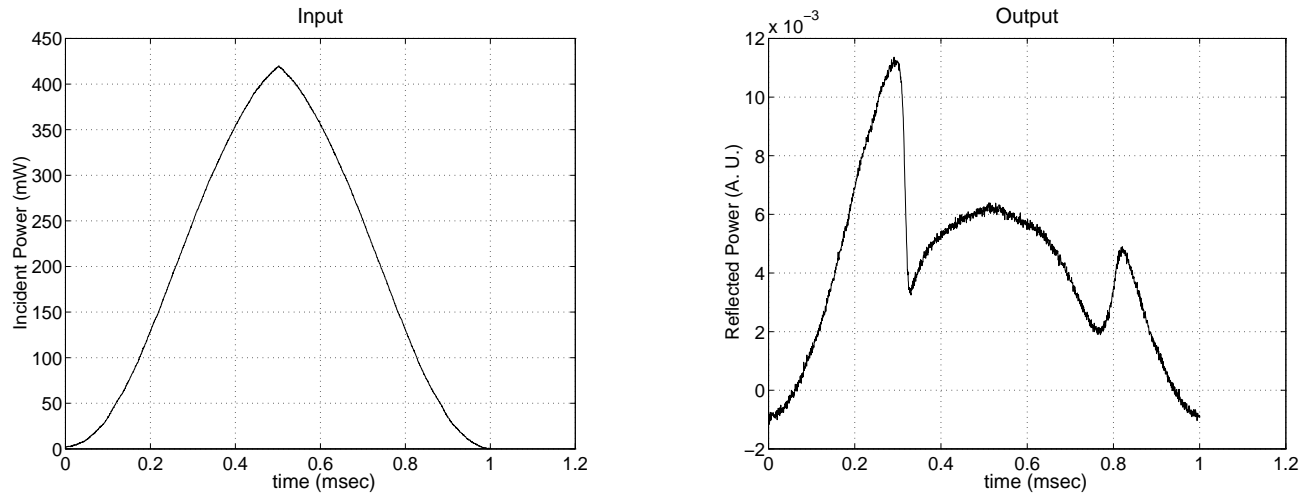
Figure 36. Pump Input and Reflected Waveforms for VCSEL: Sample 1
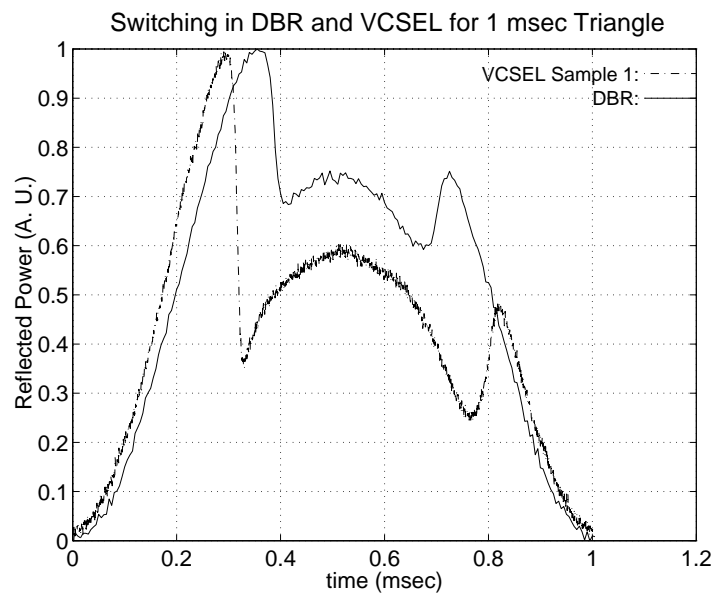
Figure 37.   Comparison of DBR/VCSEL (Sample 2) Responses to 1 msec Triangle-Wave Input Intensity

51

sharper stop band edge may also assist switch-down in the VCSEL over the DBR, as the necessary heat build up is less, it is achieved more quickly at a given input intensity. Additionally, the field intensity in the VCSEL mirrors near the pump minimum is greater than the DBR, as indicated by the normalized field strength plots (figures 5 and 8); so both the field intensity and the sharp stop band edge increase the VCSEL switch-down speed over the DBR.

Switch-up speeds in this comparison were nearly identical (both 30 μsec). The switch-up is governed by the material's ability to shed latent heat, which depends more on the thermal conductivity/diffusivity than the optical response of the structure. Between VCSELs, similar tests were performed. Sample 2, with the same cavity size and fewer mirror layers, had switching speeds between 20-25 μsec for switch-down and 30-32 μsec for switch up, with the 1 msec triangle-wave input. Sample 3, with a 9 λ_d cavity thickness had three times the cavity thickness of Samples 1 and 3, and the same mirror structure as Sample 2. Sample 3 produced switching times of 25 μsec (switch-down), and 35 μsec (switch-up) for 1 msec triangle input. This data implies switching speed is improved more by increasing the number of mirror layers (increases cavity Q, or intensity storage) than by increasing the cavity length (increases cavity absorption).

3.4.2.2   Reflectivity Bistability.   The VCSEL bistability was multi-symptomatic. The reflective bistability of the DBR mirror was evident, as the plots in the switching section above indicate. For the VCSEL, however, the power at which switch-down occurs is dramatically lower. Sample 2 typically switched at incident intensities near 175 mW, compared to 350 mW for the DBR. The increased number of mirror layers boosted reflectivity, and the addition of the absorptive cavity increased the heat in the center of the stack. Increasing reflectivity and the absorptive cavity both contributed to the lower power requirement for switching. The X-Y plot at figure 38 shows the bistability more explicitly.

3.4.2.3   Power Bistability.   When the VCSEL could be brought to lasing before the switch was effected, the reflectivity switch could be used to drive a bistable lasing output. The switching of the reflectivity represents a sudden increase in the pump intensity arriving at the gain
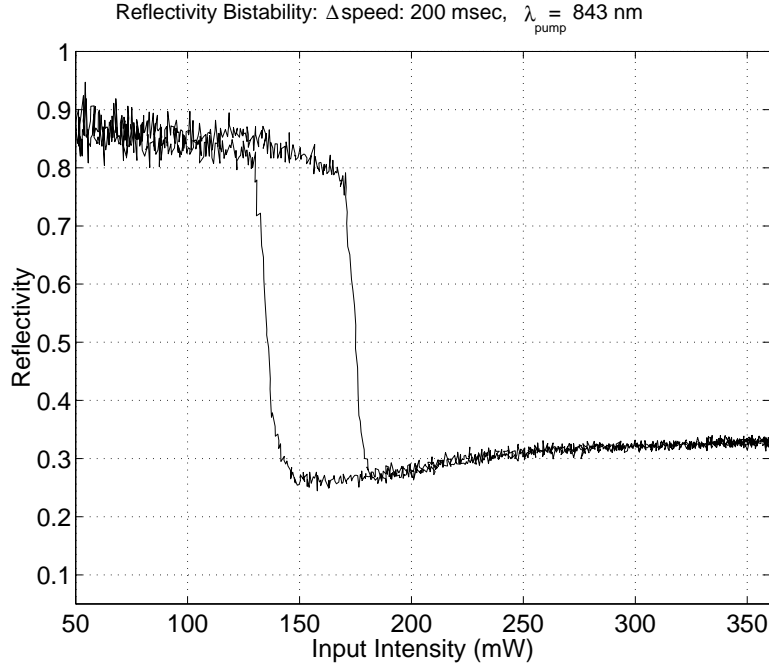
Figure 38. Reflectivity Bistability for VCSEL Sample 1

medium. The laser (VCSEL) undergoes an abrupt increase in power output. The resultant input power jump produces a spike in the lasing output at reflectivity switch-down (see figure 39).

Initially, it was suspected the VCSEL was gain-switching in reaction to the sharp input power increase. Above lasing threshold, small changes in the injected carrier density $\frac{\partial N}{\partial t}$ produce a like change in photon density $\frac{\partial S}{\partial t}$, so that the gain curve is said to be "clamped" to the loss curve. If the carrier density increases too fast for the photon density to compensate, population inversion builds, and the gain curve rises. The photon density then exhibits a sharp increase until the two (gain/loss) are again balanced; this sharp increase is the gain switch. Subsequent to the switching, the interaction of the carrier and photon density changes can result in oscillatory behavior in the lasing output [47], so that the switch and relaxation oscillations are symptoms by which gain switching may be examined. As the switching speed is increased, the carrier density increase rises more sharply than the photon density increase, and the switch intensity grows. Gain switching in GaAs is expected to occur for switching speeds faster than the carrier lifetime [47], which is < 1 nsec [12]. The switching speeds evidenced in the thermal response of the VCSEL are much slower (> 1 μsec) and are not

53
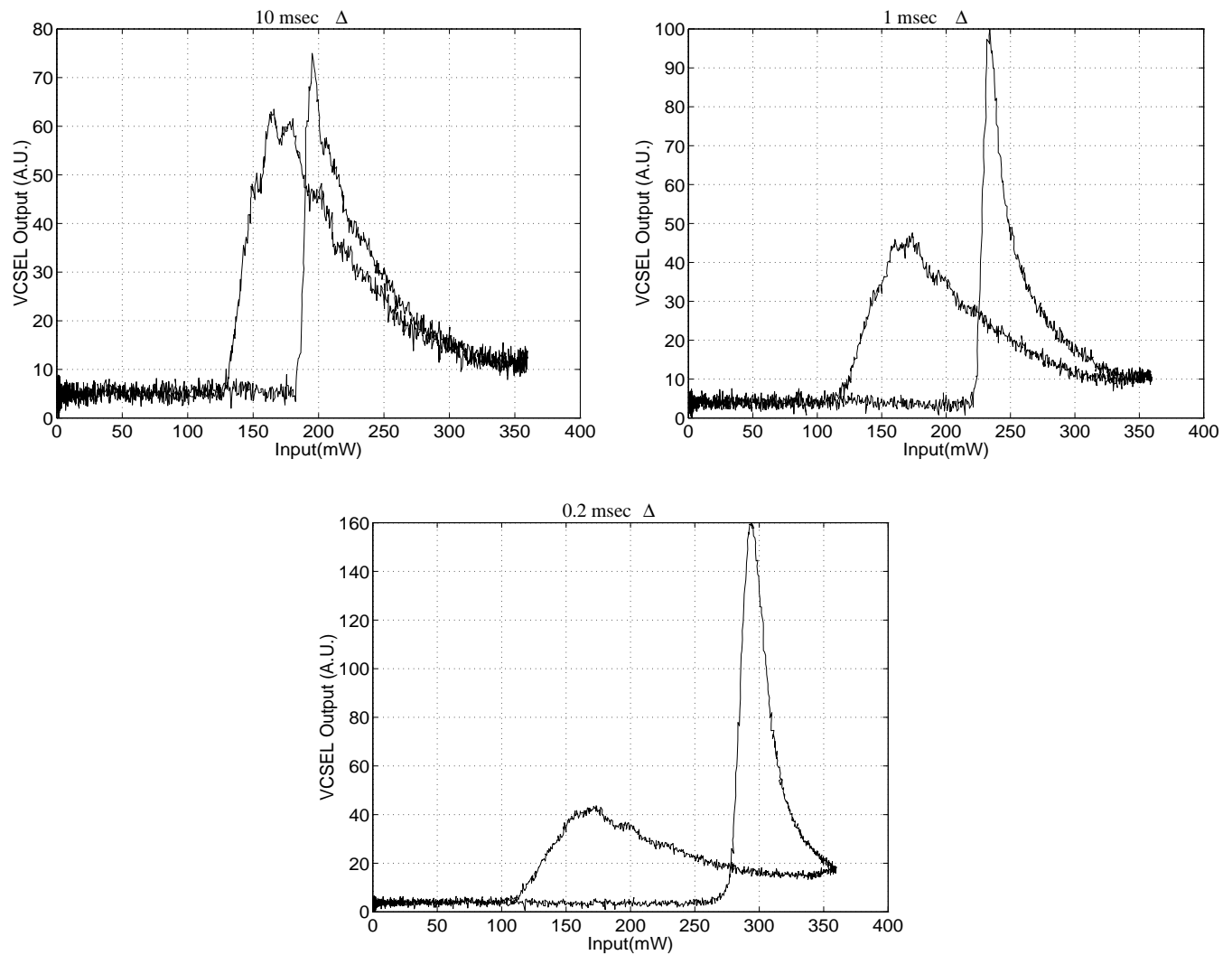
Figure 39.   Switching Overshoot in VCSEL Lasing Output as Triangle Input Intensity Speed is
            Increased (Sample 1)

accompanied by relaxation oscillations; for this reason, it is unlikely that these output spikes are
gain-switch-associated.

A more likely scenario is that the combination of the increase in input power at switch-down
and lattice heating combine to produce the spiking. At switch-down, the increased input power
shifts the gain curve up (increasing N in figure 40 (left)). The lasing output power rises with the
increased gain, then the lattice heating begins to compress the gain curve as in figure 40 (right). The
decreasing gain lowers the lasing output power on the thermal (μsec) time scale. Additionally, the

increased heating continues to shift the cavity resonance/lasing wavelength to longer wavelengths, which selects progressively smaller values of gain. The output power decreases as a result.
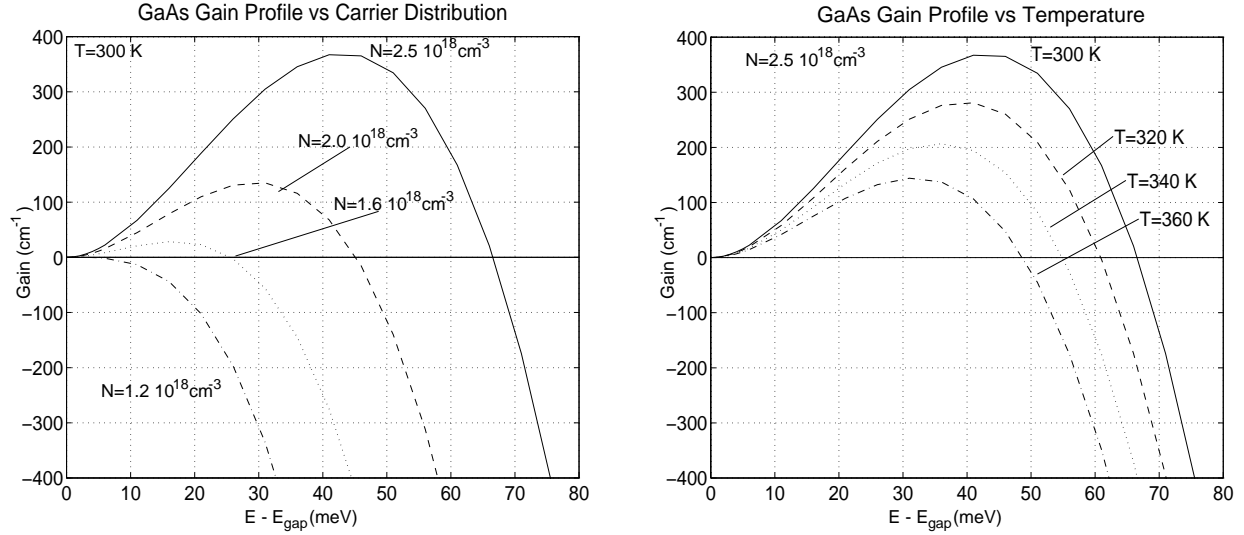
Figure 40. Gain Changes in GaAs for Changes in Carrier Density and Temperature

As the triangle speed increases, the output power spike increases. This is because the reflectivity switch-down point occurs at higher intensities, as seen in the DBR (see figure 24 and figure 25). The increase in the input power at switch-down increases, producing a higher jump in switched intensity for faster triangle speeds.

A plot of the equivalent reflectivity bistability indicates the transitions in the reflectivity correspond to the output pulse in the VCSEL. Figure 41 overlays the output reflectivity triangle and the VCSEL output pulses. At reflectivity switch-up, no spike in the lasing output is present because the pump intensity in the cavity *decreases*. The pulse width is approximately 5 μsec, measured as the half width of the pulse (first peak) above the equivalent CW lasing intensity.

3.4.2.4 Wavelength Bistability. Once it was apparent the thermal distribution in the VCSEL was producing the bistability, it was expected that the elevated temperature in the VCSEL cavity should exhibit a bistable wavelength jump. That is, below bistability threshold, the temperature of the cavity would present an optical path length of $n_L D$ for the Fabry-Perot resonance, which selects the lasing wavelength. The increased pump intensity after reflectivity switch-down

55
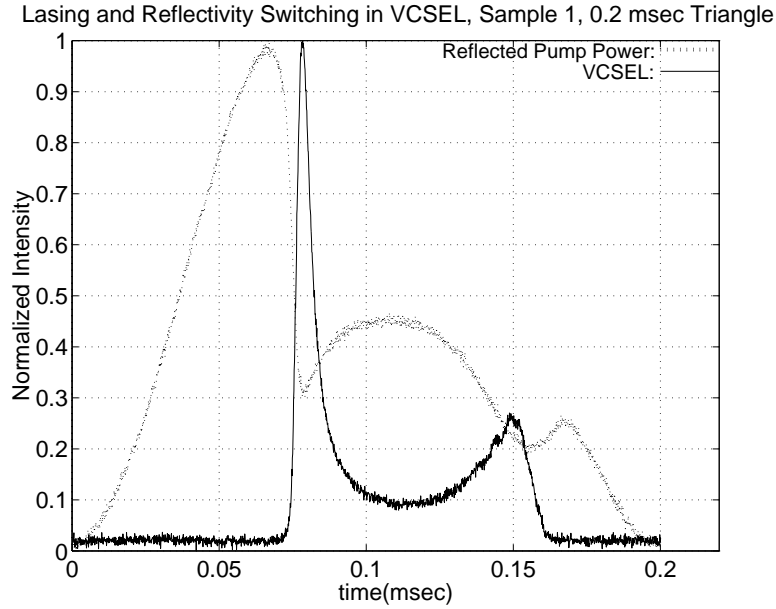
Figure 41. Comparison of Reflectivity Switching of VCSEL to Switched Output (Sample 1)

results in an increase in the power absorbed by the cavity, which heats up. Some of this power is lost to the lasing mode, but much of it contributes to lattice heating. The rise in temperature increases the optical path length $n_L D \Rightarrow (n_L + \Delta n)D$, which shifts the Fabry-Perot dip, and lasing, to longer wavelengths. The wavelength jump was exhibited in all bistable lasing samples. An example of one lasing wavelength jump is shown in figure 42.

The variety of pump wavelengths, input powers, and samples resulted in a diverse wavelength jump response. The wavelength jumps ranged in value from $\Delta\lambda_{las} = 1.1$ nm to $\Delta\lambda_{las} = 9.6$ nm. Almost invariably, the further up the stop-band slope the pump wavelength was positioned, the greater was the wavelength change. A table of wavelength bistability changes is included in table 2 below. The table is included to indicate the $\Delta\lambda_{las}$ evidenced in these samples. As the spectral location of the pump with respect to the stop band is critical, its location, and that of the pump minimum are included. The curvature of the stop band edge would also be helpful, but collection of this item for all locations would require a time-consuming absolute reflectivity measurement along the stop band edge, which was not performed.
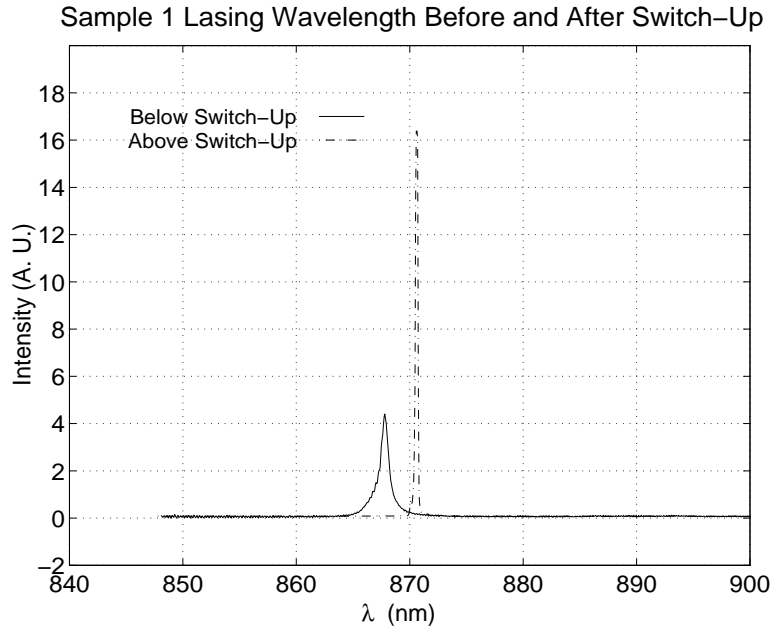
Figure 42. Lasing Wavelength Bistability in VCSEL (Sample 1)

Table 2. Lasing Wavelength Changes in Sample VCSELs

Sample:	$\Delta\lambda_{las}$ (nm)	λ_{pump} (nm)	$\lambda_{pump\ min}$ (nm)	$\Delta\lambda_{pm\Rightarrow p}$ (nm)
1	1.1	843.8	840.1	3.7
	2.8	827.0	822.7	4.3
	2.8	813.6	808.9	4.7
	3.1	842.5	837.7	4.8
	3.5	839.0	835.7	3.3
	4.4	842.7	836.7	6.0
2	2.4	827.7	820.2	7.5
	3.4	827.7	819.6	8.1
3	4.1	826.7	815.3	11.4
	7.8	841.4	832.8	8.6
	9.6	838.4	829.2	9.2

The $\Delta\lambda_{las}$ for Sample 1 indicate the location of the pump with respect to the pump minimum has a bearing on the wavelength jump. Except for the 3.5 nm $\Delta\lambda_{las}$ entry, as $\lambda_{pump\ min}$–to–λ_{pump} separation increases, so does $\Delta\lambda_{las}$. The spectral distance between $\lambda_{pump\ min}$ and λ_{pump} indicates roughly how far up the stop band slope the pump wavelength is positioned. This same relationship is borne out in Samples 2 and 3 in the table.

The wavelength jumps in Sample 3 are much larger than in Samples 1 and 2. The change in Δn is the result of a higher cavity temperature, not a scaling of the jump because of the longer cavity. Using the relationship between the design wavelength (λ_d), the cavity length (d) and the room temperature index n_0: $n_0 d = 3\lambda_d$ for Sample 1. The change in index for a jump from λ_1 to λ_2 for Sample 1 is given by:

$$
\begin{aligned}
n_1 d = 3\lambda_1 \quad &, \quad n_2 d = 3\lambda_2 \\
\Rightarrow (n_2 - n_1)d \ &= \ 3(\lambda_2 - \lambda_1) \\
\Delta n \ &= \ \frac{3\Delta\lambda}{d} \\
&= \ \frac{3\Delta\lambda}{(3\lambda_d)/n_0} \\
\Rightarrow \Delta n \ &= \ \frac{\Delta\lambda n_0}{2\lambda_d}
\end{aligned}
\tag{17}
$$

This equation holds regardless of the cavity thickness; if λ_d is the same for the two cavities, the cavity thickness does not *directly* effect Δn through equation 17. Since Δn scales with temperature, Sample 3's cavity must have a higher temperature than Samples 1 and 2. Sample 3's higher cavity temperature is due to its increased absorption, which produces larger temperatures in the cavity, increasing its index with respect to the 3 λ_d cavity for Samples 1 and 2. In this respect, the cavity thickness *indirectly* effects Δn by increasing the absorbed power.

Table 2 indicates a larger $\lambda_{pump\ min}$–to–λ_{pump} separation produces a larger $\Delta\lambda$. The cause of this behavior is that as the pump wavelength is tuned to higher reflectivities on the stop-band slope, greater intensity is required to produce the nonlinearity necessary for switching. Once the switch occurs, the jump in pump intensity reaching the cavity, and hence the temperature rise, is greater.

The wavelength jump provides an opportunity to measure the increase in temperature of the VCSEL. The position of the Fabry-Perot resonance is a product of the cavity thickness and refractive index. Penetration depth into the mirrors is significant, but affects resonance little, as only those wavelengths which correspond to the cavity resonance phase-match to form the resonant dip in reflectivity. So this piece of data allows the determination of the temperature of the cavity, namely, the resonance selects the lasing wavelength, so the shift in lasing wavelength provides the shift in resonance. The thermal expansion of the cavity should be negligible [37], so the change in resonance can be attributed to the change in the index of refraction. The ellipsometry data provides the relationship between Δn and ΔT. The relationship between Δn and $\Delta\lambda$ is given by equation 17.

Calculating the temperature rise for each of the wavelength jumps encountered provided a range of temperatures from 39° C (Sample 1) to 140° C (Sample 3). The model predicts for VCSELs of the same construction as Sample 1, a temperature jump in the cavity at reflectivity switch-down. Depending on where the pump wavelength was positioned, a range of 50 - 110° C occurred. A plot of the calculated temperature distribution along the centerline of the mathematically modeled VCSEL is provided in figure 43. The plot data was calculated for a VCSEL matching the structure of Sample 1 (3 λ cavity). The surface plot shows temperature in each layer vs input intensity. The intensity axis represents the intensity along the triangle wave input intensity, and reaches peak intensity at 50 in the plot y scale (labeled *max* on the figure). It is evident from the plot that the maximum temperature is reached in the gain region (on the plot, layers 45-56). The sharp features along the intensity scale are, of course, the intensities for which the reflectivity switches.

3.4.2.5 Longitudinal Mode Selection. The wavelength of the Fabry-Perot resonance is given by:

$$\lambda_{FP} = \frac{2nd}{m} \tag{18}$$

with n being the cavity index, d the physical thickness, and m an integer. As mentioned in the structural descriptions of the VCSEL samples, Samples 1 and 2 had cavity lengths 3 λ_d thick. The longitudinal mode separation of these cavities is computed by equation 18. The separation is the spectral distance between adjacent values of m in that equation. For example, a 3 λ thick cavity
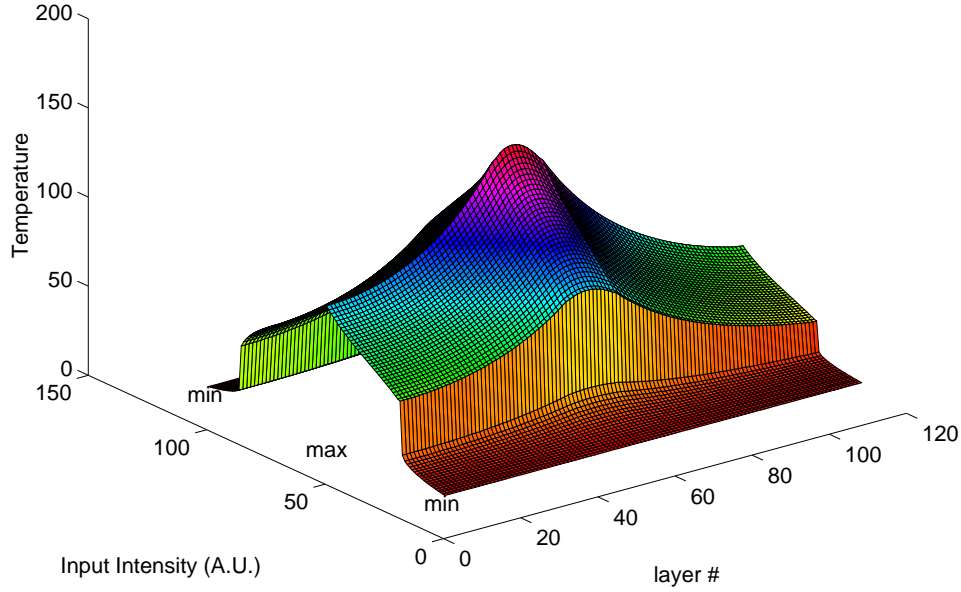
Figure 43. Calculated Temperature Distribution in VCSEL Layers, vs Input Intensity along the VCSEL centerline

($\lambda_d = 884$ nm), neglecting penetration depth into the DBR mirrors, has a spectral separation between modes: $\Delta\lambda_{lm} = 127$ nm; for a 9 λ cavity, $\Delta\lambda_{lm} = 47$ nm. In the 3 λ case, this spectral separation is enough to have only one resonant dip inside the stop band of spectral width ~ 100 nm (see figure 2 in Chapter I). The smaller $\Delta\lambda_{lm}$ for the 9 λ cavity allows more than one longitudinal mode to reside under the stop band. A plot of the measured spectral reflectivity for Sample 3 is shown in figure 44 below, showing two resonances.

The resonance selects the lasing wavelength for the VCSEL. If under excitation of the gain region there is sufficient gain at the resonance to overcome losses, the VCSEL will lase at that wavelength. Depending on the gain configuration and the reflectivities of the mirrors, Sample 3's 9 λ cavity could lase at either or both resonances. In establishing the bistability behavior of Sample 3, it was found that depending on the arm of the bistability the configuration could select a wavelength and switch to the other longitudinal mode by undergoing the reflectivity switch (increasing or decreasing pump intensity). The two modes selected are pictured spectrally in figure 45 below. The spectral
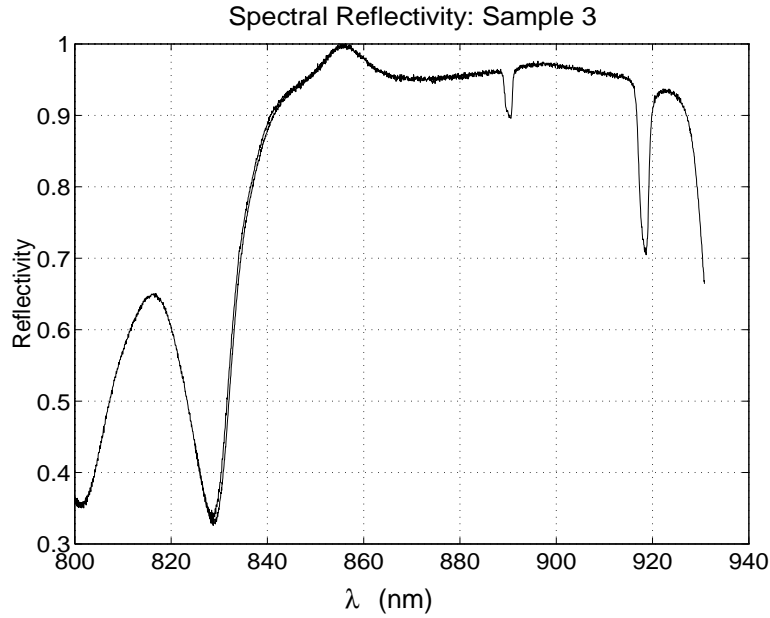
Figure 44. Spectral Reflectivity of Sample 3, Showing Two Resonances

separation between modes is 31 nm. The shorter longitudinal mode separation (47 nm was predicted for 9 λ cavity above) is due to the penetration depth of the lasing mode into the mirrors, which lengthens the cavity and shortens $\Delta\lambda_{lm}$.
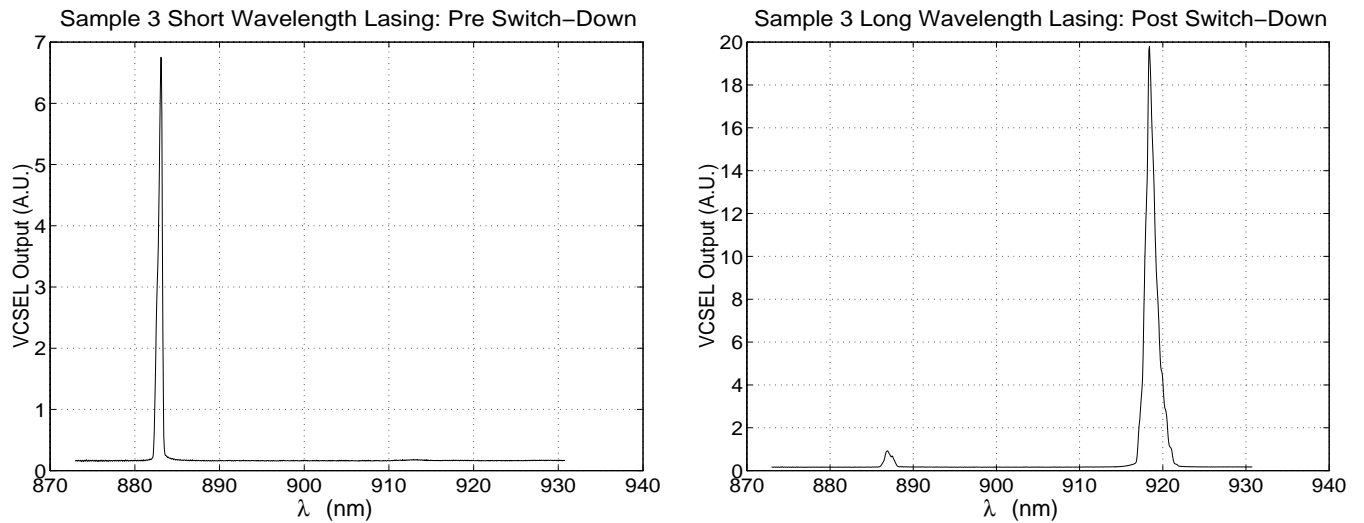
Figure 45. Plots of VCSEL Sample 3 Lasing Spectrum, Showing Two Stable Lasing Wavelengths, Switchable by Input Power

Sample 3 also exhibited switching at each arm of the reflectivity bistability (see figure 46). The switch-down produced a pulse at the long wavelength (918 nm) and the switch-up produced a pulse at the short wavelength (887 nm). The comparison of the output reflectivity to the lasing output of the VCSEL shows the coincident nature of the reflectivity switching to the pulsed VCSEL outputs. The FWHM speed for switch-down (the first pulse in figure 46) was 15 μsec, while FWHM speed for switch-up was 27 μsec.
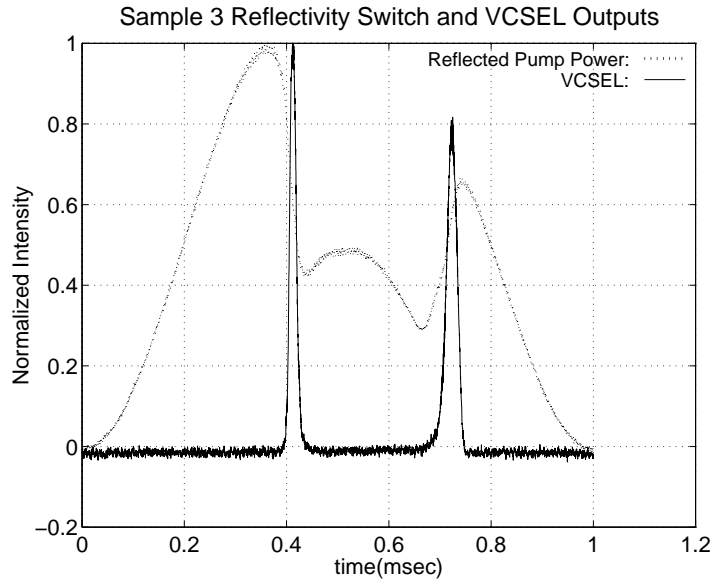
Figure 46. VCSEL Sample 3 Reflected Signal and VCSEL Switched Outputs

3.4.2.6 Spot Size Bistability. A third change in the VCSEL output lasing behavior at each leg of the bistability was a visible decrease in spot size at reflectivity switch-down and a reciprocal increase in spot size at reflectivity switch-up. Pictures of the spot behavior are shown in figure 47. Each beam was individually attenuated using a neutral density filter (NDF) to prevent camera saturation.

The intensities of these profiles were digitized, and a comparison of the cross section of the normalized intensities provides a measure of the decrease in spot size. The cross-sections of the profiles are compared in figure 48 below. Comparing the $\frac{1}{e^2}$ widths for each, the spot size reduces to approximately 36 % of the pre-switch $\frac{1}{e^2}$ width.
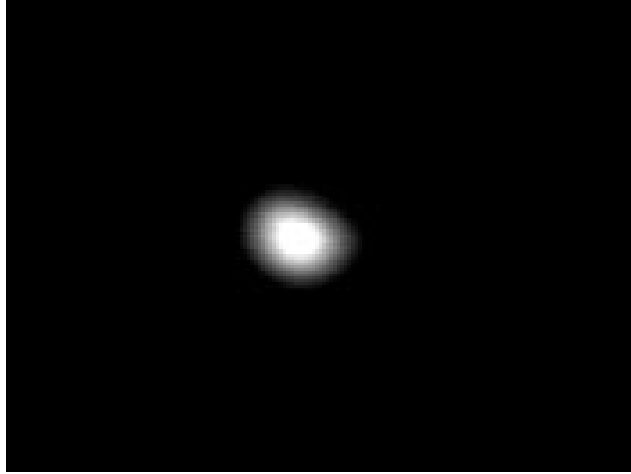
Pre Switch-Down (NDF=0.5)　　　　　　　　　　　　　　　Post Switch-Down (NDF=3.0)
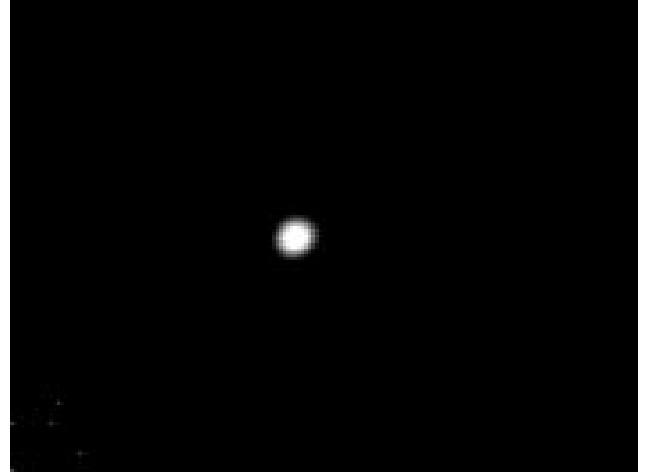
Figure 47. Lasing Spot Profiles Below(Pre) and Above(Post) Switch-Down, Sample 1
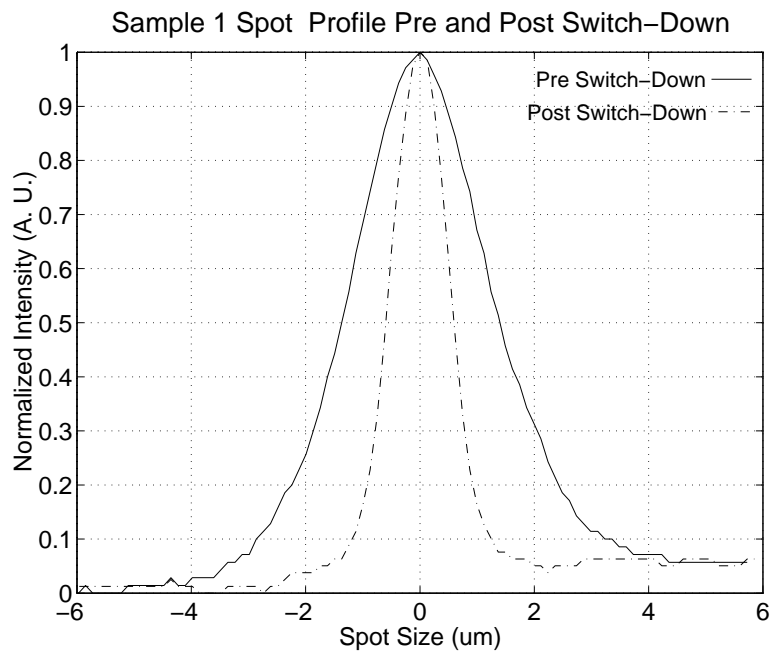
Figure 48. Line Profiles of Spot Intensity, Below- and Above-Switch-Down: Sample 1

Radial Index Profile. Self-focusing of the VCSEL structure seemed the likely cause of this phenomenon. Surface plots of the calculated temperature distribution in the radial direction at switch-down are shown in figure 49. The 3-D plot merely indicates the radial distribution is symmetric about a cylinder cut-out of the VCSEL layers. The maximum temperature is encountered in the high-absorption gain region. The surface plot of the radial profiles pre- and post- reflectivity switch-down is more useful. It indicates both the increase in temperature and the shape of the radial temperature profile in the VCSEL. The refractive index profile which coincides with this temperature profile is obtained by using ΔT for each layer and determining Δn from it, the layer's x-concentration, and the wavelength of interest. Ellipsometry data is used to get Δn for GaAs, while other x concentrations are handled via the SEO model introduced in chapter II.

The computed index changes given the radial temperature profiles at the pump wavelength and the lasing wavelength for the modeled structure are shown in figure 50. The shape of these profiles indicates a larger Δn along the centerline of the incident pump than at the edges. This tapered profile produces a self focusing medium: it slows the central part of the beam relative to the edges of the beam. The lensing effect results in the spot size change in figures 47 and 48 .

There is a sharp drop in the index change for the GaAs cavity and substrate layers at λ= 842 nm in figure 50. This pump wavelength is approximately 50 meV above the band gap (E_g = 1.42 eV) and as can be seen from the plots (see fig 51) of the ellipsometry data, this region has a much smaller variation in index for temperature increases than the below-band ($< E_g$) excitation energies. When we reach the VCSEL wavelength (λ = 884 nm) the Δn profile for GaAs layers in figure 50 has reached and surpassed the levels of the AlGaAs mirror layers.
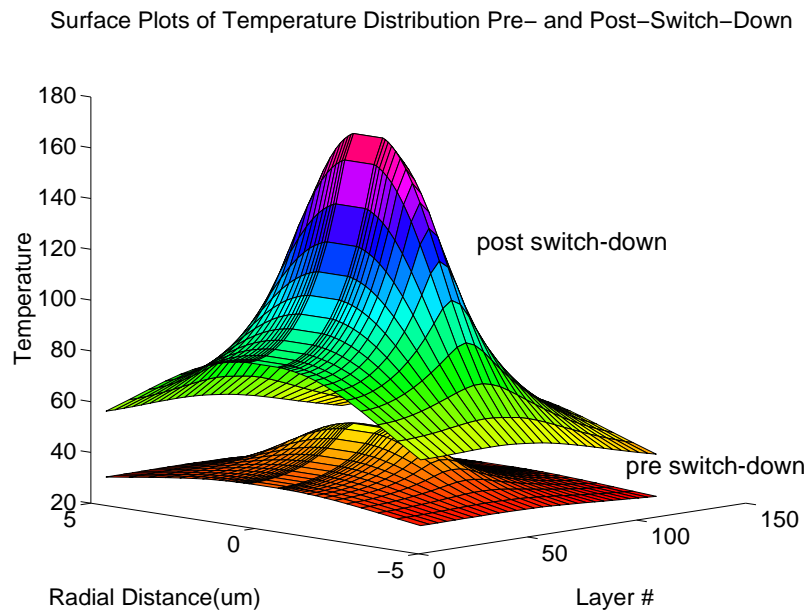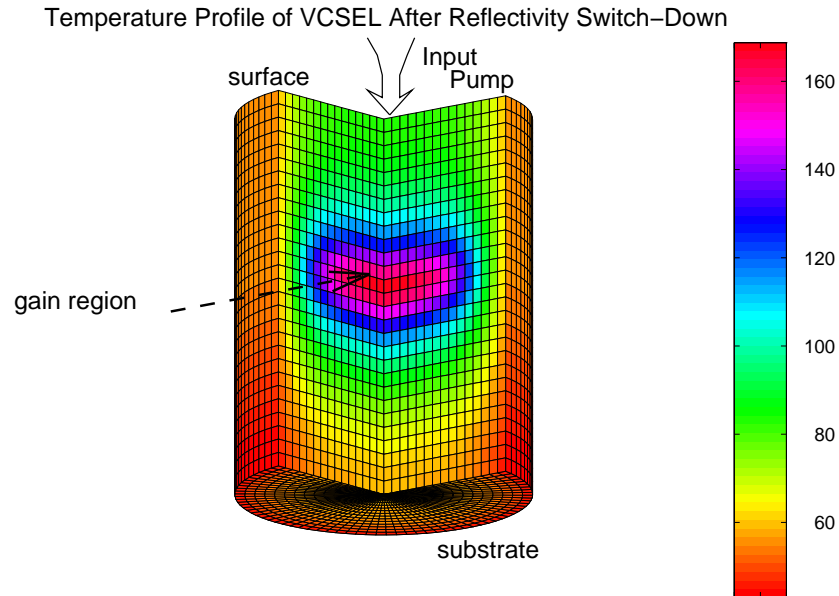
Figure 49. Cut-out of VCSEL Showing Laser Heating Just after Switch-Down & Surface Plot of Radial Temperature Distribution
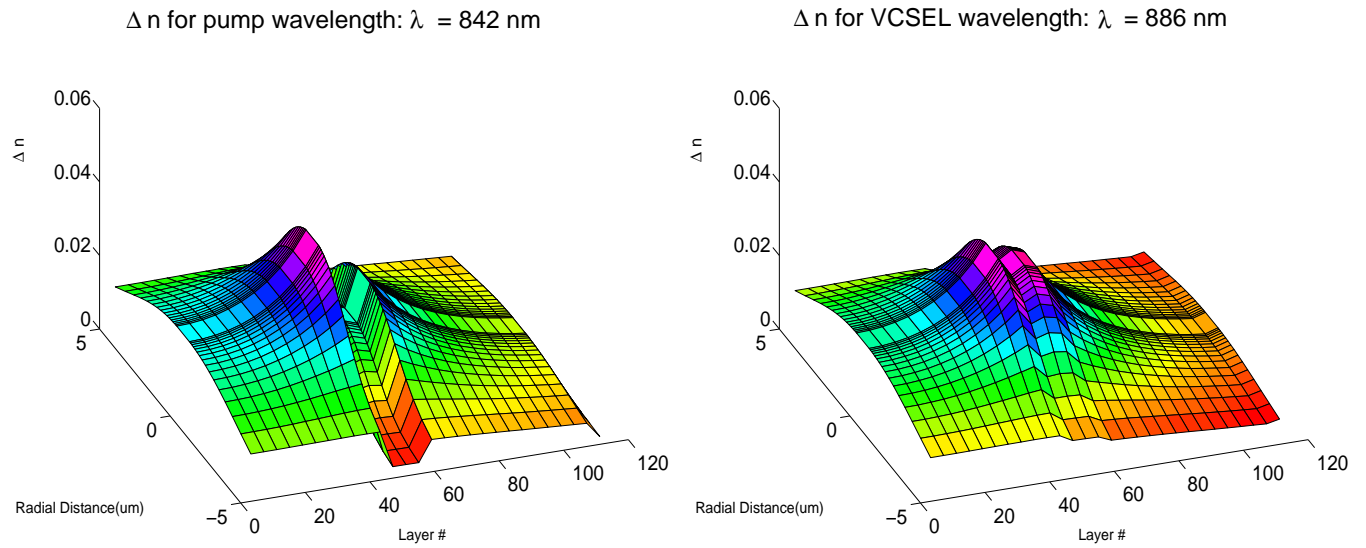
Figure 50.   Radial Change in Refractive Index Due to Heating of VCSEL: at Pump Wavelength
($\lambda = 842$ nm) and at VCSEL Lasing Wavelength ($\lambda = 884$ nm)
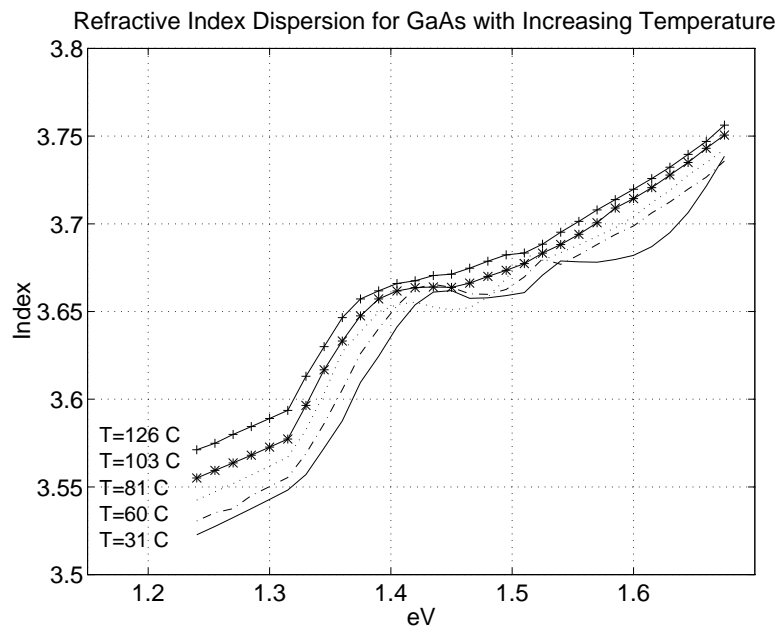
Figure 51. GaAs Index Dispersion as Temperature is Increased

66

This chapter has related the experimental results for the DBR mirror and VCSEL samples. Both are reported here because they are linked in behavior. The DBR, as a simpler structure, helps to begin sorting out the causes of the various bistable reactions. Initially, this thermal bistability was discovered in VCSEL samples. In examining the possible driving mechanisms for the bistable reaction, the complexities of the two-DBR-plus-cavity structure prevented positively attributing the bistability to the changing reflectivities of the DBR mirrors. The demonstration of DBR mirror reflectivity switching was important to the separation of the various bistable phenomena in the VCSEL behavior.

Regarding the mechanisms driving the bistability, the modeling has contributed further insight. Although the mathematical model, by necessity, is a simplified version of the actual dynamics, it was useful in verifying much of the bistable behavior. The experimentally measured VCSEL lasing wavelength shift indicates the range of cavity temperatures predicted by the model is reasonable. The widening of the bistability hysteresis for increasing input speeds and for longer pump wavelengths was verified by the model. The magnitude of the measured reflectivity jumps indicate good agreement with the model, the jump in reflectivity being from the upper edge of the stop band to the vicinity of the pump minimum. Finally, the model allowed a radial description of the lensing in the VCSEL.

It is important to note that the power requirements for the switching seen here are high. The bistable operation in the DBR required minimally 300 mW into the focusing lens above the DBR to be able to switch. This delivers 66 mW/μm^2, or 6.6 MW/cm^2. These powers are too high to be practical in most switching applications. The optical bistability produced by Acklin *et al* using a hybrid DBR/linear mirror arrangement has resulted in switching at 0.15 mW/μm^2. That arrangement, however, used a linear mirror below the DBR and a phase-matching layer. The combination was tailored to accentuate the field strength in the DBR layers which provide maximal nonlinear index change. The switching was not stable in that thermal effects would terminate the switch after $\sim 1\mu$sec. In many ways, Acklin's device is more like the VCSEL, in that a resonant cavity contributes to the index shift. The VCSEL samples used here had smaller power requirements (< 26mW/μm^2) than the DBR, but still required much higher pump intensity than Acklin's hybrid device. Of course, the

VCSEL also lases bistably, which contributes to its usefulness. Tailoring the cavity/mirror layers will improve performance. A steeper stop band slope would allow closer proximity of the inflection point to the pump wavelength, and increase the benefits of the resonant cavity in decreasing the switching intensity required. This would require an increased number of mirror layers, but might help to achieve the switching thresholds in Acklin's presentation, which are competitive in threshold with nonlinear Fabry-Perot devices [1]. Also, the thermal behavior driving the switch results in this switch being slower than desired. To compete with the fastest electronics switching, the optical switching must approach the picosecond scale. In the next chapter, pulsed inputs achieve this result. The description of the mathematical model will be completed in chapter V, after the discussion on ultrafast switching of the VCSEL/DBR.

IV. Carrier-Generated Optical Switching in $Al_x Ga_{1-x} As$ DBR mirrors & VCSELs

The examination of reflective bistability in the DBR mirror and VCSELs indicated immediately that the probable cause was the thermally driven refractive index nonlinearity. Knowing that the carrier-generated nonlinearities discussed in chapter II can work on a much faster time scale ($< 10^{-12}$ sec as compared to the 10^{-6} sec response times for the thermal nonlinearity) drove a desire to determine if such ultrafast switching was achievable in the VCSEL or DBR. This chapter discusses the experiments and results for the ultrafast switching of $Al_x Ga_{1-x} As$ DBRs and VCSELs.

4.1 Previous Work

As discussed in chapter III, bistability in distributed feedback structures was proposed as early as 1979 [44]. GaAs/AlAs Bragg reflectors were demonstrated with 20 nsec switching speeds, a 2:1 contrast ratio, and 4 mW threshold (.14 mW/μm^2) [25] in 1988. Recently, researchers at the University of Nova Scotia demonstrated the reflectivity switching of a periodic multi-layered thin film reflector, using the refractive index nonlinearity at the long wavelength edge of the stop band [1]. As outlined in chapter III, they used a DBR grown atop a high reflectivity linear mirror, and a phase matching layer, to effect the DBR switching. The group achieved switching speeds near 4 nsec [19], with 3:1 contrast ratio. These are the fastest published reflectivity transitions for DBR stacks. Hultgren's work [20] indicates the psec refractive index nonlinearity caused by carrier heating is not only reasonably strong in AlGaAs, but can be controlled to some degree by carrier injection. This experiment represents the first demonstration of picosecond reflectivity switching in DBR structures, in addition, no reflectivity switch has as yet been established for the VCSEL and a comparison of it to the DBR response could indicate if the addition of mirror layers or cavities can assist in the transition strength or speed.

The speed of the expected transitions for the ultrafast nonlinearity is too fast a transient for time-resolved recovery by typical electronic techniques. The pump-probe method is one technique by which sub-picosecond nonlinearities can be examined. In this experiment the pulsed output of the TiS system (switchable between picosecond (< 2 psec pulsed) and femtosecond (< 200 fsec pulses)) was used to generate both pump and probe signals (see figure 52). Equipment specifications are contained in appendix B.
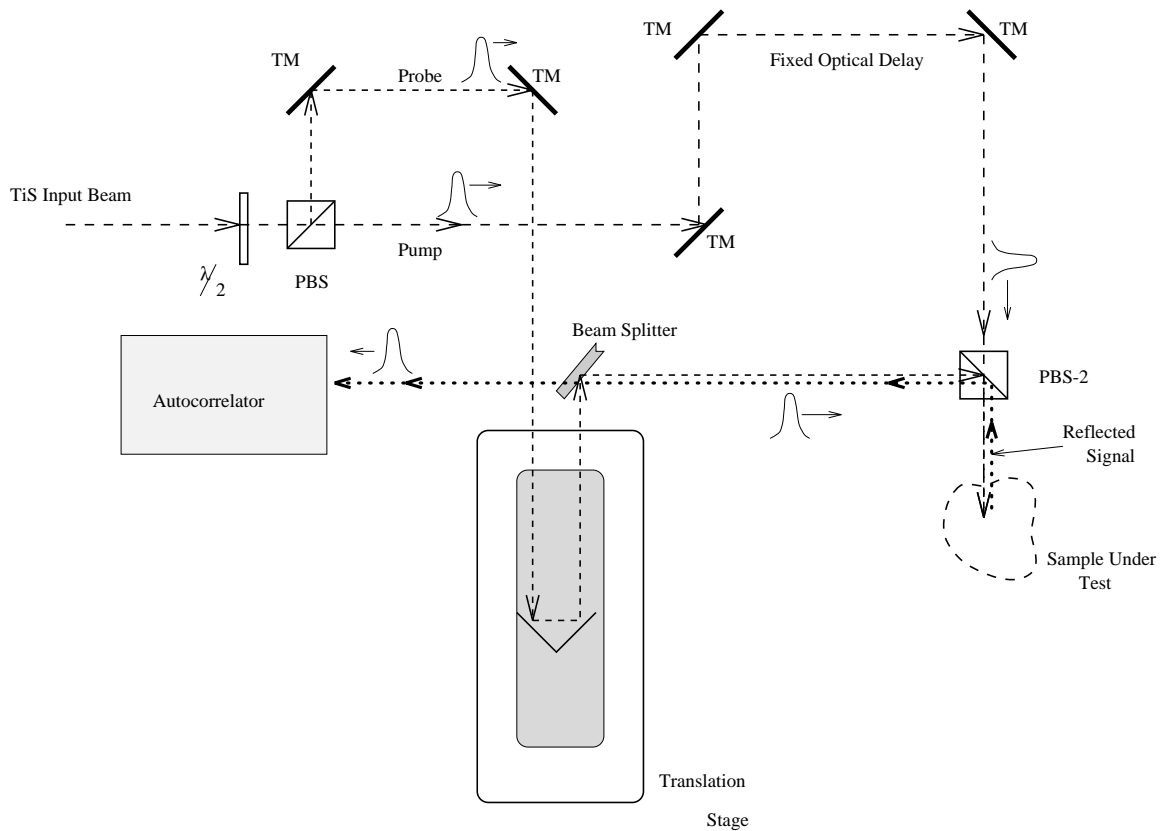
Figure 52. Pump-Probe Experimental Configuration

The horizontally polarized output of the TiS was passed through a $\lambda/2$ waveplate to rotate the beam's linear polarization. A polarizing beamsplitter (PBS) cube selected one polarization (vertical) as probe, and passed the other (horizontal) as the pump. The $\lambda/2$ plate and PBS were used to control the relative strengths of each (pump/probe) leg. Both pump and probe were then recombined at

another PBS (PBS-2) and focused into the sample under test. A fixed optical delay was placed in the pump path, and a variable delay stage (motorized) in the probe path. The probe was delayed by placing its mirrors (actually a corner cube) on the delay stage, making the delay in the probe path selectable. After combining the two pulse paths at the second PBS, they were focused onto the sample. The reflected output was then passed back through PBS-2, which reflects the vertically polarized probe and passes it to the autocorrelator. The autocorrelator measures the arriving pulse, presenting a time-resolved trace of it. Actually, the autocorrelator itself uses the pump-probe technique to form its output, splitting the arriving pulse into two, varying the delay on one leg, then recombining them in a KDP crystal and measuring the second-harmonic signal generated as its indication of the time-resolved intensity of the input pulse. A plot of the typical output of the autocorrelator for probe signal input is shown in figure 53.
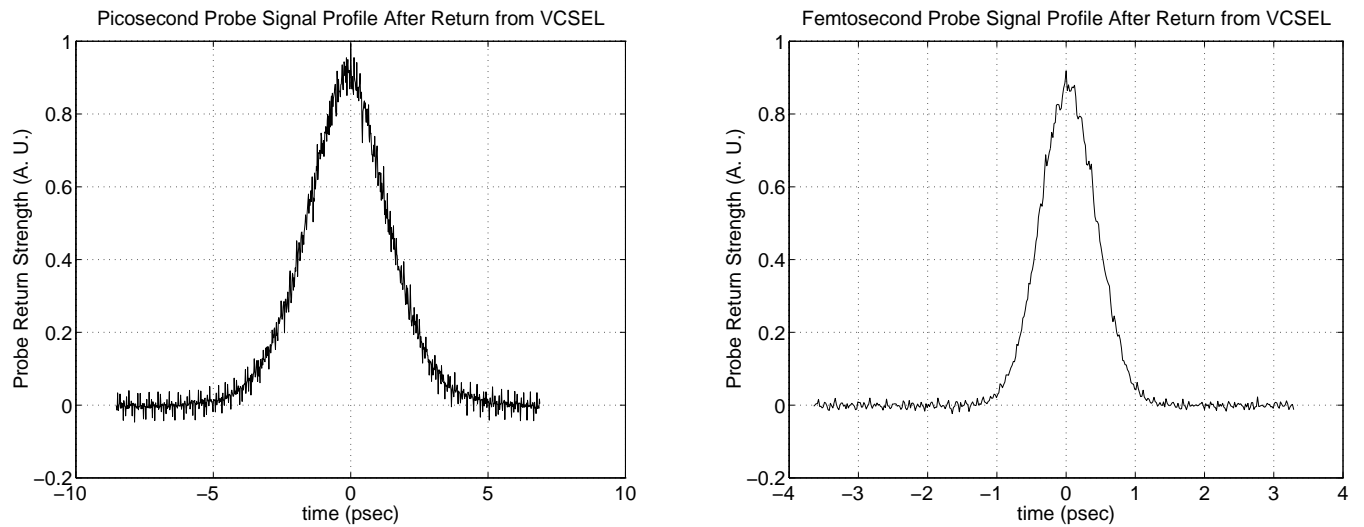
Figure 53. Profiles of Probe Signal for Picosecond and Femtosecond Pulses

The autocorrelator signals depicted in figure 53 represent a convolution of the actual probe signal entering the autocorrelator. The picosecond pulse displayed represents a pulse width (Full Width at Half Maximum) of 2 psec. The femtosecond pulse has FWHM=600fsec. The femtosecond pulse has undergone significant dispersion in the corner cube and both PBS cubes. The ultrafast nature of the femtosecond pulse requires that it contain a significant bandwidth. If this signal is passed though a dispersive medium, it selectively slows the longer wavelengths. This action spreads the pulse in

71

time. As mentioned before, the TiS femtosecond output is specified as < 200 fsec. Measurement without the dispersive elements indicated a pulse width at 110 fsec. As many dispersive elements as possible were removed from the configuration. Of the remaining elements, the main sources of significant dispersion were an optical isolator, pulse selector, two PBS cubes (one of which was traversed twice) and the corner cube. Passing the pulse through these spread the pulse to 600 fsec. Prior to completing measurements, dispersion from each element was measured so that its effect could be weighed. This also allowed determination of the actual pulse width entering the VCSEL/DBR. If we back out the dispersion of PBS-2, the probe pulse width entering the VCSEL was approximately 500 fsec. The pump pulse width was estimated at FWHM = 410 fsec.

The procedure for measurement was straightforward, the pump and probe were focused onto the sample. The zero-optical delay point was determined by viewing both pump and probe on the autocorrelator and adjusting the delay stage to make them coincide. The estimated error in zero delay point in this method was approximately .5 psec for the picosecond pulses, and approximately 200 fsec for the femtosecond pulses. The sharpness of the femtosecond response on the autocorrelator allowed the sharper distinction in pulse separation, which was governed by the Rayleigh criterion for pulse separation.

Once zero delay was determined, the probe was advanced on the delay stage, corresponding to a position in time in which the probe arrives at the VCSEL before the pump pulse (leads the pump). The autocorrelator was set to register the intensity of the peak of the probe signal. Then the delay stage was stepped backward a distance Δs which incrementally changes the pump-probe delay by a time $\Delta t = 2\Delta s/c$. The $.1\mu$m resolution of the delay stage allowed a time resolution for the measurement down to .7 fsec. By sequentially stepping the delay stage and digitally reading the autocorrelator output, the reflected probe was measured as it transitioned from leading the pump to lagging the pump. The peak of the probe response during this transition provides the measure of the reflectivity of the sample. An example of the response of the DBR mirror is shown in figure 54 below. The delay is as indicated by the x scale. The limit on the delay stage length prevented measuring delays larger than 500 psec.
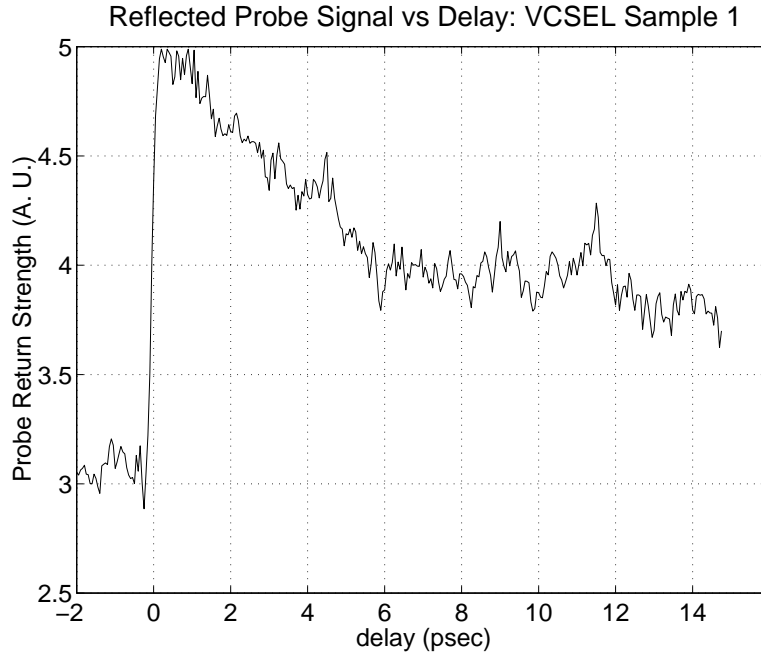
Figure 54. Reflected Probe Strength vs Delay with Respect to Pump Pulse

4.3   Carrier Generated Nonlinearities

Although the ultrafast nonlinearities were discussed in chapter II, it is convenient here to recall the variety of refractive index responses we can expect, based on time scale. The structures tested in this section included a DBR mirror (the same as used in the thermal bistability experiments), and one VCSEL structure. The VCSEL was described in chapter III as Sample 3.

The nonlinear refractive index mechanisms activated in the DBR/VCSEL depend on the strength of the fields delivered and their photon energy (wavelength). We again explored the edge of the stop band to the short wavelength side. This edge provided the necessary sharp reflectivity rise/fall required. The experiments for reflectivity switching could also have spectrally located on the long wavelength edge. This long wavelength edge has been examined for other periodic structures [19]. It was found, for CW input, to have sufficient index shift to produce a bistable response. The short wavelength edge allows the additional incentive of allowing the simultaneous photo-pumping of the cavity, with the eventual possibility of examining the effect of the reflectivity switching on VCSEL lasing output.

73

4.3.1 Femtosecond Response. The contributions of two photon absorption and the optical Stark effect each produced a negative index change in experiments by Hultgren [20] with $Al_{0.05}Ga_{0.95}$. In those experiments, the optical Stark effect contributed an instantaneous transient which grew strongest near resonance. This is supported by the modeling of Sheik-Bahae [41] previously discussed (see chapter II). Although both two photon absorption and the optical Stark effect may contribute to the negative refractive index change measured here, the two effects were not separable using this experimental configuration. The combination of the optical delay presented by the transit of the pulse through the stack and the convolving of pump and probe signals limits the detection of very fast (sub-picosecond) transients. The time required for the optical pulse to transit the structure can be likened to the effective delay of the mirrors. This delay is due to the multiple reflections in the mirrors [4]. For $Al_xGa_{1-x}As$, the index differences in the high (n_N) and low (n_L) index mirror layers is small compared to the average index of the layers ($n_H - n_L << n_{av}$). The reflection delay τ_r for small index differences ($n_{av} \approx n$, the index of the cavity) has been obtained via coupled wave theory [24] as:

$$\tau_r = \frac{n}{c} \frac{\tanh \kappa l}{\kappa} \tag{19}$$

where:
τ_r: reflection delay
n: index of refraction of the cavity
c: speed of light (free space)
κ: coupling coefficient
l: mirror length

The coupling coefficient (κ) for square wave perturbations (as for abrupt index changes in mirror layers) is $\kappa = 2\Delta n/\lambda_0$. Here Δn is the refractive index difference ($n_H - n_L$) in the mirror layers, and λ_0 is the Bragg wavelength.

For a typical AlGaAs VCSEL, $\Delta n \approx .6$, $\lambda_0 = 830$ nm for the pump wavelength, $n = 3.6$, and, for a top mirror of 44 layers, $l \approx 3\mu$m. These parameters produce a delay in reflection of $\tau_r = 8.2$ fsec. This is fast compared to the convolution of pump and probe signals in the experimental configuration. For the femtosecond pulses (500 fsec FWHM) the detected response is a mixing of

signals across an 2 psec time period. Sharper pulse profiles then, would improve the transient capture for this experiment.

4.3.2 Picosecond Response.   Carrier heating dominates the picosecond response. The expected behavior for this index change is a delay in onset of ~ 120 fsec and a relaxation of the carrier heating effect with time constant $\tau_{ch} \approx 1.1$ psec [20]. The index shift for carrier heating is positive. As will be evident in the responses of the samples, carrier heating is a dominant mechanism affecting the reflectivity of the DBR/VCSEL at ultrafast speeds.

4.3.3 Nanosecond Response.   The effect of one- and two-photon absorption is an instantaneous increase in the gain profile. This increase produces a negative refractive index change (via Kramers-Krönig), which is sustained until the carriers can relax to their respective bands. Recombination occurs in AlGaAs on a nanosecond time scale. Other nonlinearities (band filling, bandgap renormalization, exciton screening) also compete in this time scale to form an index dynamic. These effects were not measurable with the experimental configuration used here; their measurement was not pursued as they had already been documented [19, 25] in other work.

4.3.4 Microsecond Response.   The relaxation of the carriers also produces significant lattice heating. This thermal effect on the refractive index was examined in the last chapter. The thermal response is a positive index shift on a μsec time scale. Much of the effort in this section of the experiment was in trying to avoid the thermal effect. The faster responses of the mechanisms discussed above allowed the discrimination of their effect on the refractive index, even with the presence of the stronger thermal nonlinearity. The thermal response was minimized late in the experiment by inserting a pulse selector in the beam path. This allowed the slowing of pulse arrivals down to one every 0.133 sec, if necessary. Before the pulse selector's installation, the pulses arrived at a 76 MHz rate (one every 13.3 nsec), and residual heating from pulse to pulse would remain.

The response of the DBR/VCSEL reflectivity to pulsed excitation depended on the spectral location of the pump on the reflectivity curve, as for the thermal response. The difference here was that the refractive index shift could be positive or negative, depending on the mechanism. According on the sign of the index shift, the spectral shift in the reflectivity curve would be to longer ($+\Delta$n) or shorter ($-\Delta$n) wavelengths. A variety of locations were examined.

4.4.1   VCSEL Response.   The reflectivity spectrum displayed in figure 55 is from VCSEL Sample 3. The sharp peak near the pump minimum indicates the location of the pump wavelength. Picosecond pulsed excitation was delivered to the VCSEL, and measured via the experimental configuration described in section 4.2.
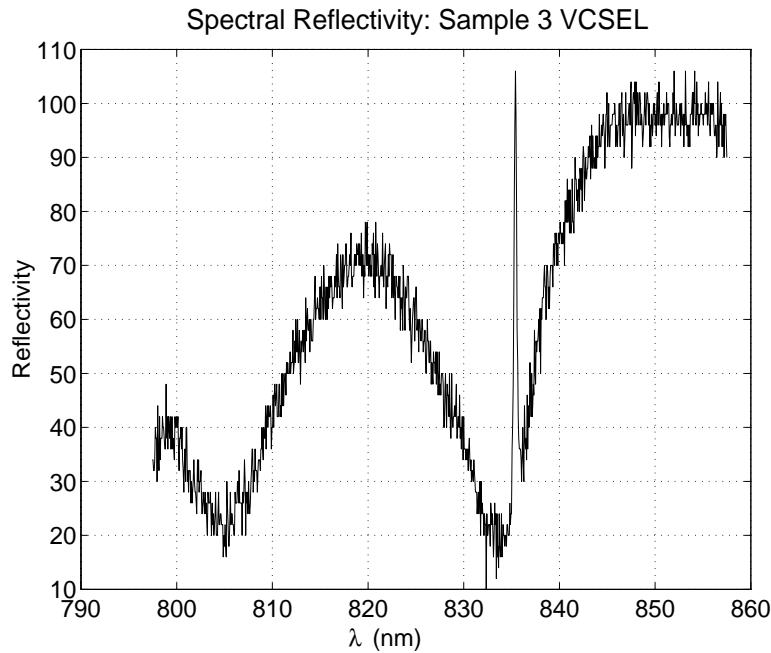
Figure 55.   Reflectivity Spectrum and Pump Wavelength Location: Sample 3 VCSEL, $\lambda_{pump} =$ 835.4 nm

The plot of the reflected probe signal vs. delay in figure 56 shows an initial reflectivity increase, followed by a gradual relaxation of the reflected signal. The output of the pump-probe experiment produces a convolution of the two signals, so that the pulses interact well before their peaks overlap.

76

Because of this, the "zero delay" point was difficult to pinpoint. All plots have been adjusted so the zero delay marks the peak of the interaction. This peak should be near (< 200 fsec) the crossing of the pump and probe peak because the peak is produced by the fast nonlinear response (femtosecond time scale).
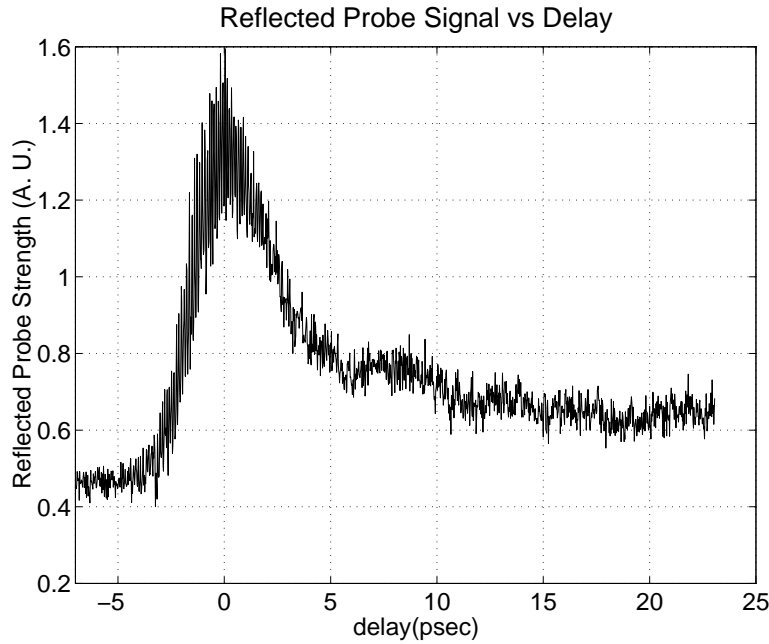
Figure 56. Reflectivity Switching and Relaxation in Sample 3 VCSEL, $\lambda_{pump} = 835.4$, 2 psec Pump Signal

The initial reflectivity increase indicates a negative refractive index shift, attributed to two-photon absorption and the optical Stark effect in the mirror layers, which are undergoing below band excitation for $\lambda_{pump} = 830$ nm, and absorption in the GaAs cavity and substrate which are undergoing above-band excitation ($E_{gap} \approx 868$ nm for GaAs). The mirrors *must* be affected to allow the reflectivity curve to shift. A cavity-only index change would shift only the Fabry-Perot dip and does not explain the reflectivity shift at the stop band edge.

The $-\Delta$n shifts the reflectivity spectrum to shorter wavelengths, increasing the reflectivity the probe experiences. The gradual relaxation of the reflectivity starting at the 1 psec point is due to carrier heating. This can be determined by curve fitting the data, as Hultgren did for AlGaAs [20].

Hultgren used an exponential curve fit to describe the index change in his AlGaAs samples. The response function for the AlGaAs was of the form:

$$h(t) = u(t) \left[a_0 + a_1 (1 - e^{-t/\tau_{delay}}) e^{-t/\tau_{ch}} \right] + a_2 \delta(t) \tag{20}$$

$h(t)$ was then convolved with the known pump profile $G(t)$, and parameters a_x changed to determine the correct fit. The mathematical convolution is necessary because we are comparing to the physical convolution of the pump/probe in the experiment. The terms inside $h(t)$ are:

$u(t)$ step function, forces causality

a_0 stimulated carrier density change

$a_1 (1 - e^{-t/\tau_{delay}}) e^{-t/t_{ch}}$ carrier heating (includes delay time τ_{delay}) of onset and τ_{ch} relaxation time constant

$a_2 \delta(t)$ instantaneous response

The response function, $h(t)$ was then convolved with the pump signal $G(t)$ to form the pump-probe signal:

$$\text{Pump-Probe Signal:} \quad = \int_{-\infty}^{\infty} dt \; h(\tau - t) \cdot G(t) \tag{21}$$

By altering the parameters in $h(t)$, Hultgren arrived at values for τ_{ch} and τ_{delay}. As indicated by figure 57, the exponential curve fit using a time constant for carrier heating of 1.1 psec, fits very closely. This time constant is the same as Hultgren's for AlGaAs refractive index carrier heating. The difficulty in gauging the moment of coincidence of the pulses prevents measuring τ_{delay}. Hultgren estimated τ_{delay} at 120 fsec. The close fit indicates carrier heating is responsible for the relaxation of the reflectivity.

Note that the relaxation of the reflectivity at longer time delays stops short of returning to the pre-pump reflectivity level. The elevated carrier density shifted the reflectivity up, but the carrier heating has not completely canceled the effect. The carriers in the bands do not begin to recombine until ~ 1 nsec. As a result, the elevated carrier densities in the bands maintain a positive Δg which sustains the negative index shift. The negative index shift keeps up the increase in reflectivity. As the next pump arrival is 13.3 nsec away, the carriers do recombine between pump pulse excitations, returning the reflectivity to that indicated at negative delays. Additionally, there is a thermal response
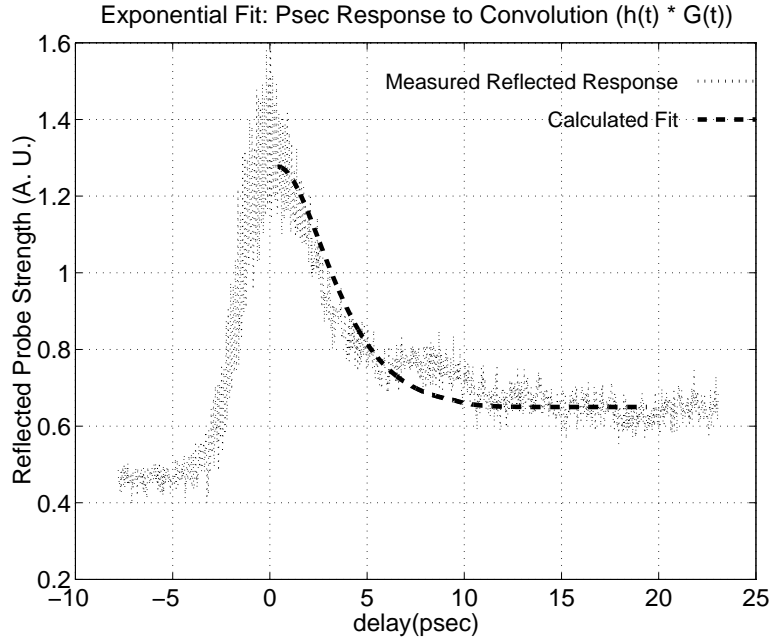
Figure 57.   Exponential Fit to Probe Signal: Sample 3 VCSEL, $\lambda_{pump} = 835.4$, 2 psec Pump Signal

associated with this plot. For early data collection, the pulse selector was not in place, and thermal build-up would pre-shift the reflectivity by producing a $+\Delta$n.

Collection of the reflectivity increase was complicated by the lack of a real time means of comparing the reflected probe with a standard of reflectivity. Substitution of a high reflectance mirror required re-alignment of the configuration and did not guarantee completely reliable reproduction. Instead, the sample remained in place and the pump laser was tuned along the spectral reflectivity curve so that the return signal matched the change in probe output signal from the plots. By this method, a change in pump wavelength correlates to a change in spectral reflectivity from the plot. This change in wavelength was then compared to the spectral reflectivity plot to indicate the reflectivity jump.

For example, in figure 57, the change in probe strength was 1.0 arbitrary units from (0.45 to 1.45); immediately after the curve was collected, the laser wavelength was tuned to higher reflectivities until it matched the 1.45 A.U. signal on the autocorrelator. Care was taken to maintain the same

output power from the TiS reaching the VCSEL. The resultant change in wavelength was recorded as $\Delta\lambda = 7$ nm. Returning to the spectral reflectivity plot in figure 55, a change in wavelength from the pump starting wavelength (835.4 nm), where $R = .3$ takes the plot to 842.4, where the reflectivity is approximately .84. This is a jump in reflectivity of $\Delta R = 54$ %, and a contrast ratio of 3:1. This measurement was typical of the maximum contrast ratio achieved.

Similar results are contained in the following plots. They are plots taken under femtosecond excitation, with the femtosecond pulse width delivered to the VCSEL at 410/500 fsec (pump/probe) FWHM. The spectral profile is as indicated in figure 58. A line indicating pump wavelength has been
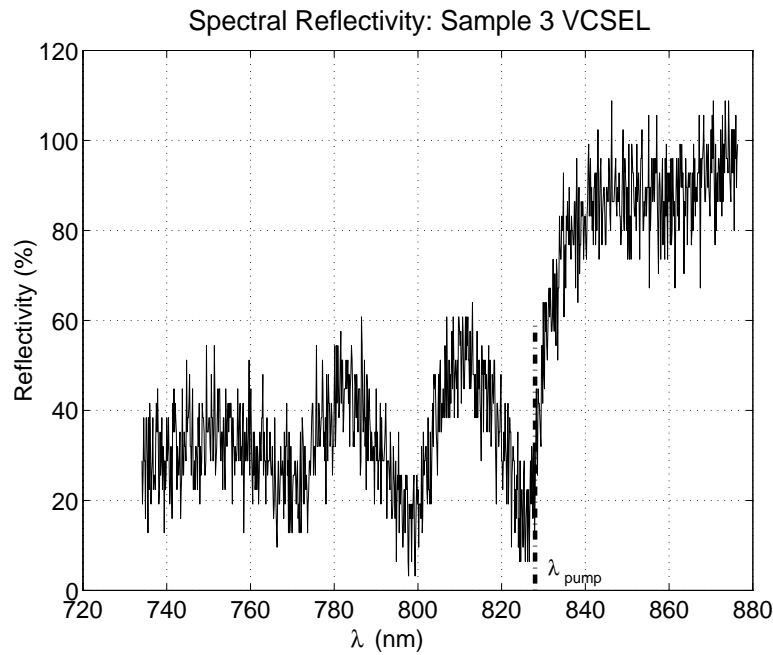
Figure 58.   Reflectivity Spectrum and Pump Wavelength Location: Sample 3 VCSEL, $\lambda_{pump} = 828$ nm

added for reference. the starting location for the pump is near the bottom of the slope of the curve.

The plot below (see figure 59) indicates the sharp increase in reflectivity, as for the previous case. An expansion of the time scale indicates the rise time on this increase is ~ 250 fsec. The faster response of the VCSEL to the sharper 410 fsec pulse indicates sub-picosecond nonlinearities (two-photon absorption) can produce a dramatic reflectivity switching speed. The thermal response
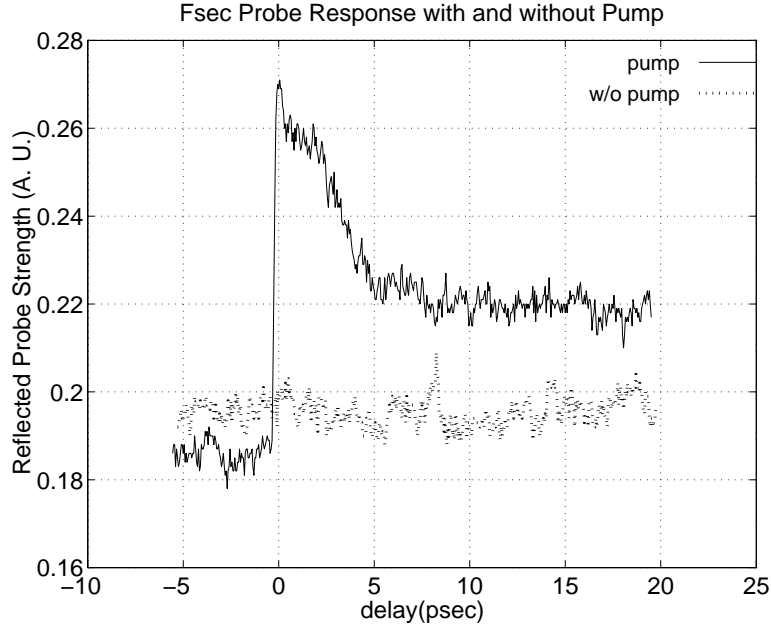
Figure 59. Reflected Signal vs Delay: Sample 3 VCSEL, $\lambda_{pump} = 828$ nm, 410 fsec Pump Pulse

is also indicated on the plot. The lighter line indicating the reflected signal when the pump is absent remains constant (with some noise) for all delays. If there were no thermal response, the 13.3 nsec delay between pulse arrivals would allow the system to relax to this level. The reflectivity shift of the probe to lower values at negative delay (before the pump arrives) indicates the thermal shift is present. The thermal nonlinearity shifts the reflectivity spectrum to longer wavelengths, producing a decreased reflectivity at these negative delays. With the arrival of the pump, the two-photon absorption $-\Delta$n shift moves the reflectivity spectrum to shorter wavelengths, which produces the sharp increase in reflectivity at zero delay. The carrier heating ($+ \Delta$n) then produces the gradual ($\tau_{ch} = 1.1$ psec) exponential decrease in reflectivity.

The curve fit of the femtosecond response is also very close, as indicated in the plot at figure 60. The response for the AlGaAs waveguides Hultgren reported on indicated a delay of 120 fsec. The curve fit for the carrier heating response indicates there is a delay in its onset: there is a more gradual fall in reflectivity in the 0.5 to 3 psec delay range than at later delay times. This is a longer delay than that witnessed by Hultgren. The delay is likely the result of a combination of faster
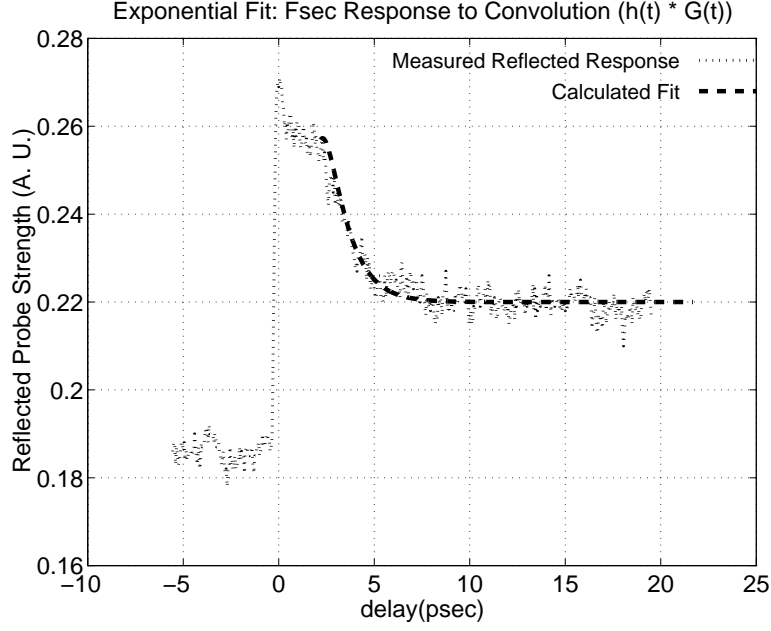
Figure 60. Exponential Fit to Probe Signal: Sample 3 VCSEL, $\lambda_{pump} = 835.4$, 410 fsec Pump Signal

mechanisms. Early in this range, the pump pulse is still present, so that its contribution (carrier density changes and optical Stark effect) to the $-\Delta$n dynamic competes with the carrier heating mechanism. Once the pump intensity is no longer a significant contributor, the carrier heating dynamic is clearly recognizable by the curve fit.

4.4.2   DBR Response.   The DBR produced femtosecond reflectivity switching as well. The spectral location on the DBR for which the plots below were taken is indicated in the spectral reflectivity plot (figure 61).

4.4.2.1   Thermal Response to Pulse Frequency.   The plots in figure 62 indicate that as the pulse repetition is decreased, the thermal component begins to abate.   Note the pre-pump arrival signal in figure 62, as compared to its probe-only signal (labeled w/o pump) shows a significant drop in autocorrelation output. The drop was due to a $+\Delta$n refractive index shift from heating, which decreases the DBR mirror reflectivity by shifting the spectral reflectivity plot to longer wavelengths, so that, at the $\lambda = 815$ nm wavelength, the heated structure presents a lower reflectivity to the incident

82
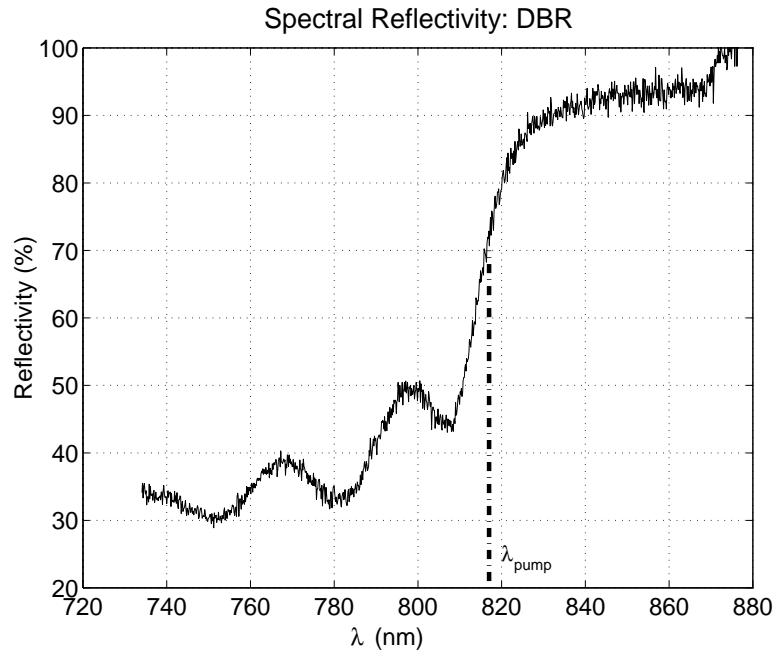
Figure 61. Spectral Reflectivity Curve for DBR Mirror Pump-Probe Measurements
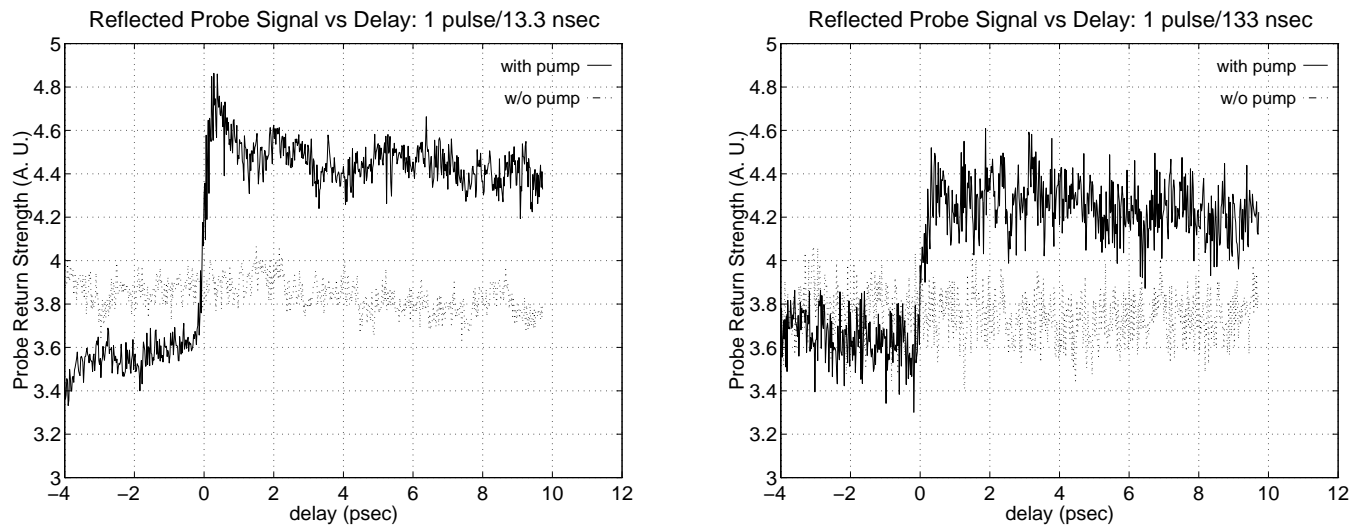
Figure 62. Reflected Probe Signal Response of DBR for Varying Pulse Input Frequency
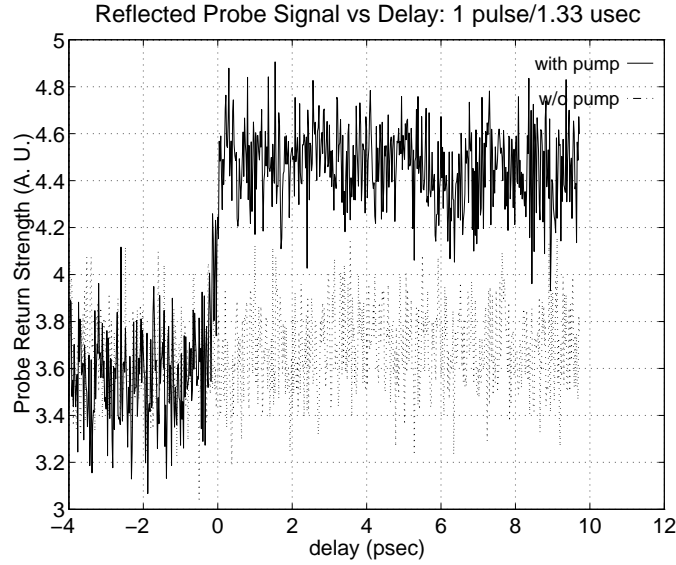
Figure 63. Reflected Probe Signal Response of DBR for Varying Pulse Input Frequency (cont)

probe pulse. As heating is reduced by the increase in time between pulses, the spectral reflectivity curve blue shifts to its unheated reflectivity curve value. The pulse selector was used to generate these plots, which indicate that for pulse separations of 1.33 μsec, the thermal component is nearly indiscernible (see figure 63).

Fits to the DBR response indicate the carrier heating response is not as pronounced as for the VCSEL. Although the 1.1 psec carrier heating relaxation is present in the plot for the DBR (see figure 64 below), it is much weaker than in the VCSEL. The coefficient a_1 (from equation 20) corresponding to the strength of the carrier heating response was smaller ($a_1 = .0029$) for the DBR, while the VCSEL had $a_1 = .0069$. The weaker response may be due to the fewer number of layers in the mirror, or that the GaAs layers in the mirror produce less carrier heating. The pump wavelength is above the band-gap for these layers, and can produce both cooling and heating dynamics, which counteract. The speed of the DBR switch-up is 300 fsec.

4.4.3 Effect of Spectral Location of λ_{pump}. The plots below (see figures 65 and figure 66) indicate the dependence of the reflected signal response on the spectral location of the pump. The series of plots was collected for the DBR mirror, whose GaAs mirror layers have a gap energy below

84
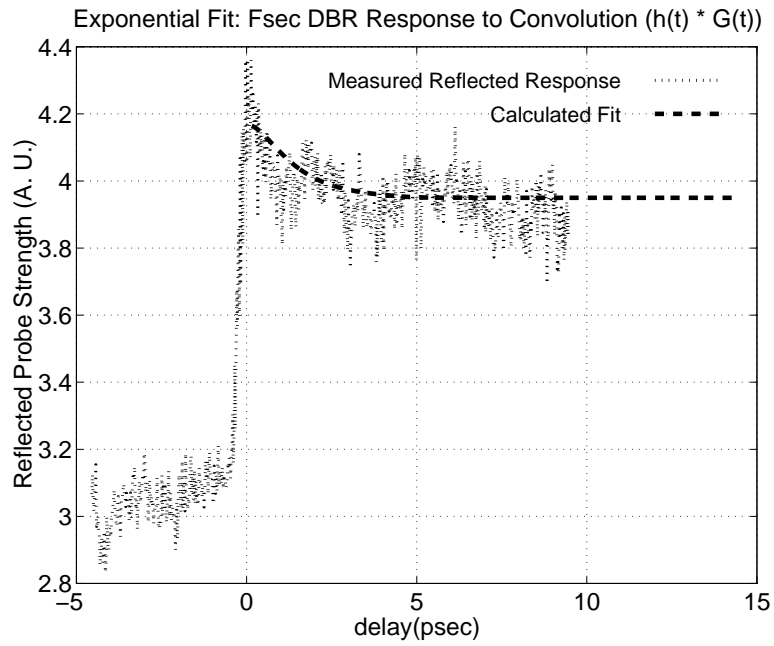
Figure 64. Exponential Fit for DBR Reflected Probe Response ($\tau_{ch} = 1.1$ psec)
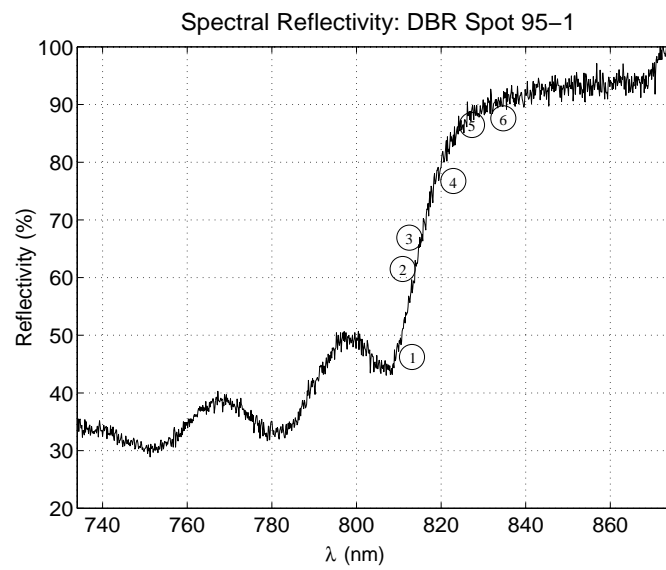
Figure 65. Reflectivity Spectrum of DBR, Noting Data Collection Points for Figure 66

Reflected Probe Strength vs Delay, DBR, Varying Wavelengths
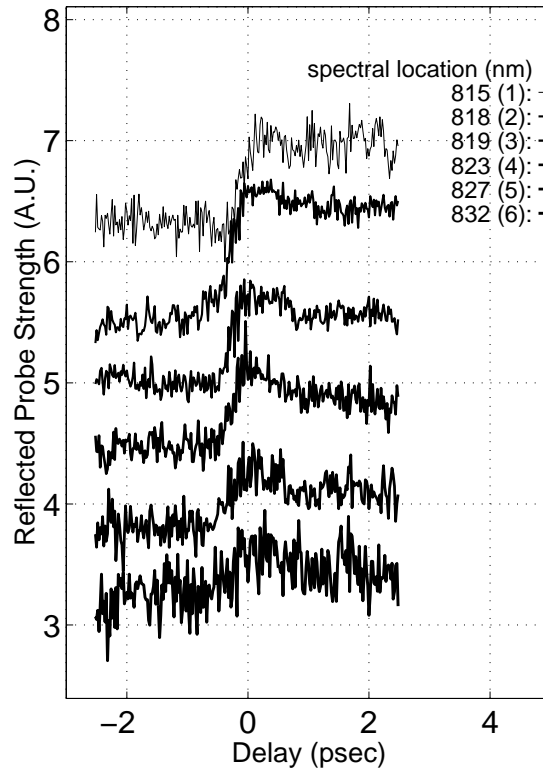
Figure 66.   Reflected Probe Signal as Pump Wavelength is Tuned through the DBR Stop Band Edge

that of the pump. Comparison of these plots with those of the VCSEL indicate the expected negative index shift due to two-photon absorption.

Using the same nonlinear mechanisms but locating the pump near the sidelobe adjacent to the stop band provides the capability of selecting the reflectivity shift up or down. The spectral reflectivity curve at figure 67 provides the spectral locations, and the reflectivity shifts are recorded for these locations in figure 68.

Spectral Reflectivity: DBR Spot 95–2
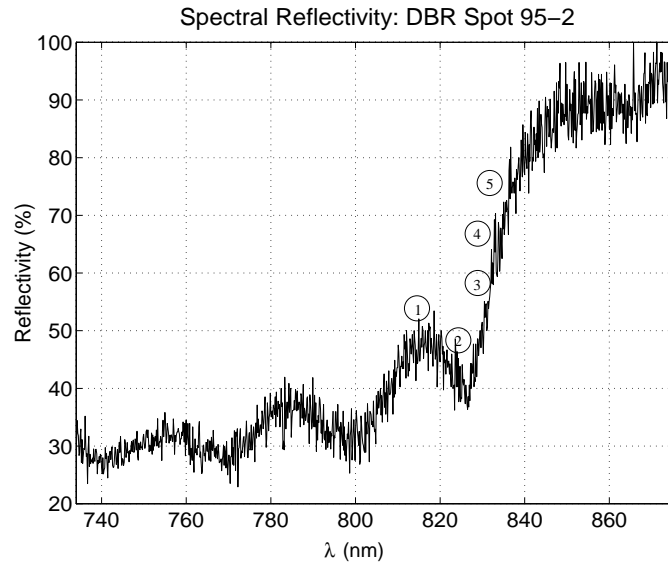
Figure 67. Reflectivity Spectrum of DBR, Noting Data Collection Points for Figure 68

Reflected Probe Strength vs Delay, DBR, Varying Wavelengths
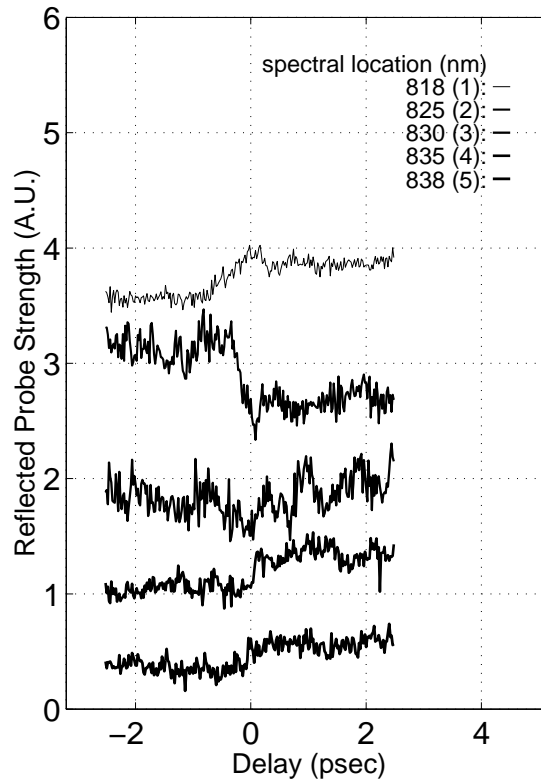
Figure 68. Reflected Probe Signal as Pump Wavelength is Tuned through the Side Lobe

4.4.4 Intensity Dependence. The effect of decreasing the pump intensity is examined in the series of plots shown in figure 69. The decreasing of the pump intensity results in a reduction in the reflectivity change in the probe signal. These plots were collected from the DBR mirror, and indicate average powers as small as 5 mW effected a reflectivity change. This average power corresponds to ~ 1.1 mW/μm^2
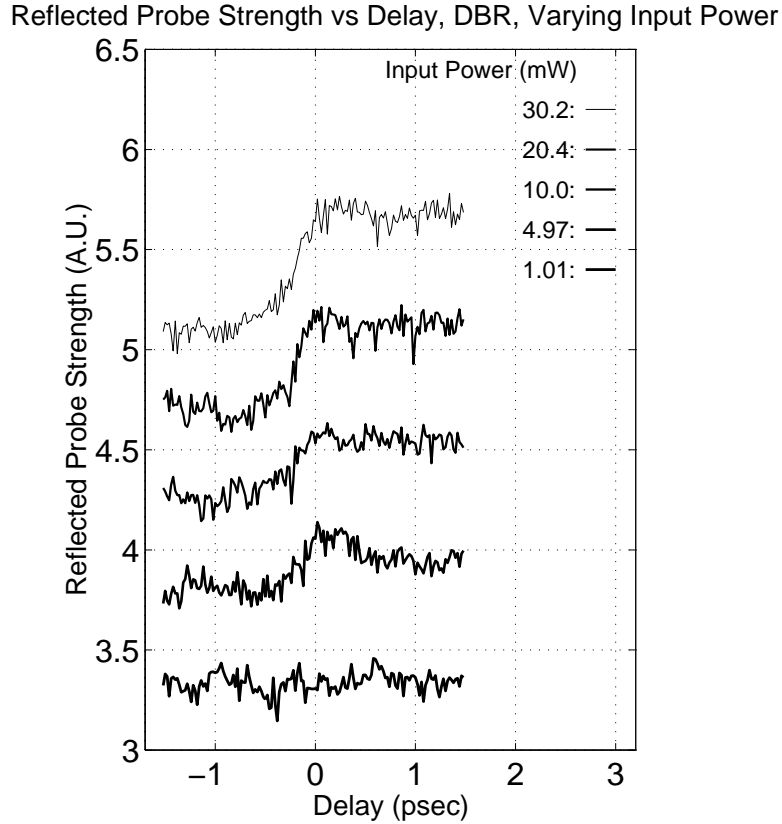
Figure 69. Reflected Signal vs Delay for Decreasing Pump Powers DBR, $\lambda = 818$ nm

4.5 Summary

The use of the carrier generated effects to produce a reflectivity switch in DBRs and VCSELs was demonstrated in this section. The mechanisms affecting the changing reflectivity of the DBR mirrors were able to produce both positive and negative index changes, with related shifts in the spectral reflectivity. Responses to the incident pump indicated reflectivity could be switched on a

sub-picosecond time-scale via two-photon absorption, and that carrier heating effects could be used to effect a reflectivity switch down on a 1.1 psec exponential response curve. The reflectivity changes achieved contrast ratios of 3:1, which is equivalent to that achieved by *Acklin* working at the long wavelength stop band edge [1].

V. Green's Function Solution to Thermally-Driven Bistability in DBR/VCSELs

5.1 Introduction

The experimental data indicates a nonuniform heat distribution in the VCSEL/DBR produces the bistable reflectivity in the multi-layer stacks which constitute its mirrors. To describe the nonuniform heat distribution, and its effect on the mirror reflectivity/VCSEL output, we must model the heat distribution in the stack due to the incident laser. This model assumes the energy absorbed by the mirrors/cavity of the structure is primarily converted to heat, which drives the bistable response. Other losses, such as the loss of energy due to the VCSEL lasing, are assumed to be negligible compared to the thermal response. The heating of a multi-layer stack by a normally incident laser beam (see figure 70) is described by the linear heat conduction equation, in two spatial (longitudinal and radial) dimensions:

$$\frac{1}{r}\frac{\partial}{\partial r}\left(r\frac{\partial T(r,z,t)}{\partial r}\right) + \frac{\partial^2 T(r,z,t)}{\partial z^2} + \frac{1}{\alpha}\frac{\partial T(r,z,t)}{\partial t} = -\frac{g(r,z,t)}{\kappa} \tag{22}$$

where:
α: thermal diffusivity of the medium
κ: thermal conductivity of the medium
$g(r,z,t)$:   power per unit volume generated in the medium by the laser
$T(r,z,t)$:   position- and time-dependent temperature

This equation assumes that the thermal and optical properties of the stack are temperature independent, and the layers are laterally homogeneous and isotropic. Temperature independence, however, is not true for the structures to be studied here. The effect to be observed (change in reflectivity) relies on the temperature dependence of the optical properties of the materials in the stack. For small temperature changes, however, an iterative solution has proven effective in simulating the temperature dependence of the material properties of laser heated multi-layer stacks [29, 28, 30, 46, 35, 45].
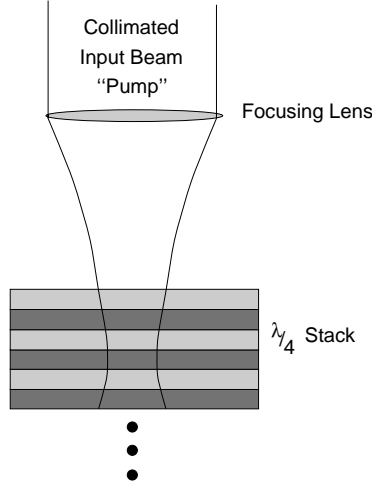
Figure 70. Focused Pump Input, Normally Incident on DBR Mirror Surface

5.2   Algorithm Overview

The method used to calculate the VCSEL/DBR response is depicted in the flowchart at figure 71. Included in this method is the allowance for temperature dependent parameters: $n(T)$: the refractive index, $k(T)$: the extinction coefficient, $\alpha(T)$: the thermal diffusivity, and $\kappa(T)$: the thermal conductivity. $T(r, z, t)$ is used to calculate the change in refractive index for each layer, using dn/dT data for the constituent materials. The algorithm iterates until a stable temperature profile is reached for a given input intensity. In this manner, it is a steady state solution. This index profile is used as the starting index profile as intensity ramps. At each intensity, reflectivity is determined via the matrix methods described in chapter II. By collecting these reflectivities (output intensities) vs the input intensity, the model mimics the input/output relationship employed in the lab.

5.3   Green's Function Solution to the Heat Equation

To solve equation 22, we follow a method developed by McGahan and Cole [34]: a solution for each region (layer) in the multi-layer stack is used, and boundary conditions (continuity of the temperature and the normal component of the heat flux across the layer boundaries) provide the means to solve their interdependence. A Green's function solution $(G_0(r, z, t | r', z', \tau))$ to equation 22 is

91
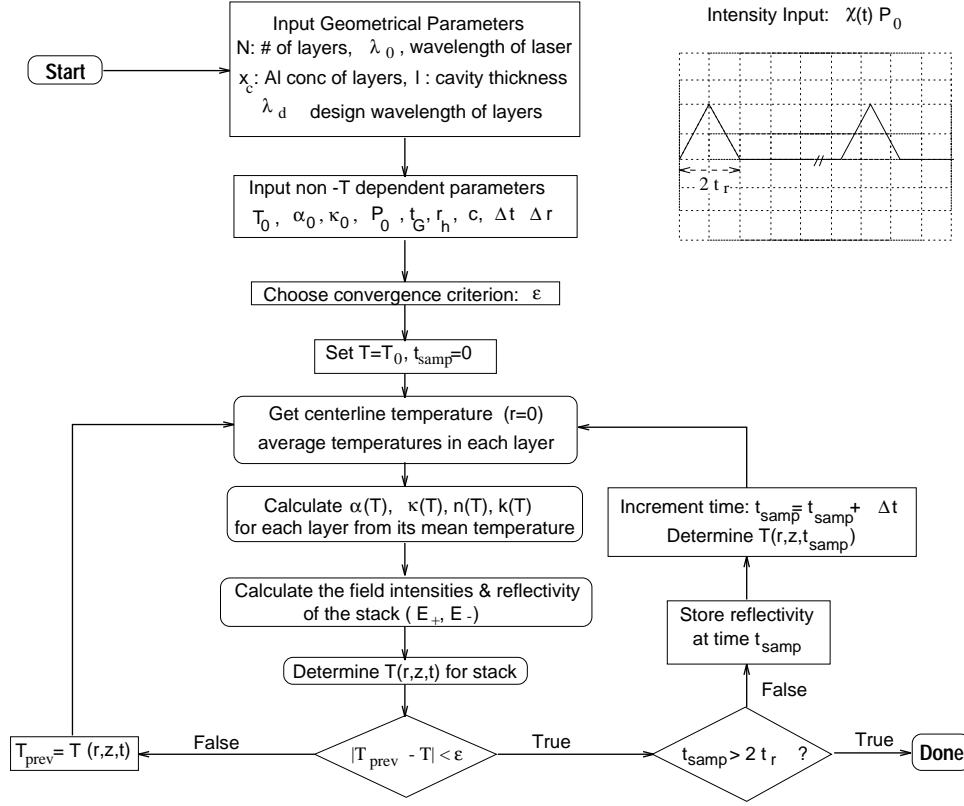
Figure 71.   Algorithm to Obtain Temperature-Dependent Reflectivity Induced by Laser Heating of VCSEL

contained in the superposition of radial/axial solutions of Beck *et al* [5]) to the heat equation [1]. The solution differs for the substrate and for the layers of the multi-layer stack (because the substrate is approximated as semi-infinite). Each layer has its own local coordinate system, so that z runs from 0 to d in each layer, and from 0 to ∞ in the substrate (see figure 72). For the semi-infinite substrate, with $\partial G_0 / \partial z = 0$ at $z = 0$ (so that G_0 is continuous at the boundary) [5]

$$G_0(r, z, t | r', z', \tau) = \frac{1}{4\pi^{3/2}} \frac{1}{\sqrt{\alpha(t - \tau)}} \left\{ \exp\left[-\frac{(z - z')^2}{4\alpha(t - \tau)} \right] + \exp\left[-\frac{(z + z')^2}{4\alpha(t - \tau)} \right] \right\}$$
$$\int_0^\infty \exp\left[-\beta^2 \alpha(t - \tau) \right] \beta \, J_0(\beta r) \, J_0(\beta r') \, d\beta \qquad (23)$$

---

[1] In *Beck*: equations $X20$ (Appendix X) and $R00$ (pg 238) for substrate, and $X22.3$ (Appendix X) and $R00$ (pg 238) for layers
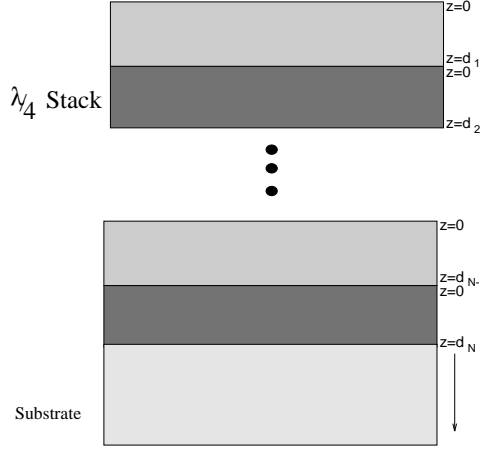
Figure 72. Stack Geometry for Identification of Layer Coordinates

... for $t > \tau$, and zero otherwise. For the layers,

$$G_0(r, z, t|r', z', \tau) = \frac{1}{2\pi d}\left[1 + 2\sum_{m=1}^{\infty} \cos\left(\frac{m\pi z}{d}\right)\cos\left(\frac{m\pi z'}{d}\right)\exp\left(-\frac{m^2\pi^2\alpha(t-\tau)}{d^2}\right)\right]$$

$$\times \int_0^\infty \exp\left[-\beta^2\alpha(t-\tau)\right]\beta\, J_0(\beta r)J_0(\beta r')\, d\beta \qquad (24)$$

... again, for $t > \tau$, and zero otherwise. $J_0(x)$ is the zeroth order Bessel function. Using these Green's functions, McGahan and Cole outlined an equation to arrive at the temperature at any point in the stack at any time [34]:

$$\begin{aligned} T(r, z, t) &= \frac{\alpha}{\kappa}\int_S\int_{\tau=-\infty}^{t} q(r', \tau)G_0(r, z, t|r', z'=z_s, \tau)\, 2\pi r'\, dr'\, d\tau \\ &+ \frac{\alpha}{\kappa}\int_V\int_{\tau=-\infty}^{t} g(r', z', \tau)G_0(r, z, t|r', z', \tau)\, 2\pi r'\, dr'\, dz'\, d\tau \end{aligned} \qquad (25)$$

The first double integral on the right hand side of equation 25 provides the change in temperature due to heat conduction (between layers). The integral over S is for the surface of the region in which the point (r, z) resides and $q(r', \tau)$ is the normal component of the heat flux through the boundary.

The second double integral determines the heat at any point (r, z) which results from sources inside the region (the laser, as well as thermal diffusion from other points in the region). These sources are represented by $g(r, z, t)$ in the volume integral.

93

McGahan and Cole [34] solved these equations for a time-periodic heat source (a sinusoidally modulated laser intensity). In this case we desire a more complex time dependent intensity. A simple input waveform to demonstrate the bistable behavior is the triangle wave (see figure 73). The use of a duty cycle (20 %) allows heat to diffuse and the temperature profile of the multi-layer stack to relax to a steady state between intensity ramps. This more complicated waveform requires some
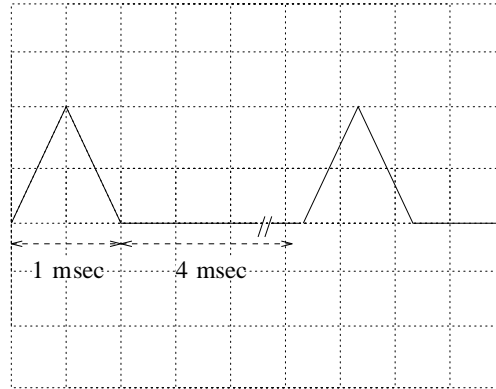
Figure 73. Input Laser Intensity Time Dependence

modification to the approach used by McGahan and Cole. Their algorithm used the Fourier and Hankel Transforms to eliminate difficulties associated with the Bessel functions (inside $G_0(r, z, t)$) in the integral. The solution is more easily handled in transformed space; so this approach maintains the Fourier/Hankel transforms, and collects the necessary temporal frequencies to inverse Fourier transform the solution. The Hankel transform will be used to translate the spatial frequencies back to real space. This method has been used to describe heating in magneto-optical disks, modifying McGahan and Cole's algorithm to model the heat distribution in a spinning disk [42]. Unlike that application, in this VCSEL problem the stack is not moving as the laser heats it; so in that respect this problem is slightly simpler. The addition of an absorbing substrate along with iteratively solving for the temperature dependent thermal and optical properties, however, add unique features to this problem.

5.3.1   Fourier & Hankel Transforms.   We use the Fourier transform relations (see Gaskill [14]):

$$
\begin{aligned}
\mathcal{F}\left\{f(t)\right\} &= F(f) = \int_{-\infty}^{\infty} f(t)\, e^{-j\,2\pi f t} dt \\
\mathcal{F}^{-1}\left\{F(f)\right\} &= f(t) = \int_{-\infty}^{\infty} F(f)\, e^{j\,2\pi f t} df
\end{aligned} \tag{26}
$$

The Hankel transform is used for the Gaussian distribution of the intensity, because it is radially symmetric. The Hankel transform takes the form [13]:

$$
\begin{aligned}
\mathcal{H}\left\{f(r)\right\} &= F(\beta) = \int_{0}^{\infty} f(r)\, r\, J_0(\beta r) dr \\
\mathcal{H}^{-1}\left\{F(\beta)\right\} &= f(r) = \int_{0}^{\infty} F(\beta)\, \beta\, J_0(\beta r) d\beta
\end{aligned} \tag{27}
$$

5.3.2   The Hankel-Transformed Heat Equation Solution $\tilde{T}(\beta, z, f)$.   The Hankel transform of equation 25 is desired.

$$
\begin{aligned}
\tilde{T}(\beta, z, t) &= \mathcal{H}\left\{T(r, z, t)\right\} \\
&= \int_{0}^{\infty} T(r, z, t))\, r\, J_0(\beta r) dr
\end{aligned} \tag{28}
$$

We are helped by the form of $G_0(r, z, t | r', z', \tau)$ in that, for both the layers and the substrate the integral:

$$
G_0(r, z, t | r', z', \tau) = \mathbb{K} \int_{0}^{\infty} \exp\left[-\beta^2 \alpha (t - \tau)\right] \beta\, J_0(\beta r)\, J_0(\beta r')\, d\beta \tag{29}
$$

... is part of the equation (equations 23 & 24). Here the non-r dependent part of each Green's function (labeled $\mathbb{K}$) has been taken outside the transform integral. The form of equation 29 is, by inspection and comparison with equation 27, an inverse Hankel transform. Applying the forward Hankel transform we obtain:

$$
\begin{aligned}
\mathcal{H}\left\{G_0(r, z, t | r', z', \tau)\right\} &= \tilde{G}_0(\beta, z, t | r', z', \tau) \\
&= \mathbb{K} \exp\left[-\beta^2 \alpha (t - \tau)\right] J_0(\beta r')
\end{aligned} \tag{30}
$$

95

This relation can be applied to each of the Green's functions with the result:

$$
\begin{aligned}
\tilde{T}(\beta, z, t) \;=\; & \frac{\alpha}{\kappa} \int_{\tau=-\infty}^{t} \mathbb{K} \exp\left[-\beta^2 \alpha(t-\tau)\right] 2\pi \int_{S} q(r', \tau) J_0(\beta r')\, r'\, dr'\, d\tau \\
& + \frac{\alpha}{\kappa} \int_{\tau=-\infty}^{t} \int_{z'} \mathbb{K} \exp\left[-\beta^2 \alpha(t-\tau)\right] 2\pi \int_{r'} g(r', z', \tau) J_0(\beta r')\, r'\, dr'\, dz'\, d\tau \quad (31)
\end{aligned}
$$

Here, the z', τ dependence of $\mathbb{K}$ require that it be kept under the integrals over z' and τ. The integrals over r' in this equation are, again, Hankel transforms, producing the transformed functions $\tilde{q}(\beta, \tau)$ and $\tilde{g}(\beta, z', \tau)$. The Hankel transformed temperature equation results:

$$
\tilde{T}(\beta, z, t) = \frac{\alpha}{\kappa} \int_{-\infty}^{t} 2\pi\, \mathbb{K} e^{\left[-\beta^2 \alpha(t-\tau)\right]} \tilde{q}(\beta, \tau)\, d\tau \;+\; \frac{\alpha}{\kappa} \int_{-\infty}^{t} \int_{z'} 2\pi\, \mathbb{K} e^{\left[-\beta^2 \alpha(t-\tau)\right]} \tilde{g}(\beta, z', \tau)\, dz'\, d\tau \quad (32)
$$

Having used the factor $J_0(\beta r')$ in the Hankel transforms for $\tilde{q}$ and $\tilde{g}$, we let:

$$
\begin{aligned}
\tilde{G}^{ssi}(\beta, z, t | z', \tau) \;=\; & 2\pi\, \mathbb{K} e^{\left[-\beta^2 \alpha(t-\tau)\right]} \\
\;=\; & \frac{1}{2\sqrt{\pi}} \frac{1}{\sqrt{\alpha(t-\tau)}} \left\{ e^{\left[-\frac{(z-z')^2}{4\alpha(t-\tau)}\right]} + e^{\left[-\frac{(z+z')^2}{4\alpha(t-\tau)}\right]} \right\} e^{\left[-\beta^2 \alpha(t-\tau)\right]} \quad (33)
\end{aligned}
$$

... and for the layers:

$$
\begin{aligned}
\tilde{G}^{l}(\beta, z, t | z', \tau) \;=\; & 2\pi \mathbb{K} e^{\left[-\beta^2 \alpha(t-\tau)\right]} \\
\;=\; & \frac{1}{d} \left[1 + 2 \sum_{m=1}^{\infty} \cos\left(\frac{m\pi z}{d}\right) \cos\left(\frac{m\pi z'}{d}\right) e^{\left(-\frac{m^2 \pi^2 \alpha(t-\tau)}{d^2}\right)} \right] e^{\left[-\beta^2 \alpha(t-\tau)\right]} \quad (34)
\end{aligned}
$$

Fourier transforming equation 32 further reduces the integrations:

$$
\begin{aligned}
\mathcal{F}\left\{\tilde{T}(\beta, z, t)\right\} \;=\; & \tilde{T}(\beta, z, f) \\
\;=\; & \mathcal{F}\left\{ \frac{\alpha}{\kappa} \int_{\tau} \tilde{G}(\beta, z, t | z' = z_s, \tau) \tilde{q}(\beta, \tau)\, d\tau + \frac{\alpha}{\kappa} \int_{\tau} \int_{z'} \tilde{G}(\beta, z, t | z', \tau) \tilde{g}(\beta, z', f)\, dz'\, d\tau \right\} \\
\tilde{T}(\beta, z, f) \;=\; & \frac{\alpha}{\kappa} \tilde{G}(\beta, z, f | z' = z_s) \tilde{q}(\beta, f) + \underbrace{\frac{\alpha}{\kappa} \int_{z'} \tilde{G}(\beta, z, f | z') \tilde{g}(\beta, z', f)\, dz'}_{B(\beta, z, f)} \quad (35)
\end{aligned}
$$

The component $B(\beta, z, f)$ represents the volumetric heat integral. Equation 35 is to be applied in each layer. Continuity of the heat flux and temperature at the interfaces will yield $\tilde{q}(\beta, f)$ and, finally, $\tilde{T}$. The calculation of the real-time temperature profile is obtained by calculating $\tilde{T}(\beta, z, f)$ for a collection of temporal and spatial frequencies, then performing inverse Hankel and Fourier transforms to get $T(r, z, t)$.

The transforms of each part of equation 35 are involved. For this reason, the transforms of the Green's functions, the development of the volume heat expressions, and their transforms, is deferred to Appendix A. A summary of their results is contained in the next section.

5.4 Multi-layer Solution

With the transforms derived in Appendix A, the method can now be applied to a multi-layer stack by following McGahan and Cole's solution for the N-layer problem, and substituting in the revised equations from Appendix A.

5.4.1 Step 1: Expressions for Temperature Profile in Transformed Space.

The N-layer stack is divided into $N + 2$ regions: Region 0 is the air above the stack, Region 1, the first layer, ..., and Region $N + 1$, the substrate. The general expression for the temperature in each region is:

$$
\begin{aligned}
&\text{Air:} \\
\tilde{T}_0\left(\beta, z, f\right) \;\; &= \tfrac{\alpha_0}{\kappa_0} \tilde{q}_{10}(\beta, f)\tilde{G}_0^{si}(\beta, z, f | z' = 0) \\
&\text{for layer } j: \\
\tilde{T}_j\left(\beta, z, f\right) \;\; &= \tfrac{\alpha_j}{\kappa_j} \tilde{q}_{j-1,j}(\beta, f)\tilde{G}_j^l(\beta, z, f | z' = 0) + \tfrac{\alpha_j}{\kappa_j} \tilde{q}_{j,j+1}(\beta, f)\tilde{G}_j^l(\beta, z, f | z' = d) + B_j(\beta, z, f) \\
&\text{substrate:} \\
\tilde{T}_{N+1}\left(\beta, z, f\right) \;\; &= \tfrac{\alpha_{N+1}}{\kappa_{N+1}} \tilde{q}_{N,N+1}(\beta, f)\tilde{G}_{N+1}^{si}(\beta, z, f | z' = 0) + B_{N+1}(\beta, z, f)
\end{aligned}
$$

A summary of the equations to be used in each layer (finite or semi-infinite) and for each case are provided below (derivations are contained in appendix A). The three cases are: $\beta = 0$ and $f = 0$, $\beta = 0$ only, and $\beta \neq 0$, $f \neq 0$. The parameters in the following equations are recapped in the table that follows Case 3.

5.4.1.1 Case 1: $\beta = 0$ and $f = 0$.   We collect expressions for G, g, and B, for semi-infinite (air & substrate) and finite (layers) media:

$$\tilde{G}^{si}(0,z,0|z') = \frac{1}{\sqrt{\pi\alpha}} \left[e^{-\frac{b_-^2}{t_G}}\sqrt{t_G} - (\sqrt{\pi}b_-)\mathrm{erfc}\left(\frac{b_-}{\sqrt{t_G}}\right) + \{b_+ \to b_-\} \right] \tag{36}$$

$$\tilde{G}^{l}(0,z,0|z') = \frac{1}{d}\left[t_G + 2\sum_{m=1}^{\infty}\cos\left(\frac{m\pi z}{d}\right)\cos\left(\frac{m\pi z'}{d}\right)\frac{1 - e^{-(\alpha\pi^2 m^2/d^2)t_G}}{\alpha\pi^2 m^2/d^2} \right] \tag{37}$$

$$\tilde{g}(0,z,0) = P_0\Gamma(0)\frac{2nk}{\lambda_0}\left[C_1 e^{-2\gamma z} + C_2 e^{2\gamma z} + C_3\cos\left(\delta d - 2\delta z + \phi\right) \right] \tag{38}$$

$$B^{si}(0,z,0) = \frac{P_0\Gamma(0)nk}{\kappa\lambda_0}\frac{1}{2\gamma^2}|E_+(z=0)|^2\left[e^{4\gamma^2\alpha t_G}\mathrm{erfc}\left(2\gamma\sqrt{\alpha t_G}\right) - 1 + \frac{4\gamma\sqrt{\alpha t_G}}{\sqrt{\pi}} \right] \tag{39}$$

$$B^{l}(0,z,0) = \frac{\alpha P_0\Gamma(f=0)}{\kappa d}\frac{2nk}{\lambda_0}\left[\mathbb{C}_1 t_G + 2\sum_{m=1}^{\infty}\mathbb{C}_m\cos\left(m\pi z/d\right)\frac{1 - e^{-(\alpha\pi^2 m^2/d^2)t_G}}{\alpha\pi^2 m^2/d^2} \right] \tag{40}$$

5.4.1.2 Case 2: $\beta = 0$ only.

$$\tilde{G}^{si}(0,z,f|z') = \frac{1}{4a\sqrt{\alpha}}\left\{ e^{-2ab_-}\left[1 + \mathrm{erf}\left(a\sqrt{t_G} - \frac{b_-}{\sqrt{t_G}}\right) \right] \right.$$
$$\left. -e^{2ab_-}\mathrm{erfc}\left(a\sqrt{t_G} + \frac{b_-}{\sqrt{t_G}}\right) + \{b_- \to b_+\} \right\} \tag{41}$$

$$\tilde{G}^{l}(0,z,f|z') = \frac{1}{d}\left[t_G e^{-j\pi f t_G}\mathrm{sinc}(\pi f t_G) \right.$$
$$\left. +2\sum_{m=1}^{\infty}\cos\left(\frac{m\pi z}{d}\right)\cos\left(\frac{m\pi z'}{d}\right)\frac{1 - e^{-(j2\pi f + \frac{\alpha\pi^2 m^2}{d^2})t_G}}{j2\pi f + \frac{\alpha\pi^2 m^2}{d^2}} \right] \tag{42}$$

$$\tilde{g}(0,z,f) = P_0\Gamma(f)\frac{2nk}{\lambda_0}\left[C_1 e^{-2\gamma z} + C_2 e^{2\gamma z} + C_3\cos\left(\delta d - 2\delta z + \phi\right) \right] \tag{43}$$

$$B^{si}(0,z,f) = \frac{\alpha P_0\Gamma(0)}{\kappa a}\frac{2nk}{\lambda_0}|E_+(z=0)|^2 e^{-\beta^2 r_h^2/4}\frac{1}{4\gamma^2\alpha - a^2}$$
$$\times\left[2\gamma\sqrt{\alpha}\left(\mathrm{erf}(a\sqrt{t_G}) + e^{t_G(4\gamma^2\alpha - a^2)}\mathrm{erfc}(2\gamma\sqrt{t_G\alpha})\right) - a \right] \tag{44}$$

$$B^{l}(0,z,f) = \frac{\alpha P_0\Gamma(f)}{\kappa d}\frac{2nk}{\lambda_0}\left[\mathbb{C}_1 t_G e^{-j\pi f t_G}\mathrm{sinc}(\pi f t_G) \right.$$
$$\left. +2\sum_{m=1}^{\infty}\mathbb{C}_m\cos\left(\frac{m\pi z}{d}\right)\frac{1 - e^{-(j2\pi f + \frac{\alpha\pi^2 m^2}{d^2})t_G}}{j2\pi f + \frac{\alpha\pi^2 m^2}{d^2}} \right] \tag{45}$$

5.4.1.3 Case 3: $\beta \neq 0$, $f \neq 0$.

$$\tilde{G}^{si}(\beta, z, f | z') = \frac{1}{4a\sqrt{\alpha}} \left\{ e^{-2ab_-} \left[1 + \mathrm{erf}\left(a\sqrt{t_G} - \frac{b_-}{\sqrt{t_G}} \right) \right] \right.$$
$$\left. - e^{2ab_-}\mathrm{erfc}\left(a\sqrt{t_G} + \frac{b_-}{\sqrt{t_G}} \right) + \{ b_- \rightarrow b_+ \} \right\} \tag{46}$$

$$\tilde{G}^l(\beta, z, f | z') = \frac{1}{d} \left[\frac{1 - e^{-a^2 t_G}}{a^2} + 2 \sum_{m=1}^{\infty} \cos\left(\frac{m\pi z}{d} \right) \cos\left(\frac{m\pi z'}{d} \right) \frac{1 - e^{-(a^2 + \alpha\pi^2 m^2/d^2)t_G}}{a^2 + \alpha\pi^2 m^2/d^2} \right] \tag{47}$$

$$\tilde{g}(\beta, z, f) = P_0 \Gamma(f) \frac{2nk}{\lambda_0} e^{-\beta^2 r_h^2/4} \left[C_1 e^{-2\gamma z} + C_2 e^{2\gamma z} + C_3 \cos\left(\delta d - 2\delta z + \phi \right) \right] \tag{48}$$

$$B^{si}(\beta, z, f) = \frac{\alpha P_0 \Gamma(f)}{\kappa a} \frac{2nk}{\lambda_0} |E_+(z=0)|^2 e^{-\beta^2 r_h^2/4} \frac{1}{4\gamma^2\alpha - a^2}$$
$$\times \left[2\gamma\sqrt{\alpha} \left(\mathrm{erf}(a\sqrt{t_G}) + e^{t_G(4\gamma^2\alpha - a^2)}\mathrm{erfc}(2\gamma\sqrt{t_G\alpha}) \right) - a \right] \tag{49}$$

$$B^l(\beta, z, f) = \frac{\alpha P_0 \Gamma(f) e^{-\beta^2 r_h^2/4}}{\kappa d} \frac{2nk}{\lambda_0} \left[\mathbb{C}_1 \frac{1 - e^{-a^2 t_G}}{a^2} \right.$$
$$\left. + 2 \sum_{m=1}^{\infty} \mathbb{C}_m \cos\left(m\pi z/d \right) \frac{1 - e^{-(a^2 + \frac{\alpha\pi^2 m^2}{d^2})t_G}}{a^2 + \frac{\alpha\pi^2 m^2}{d^2}} \right] \tag{50}$$

. . . with:

$$\mathbb{C}_1 = \frac{C_1}{2\gamma} \left[1 - e^{-2\gamma d} \right] + \frac{C_2}{2\gamma} \left[e^{2\gamma d} - 1 \right] + \frac{C_3}{\delta} \sin\left(\delta d \right) \cos\left(\phi \right)$$

$$\mathbb{C}_m = \frac{2\gamma}{4\gamma^2 + m^2\pi^2/d^2} \left\{ C_1 \left[1 - (-1)^m e^{-2\gamma d} \right] + C_2 \left[(-1)^m e^{2\gamma d} - 1 \right] \right\}$$
$$+ C_3 \left(\frac{4\delta}{4\delta^2 - m^2\pi^2/d^2} \right) \times \left\{ \begin{array}{ll} \sin\left(\delta d \right) \cos\left(\phi \right) & m = \text{even} \\ \cos\left(\delta d \right) \sin\left(\phi \right) & m = \text{odd} \end{array} \right\} \tag{51}$$

The parameters for these equations have been collected in Table 3 below.

Table 3. Parameters for Equations

α_x	thermal diffusivity of region x	$b_\pm$	$\frac{|z - z'|}{2\sqrt{\alpha}}$
t_G	Gate time (time at which Green's function is truncated)	$\mathrm{erfc}()$	complimentary error function $(1 - erf(x))$
P_0	Mean input intensity (W/cm^2)	$\Gamma(f)$	Fourier transform of the intensity input waveform (called $\chi(t)$ in this text)

99

Table 3. Parameters for Equations (cont)

n	index of refraction in the medium	k	extinction coefficient in the medium
r_h	Gaussian radius of the input intensity (cm)	λ_0	free space wavelength of laser input
γ	$\frac{2\pi n}{\lambda_0}$	δ	$\frac{2\pi k}{\lambda_0}$
E_+	forward propagating wave	E_-	reverse propagating wave
C_1	$|E_+(z=0)|^2$	C_2	$|E_-(z=d)|^2 e^{-2\gamma d}$
C_3	$|E_+(z=0)E_-^*(z=d)|e^{-\gamma d}$	ϕ	$arg\left[E_+(z=0)E_-^*(z=d)\right]$
κ	thermal conductivity of the medium	$\mathbb{C}_{1,2}$	defined in eqn 51
a	$\sqrt{\beta^2\alpha + j2\pi f}$		

5.4.2 Step 2: Enforce Continuity of Temperature Over Interfaces. This step involves constructing a series of equations relating the temperature on one side of the interface to the other. For the arguments to the Green's functions ($\tilde{G}(\beta, z, f)$ and the volume heat term ($B(\beta, z, f)$), we drop the β and f terms, to make the equations concise; these equations still apply to all three cases above:

$$\frac{\alpha_0}{\kappa_0}\tilde{G}_0^{si}(0|0)\tilde{q}_{1,0} = \tilde{G}_1^l(0|0)\tilde{q}_{0,1} + \frac{\alpha_1}{\kappa_1}\tilde{G}_1^{si}(0|0)\tilde{q}_{2,1} + B_1(0) \tag{52}$$

at intermediate interfaces:

$$\frac{\alpha_j}{\kappa_j}\tilde{G}_j^l(d_j|0)\tilde{q}_{j-1,j} + \frac{\alpha_j}{\kappa_j}\tilde{G}_j^l(d_j|d_j)\tilde{q}_{j,j+1} + B_j(d_j) =$$
$$\frac{\alpha_{j+1}}{\kappa_{j+1}}\tilde{G}_{j+1}^l(0|0)\tilde{q}_{j,j+1} + \frac{\alpha_{j+1}}{\kappa_{j+1}}\tilde{G}_{j+1}^l(0|d_{j+1})\tilde{q}_{j+2,j+1} + B_{j+1}(0) \tag{53}$$

and, at the last interface:

$$\frac{\alpha_N}{\kappa_N}\tilde{G}_N^l(d_N|0)\tilde{q}_{N-1,N} + \frac{\alpha_N}{\kappa_N}\tilde{G}_N^l(d_N|d_N)\tilde{q}_{N+1,N} + B_N(d_N) =$$
$$\frac{\alpha_{N+1}}{\kappa_{N+1}}\tilde{G}_{N+1}^l(0|0)\tilde{q}_{N,N+1} + B_{N+1}(0) \tag{54}$$

Continuity of heat fluxes across the boundary require that $\tilde{q}_{i,j} = -\tilde{q}_{j,i}$. This condition, and the equations above, produce a set of $N+1$ simultaneous equations for the $N+1$ heat fluxes $\tilde{q}$. As in both McGahan and Cole [34] and Shih [42] the equations may be written in a tridiagonal matrix

100

form:

$$
\begin{bmatrix}
W_0 + U_1 & -V_1 & 0 & \dots & 0 \\
-V_1 & U_1 + U_2 & V_2 & \dots & 0 \\
0 & -V_2 & U_2 + U_3 & \dots & 0 \\
\vdots & \vdots & \vdots & \ddots & V_N \\
0 & 0 & 0 & -V_N & U_N + W_{N+1}
\end{bmatrix}
\times
\begin{bmatrix}
\tilde{q}_{1,0} \\
\tilde{q}_{2,1} \\
\tilde{q}_{3,2} \\
\vdots \\
\tilde{q}_{N+1,N}
\end{bmatrix}
=
\begin{bmatrix}
B_1(0) \\
B_2(0) - B_1(d_1) \\
B_3(0) - B_2(d_2) \vdots \\
B_{N+1}(0) - B_N(d_N)
\end{bmatrix}
$$

(55)

$\dots$, and U, V, and W are, as in Shih's paper:

$$
\begin{aligned}
U_j &= \frac{\alpha_j}{\kappa_j}\tilde{G}^l_j(0|0) = \frac{\alpha_j}{\kappa_j}\tilde{G}^l_j(d_j|d_j) \\
V_j &= \frac{\alpha_j}{\kappa_j}\tilde{G}^l_j(0|d_j) = \frac{\alpha_j}{\kappa_j}\tilde{G}^l_j(d_j|0) \\
W_j &= \frac{\alpha_j}{\kappa_j}\tilde{G}^{si}_j(0|0)
\end{aligned}
$$

Defining the Green's functions at the interfaces:

$$
\tilde{G}^{si}(0|0) =
\begin{cases}
\frac{1}{a\sqrt{\alpha}}\mathrm{erf}(a\sqrt{t_G}): & a \neq 0 \\
2\sqrt{\frac{t_G}{\alpha\pi}}: & a = 0
\end{cases}
$$

(56)

$$
\tilde{G}^l(0|0) = \tilde{G}^l(d|d) = \frac{1}{d} \times
\begin{cases}
\left[t_G + 2\sum_{m=1}^{\infty} \frac{1-e^{-(\alpha\pi^2 m^2/d^2)t_G}}{\alpha\pi^2 m^2/d^2} \right]: & \beta = 0, f = 0 \\
\left[t_G e^{-j\pi f t_G}\mathrm{sinc}(\pi f t_G) + 2\sum_{m=1}^{\infty} \frac{1-e^{-(j2\pi f + \alpha\pi^2 m^2/d^2)t_G}}{j2\pi f + \alpha\pi^2 m^2/d^2} \right]: & \beta = 0 \text{ only} \\
\left[\frac{1-e^{-a^2 t_G}}{a^2} + 2\sum_{m=1}^{\infty} \frac{1-e^{-(a^2+\alpha\pi^2 m^2/d^2)t_G}}{a^2+\alpha\pi^2 m^2/d^2} \right]: & \beta \neq 0, f \neq 0
\end{cases}
$$

(57)

$$
\tilde{G}^l(0|d) = \tilde{G}^l(d|0) = \frac{1}{d} \times
\begin{cases}
\left[t_G + 2\sum_{m=1}^{\infty}(-1)^m \frac{1-e^{-(\frac{\alpha\pi^2 m^2}{d^2})t_G}}{\alpha\pi^2 m^2/d^2} \right]: & \beta = 0, f = 0 \\
\left[t_G e^{-j\pi f t_G}\mathrm{sinc}(\pi f t_G) + 2\sum_{m=1}^{\infty}(-1)^m \frac{1-e^{-(j2\pi f + \frac{\alpha\pi^2 m^2}{d^2})t_G}}{j2\pi f + \alpha\pi^2 m^2/d^2} \right]: & \beta = 0 \\
\left[\frac{1-e^{-a^2 t_G}}{a^2} + 2\sum_{m=1}^{\infty}(-1)^m \frac{1-e^{-(a^2+\frac{\alpha\pi^2 m^2}{d^2})t_G}}{a^2+\alpha\pi^2 m^2/d^2} \right]: & \beta \neq 0, f \neq 0
\end{cases}
$$

(58)

5.4.3   Step 3: Solve for the Heat Fluxes $\tilde{q}$.   Equation 55 has the form $\mathbb{W} \times \mathbb{Q} = \mathbb{B}$, with $\mathbb{W}$ in tridiagonal form. By inverting $\mathbb{W}$, we may solve for $\mathbb{Q}$, the heat fluxes for the stack. These heat fluxes, then, are the final input necessary to solving for $T(\beta, z, f)$.

5.4.4   Step 4: Solve for the Transformed Temperature $T(\beta, z, f)$, and Invert.   The heat fluxes $\tilde{q}_{ij}$ and the volume heat $B(\beta, z, f)$ can now be used to determine the transformed temperature $T(\beta, z, f)$ anywhere in the stack, by use of the temperature equations outlined in step 1. Hankel and Fourier inverse transforms of $T(\beta, z, f)$, produce the real-space, real-time temperature distribution in the stack.

5.5   Algorithm Development

The flowchart for the main program is contained in figure 71. Once the non-temperature dependent parameters are entered, the program begins a loop. One full cycle of this loop includes an update of the temperature dependent parameters for each layer of the stack. These parameters are then used to determine the new heat profile.

No direct measurements on the VCSEL laser-induced heat profile could be accomplished, so the algorithm was run against O. W. Shih's [42] example magneto-optic disk structure and found to agree with his calculation of the temperature profile. This agreement, the replication of VCSEL/DBR reflectivity bistability, and the validation of the cavity temperature the model predicts by the VCSEL wavelength shift all indicate the algorithm is sound.

5.5.1   Temperature Dependent Parameters.   These include the refractive index, n, the extinction coefficient, k, the thermal conductivity, κ, and the thermal diffusivity, α.

5.5.1.1   n, k.   The most recent data available for the temperature dependence of the index of refraction in GaAs comes from ellipsometry studies at Arizona State University [32]. The index of refraction and extinction coefficient are both tabulated from room temperature to $\sim 600C$. The energy range for the data covers the 800-900 nm range necessary for our purposes. No data yet exists for the ternary $Al_x Ga_{1-x}As$ for $n(T)$ and $k(T)$. For the dn/dT of AlGaAs layers, we use

102

a formula developed by Dudley [11], and described in chapter II, valid for wavelengths below the band gap, which develops dn/dT from an oscillator model. For k, fortunately, the wavelengths of interest in this study correspond to energies well below the band gap of the AlGaAs layers even at high temperatures. As a result, k is neglected for AlGaAs layers.

5.5.1.2 κ, α.   The calculation of the thermal conductivity for $Al_xGa_{1-x}As$ used here follows the rationale of Adachi [2]. He used experimental data and fit the curve using a cubic fit with the x concentration as the parameter. Adachi's formulae provide thermal conductivity (κ), density (ρ), and specific heat (C_p), from which we can get diffusivity ($\alpha = \frac{\kappa}{\rho C_p}$). Temperature dependent thermal conductivity is taken from Brice ("Properties of Gallium Arsenide") [6] for GaAs only. The formula is:

$$\kappa(T) = \frac{A}{T^{1.2}} \tag{59}$$

... with A being adjustable, based on the purity of the sample. To fit the room temperature κ to Adachi, A from Brice was adjusted to fit Brice and Adachi over the expected temperature range, within 10 %. To fit this temperature dependence to Adachi's formula, would require A to be 414 ($\frac{W\ K^{0.2}}{cm}$). In a similar manner, the temperature dependence of the thermal diffusivity ($\alpha(T)$) in GaAs can be estimated by comparing the relations according to Adachi to those estimates for $\alpha(T)$ for GaAs from Brice, this produces:

$$\alpha(T) = .4974 - 8.4 \times 10^{-4}T. \tag{60}$$

No temperature dependence is now incorporated into the algorithm for $x \neq 0$. Incorporating x concentration requires a parametric fit to experimental data for several temperature values of the conductivity/diffusivity. No experimental data exists for the x concentrations of interest.

5.6   Summary

The aim of this chapter was to introduce the algorithm used to determine the expected temperature distribution in the VCSEL/DBR stack. The results of this program have been useful in describing the bistable reactions of these structures.

As with most mathematical models of dynamic systems, initially the intent was to get as close as possible to describing the physical effects of all changing parameters. Early in the development it was evident the thermal dependencies were not extensively explored enough to cover all temperature dependencies. A pleasing result was the estimates for $Al_xGa_{1-x}As$ refractive index $n(T)$. The Single Effective Oscillator model worked extremely well in determining the temperature dispersion of the refractive index for $Al_xGa_{1-x}As$, as can be seen in figure 12. Although lack of experimental data prevented estimates for κ and α, their temperature dependence is probably on the order of the equivalent GaAs relationship with temperature. If so, their temperature dependence would not appreciably change the heat distributions, especially at the lower temperatures for bistability seen in the VCSELs (50 to 100^oC).

The exclusion of lasing in the model was a difficult choice. The laser dynamics proved too complex to adequately model the temperature effects, the carrier densities, and their effects, and the photon fluxes of the pump and VCSEL.

The strengths of this approach, though, were evident early on. No other model offered the ability to model the radial and axial heating, and incorporate time dependence simultaneously. With fair accuracy, the VCSEL cavity temperature, reflectivity bistability, and wavelength dependence of the hysteresis was predicted, and the self focusing described. With modifications for Joule heating at each layer, electrically pumped VCSEL heating could be described in this manner.

VI. **Conclusion**

In the previous five chapters, the effects of the nonlinear optical response of distributed Bragg reflector based devices has provided a means to switch reflectivity in response to an optical stimulus. The various mechanisms employed to force the DBR/VCSELs to switch include the thermal response, which effected a positive refractive index change on a μsec time scale; carrier heating, which produced a positive Δn shift and responded on a psec time scale; and carrier density changes and the optical Stark effect, which provided a means to blue shift (-Δn) the index and acted on the femtosecond scale.

In demonstrating bistable behavior using the thermal nonlinearity, this work is the first of its kind. The application of the thermal nonlinear mechanism produced a bistable reflectivity response in the DBR and bistability in VCSEL power, wavelength, and divergence. By mathematically modeling this response, the thermal nonlinear mechanism was shown to be sufficient to effect the bistable reflectivity. Additionally, this model verified the radial heat profile's effect in self-focusing the VCSEL and pump beams inside the mirror layers and cavity. The bistable wavelength shift of the VCSELs indicates the temperature ranges predicted by the mathematical model are within those seen experimentally, partially verifying the model's accuracy.

The carrier generated nonlinearities demonstrated in chapter IV indicate a capability for switching speeds approaching the sub-picosecond regime. The experimental measurements of the refractive index response agree with those nonlinear index measurements for below-band excitation of AlGaAs samples [20]. Although carrier generated effects have been used to effect a bistable switch in DBRs [1] no means of effecting switching in both -up and -down directions has been reported. The index nonlinearities which produce these effects are now published, but the application of the index nonlinearities to the switching dynamics is new.

6.1 Devices

Practical devices may soon be achievable using the reflectivity response of AlGaAs DBR structures. The carrier generated nonlinearity demonstrated in chapter IV is more likely to produce

a useful switching capability than the thermally-generated bistable devices of chapter III. Switching speeds and power consumption are the main criteria which rate an optical switch's prospects. The thermally-driven switch is too slow and power-hungry to place high on this scale.

If carrier generated mechanisms are pursued, femtosecond switch-up is achievable, but the switch-down will require the slower psec response of the carrier heating mechanism. There is some ability to tailor the psec response. The injection of carriers into the bands can increase the carrier density, and when the optical stimulus interacts with the layers, free carrier absorption will provide additional excited carriers. This process enhances carrier heating as phonon relaxation occurs. Although the time constant for the carrier heating is not affected, the strength of the index change is enhanced. The combination of these two switching schemes, which can be affected with a single pump laser, could produce a bit width near 1 picosecond.

By tailoring the x-concentrations and layer thicknesses of the DBR, it is possible to select the location of the stop band edge. The fast switch evident in these structures could be useful in optical device protection. For a sensitive detector array, for example, such a DBR, placed in the optical path, could be used to limit damage to the array by switching to low reflectivity when it encounters an intense "blinding" input. Femtosecond response in the mirror is advantageous, if the relaxation from carrier heating can be managed.

As far as using these nonlinearities to affect VCSEL output, pulsed experimentation and modeling of the VCSEL has quantified optical delays and pulse spreading in the pulsed VCSEL output [23]. An optical delay is of course to be expected, as the dispersion in the layers of the mirror causes the broadening of the input pulse, and traversing the multi-layers delays its interaction with the gain region. The delay is also partially the result of the build up of the population inversion, finite recombination time of the carriers, photon build-up in the cavity, and optical delay in the pulse exiting the multi-layered mirrors. For pulsed excitation, the fastest response achieved has been a 20 psec delay, with a pulse spread of 4 ps. Given this limitation on the VCSEL output, it is apparent optically switching the device may be limited to speeds > 20 psec, rather than the femtosecond response for the mirrors seen here.

Experimentally, the construction of more optimal DBR/VCSEL structures would benefit this data tremendously. Many of the samples used were less than ideal for the experiment. Stop band edges generally had a gradual slope, so that the dramatic reflectivity shift expected was tough to achieve. Isolation of the below-band excited nonlinear effects on the DBR mirror alone would be an interesting project. Although excitation at the long wavelength edge of the stop band of the DBR was attempted, the stop band there was, as above, not sharp enough to make an effective switch.

The use of free carrier absorption to tailor the carrier heating effect could also prove useful. In Hultgren's pump-probe experimentation [20], he found electrically injected carriers could enhance carrier heating. He attributed this response to an increased capacity for free carrier absorption (the electrically injected carriers were absorbing pump photons); the excited free carriers, upon phonon relaxation, produced more carrier heating. By enhancing carrier heating, the magnitude of the reflectivity shift in the mirrors can be increased. Electrically-pumped VCSELs are available at AFIT to examine the effect on the switch-down in reflectivity. The current configuration for photo-pumping would allow top-mirror-emitting devices to be simultaneously optically probed as carriers were injected. The expected ability to control the switch-down strength of the mirror could effect a high speed clocking signal.

Extension of this mathematical model to mimic Joule heating in electrically pumped VSCELs would be very useful in examining the interdependencies of the VCSEL components. The heat generator used here was volumetric; occurring throughout the mirror layers as the fields penetrated the structure. In the electrically stimulated VCSEL, the abrupt changes in mirror layers provides, especially in the p-doped layers, a resistive heating that is more adequately modeled as a surface heat source at each layer. Of course, with diffusion and field calculations already incorporated here, the primary work lies in describing the heat source adequately, as we did for the laser heating. This type of tool could prove extremely useful to the device designer.

Although several attempts were made to capture the VCSEL pulsed output at the autocorrelator, none were successful. The femtosecond response of the VCSEL would be a useful measurement in

determining the speed limitations of the photo-pumped devices. Indications (power available from the VCSEL, and min pulse power detectable from the TiS) are that the system should be able to capture a VCSEL pulsed response. Further efforts should be made to collect this data.

Appendix A. **Fourier Transforms and Volumetric Heat Integral**

This appendix outlines the derivation of several functions supporting the solution of the Fourier transformed heat equation (equation 35).

A.1   *Truncated Green's Functions*

As described in chapter V, McGahan and Cole's method provides a relatively simple solution to the heating problem for a sinusoidal laser intensity. The application to more complex input intensity waveforms would be straightforward, except that the solution cannot be applied for low spatial and temporal frequencies. For example, the Hankel and Fourier transform for the substrate Green's function solution in McGahan and Cole's problem was [34:equation 7a]:

$$\tilde{G}^{si}(\beta, z, f | z') = \frac{1}{2\alpha\eta} \left(e^{-|z-z'|\eta} + e^{-|z+z'|\eta} \right)$$

with:
$\tilde{G}^{si}$:   transformed Green's function for the semi-infinite *si* layer (i.e. substrate)
α: thermal diffusivity
η: $\sqrt{\beta^2 + 2\pi j f / \alpha}$

The difficulty noted by Shih [42] is that as $\beta \to 0$ and $f \to 0$, $\tilde{G}^{si}$ becomes undefined. It is important to retain the low frequency components as they significantly affect the resultant inverse transform. To retain these components, Shih truncated the Green's function after a gate time t_G. This method alleviates two problems at once. First, it bounds the zero frequency component of $\tilde{G}$. The other difficulty it prevents is in the application of the Fast Fourier Transform (FFT). The FFT inherently truncates the function to which it is applied. For infinite duration signals, this time-aliases the outlying parts of the function into the non-truncated section. By truncating the Green's function, we force the outlying tails of the function to zero, eliminating their aliased contribution. The choice of t_G is important to the accuracy of the model; it must be chosen so that it is greater than the largest time of interest. For the triangle-wave input intensity (fig 73), we must exceed the duration of the triangle, but not exceed the wait to the next triangle input.

Shih used Fourier transforms for both the spatial and temporal dimensions in his method. This was necessary because the spinning of the multi-layer stack eliminated the radial symmetry of the problem. In this problem the radial symmetry is maintained, so that we can eliminate one of the spatial dimensions by using the Hankel transform.

A.1.1   Semi-Infinite Layer (Substrate) $\tilde{G}^{si}(\beta, z', f)$.   The Fourier Transform of the Green's function for the semi-infinite substrate is:

$$
\mathcal{F}\left\{G^{si}\right\} = \tilde{G}^{si}
$$
$$
= \int_{-\infty}^{\infty} \frac{1}{2\sqrt{\pi}} \frac{1}{\sqrt{\alpha(t-\tau)}} \left\{ e^{\left[-\frac{(z-z')^2}{4\alpha(t-\tau)}\right]} + e^{\left[-\frac{(z+z')^2}{4\alpha(t-\tau)}\right]} \right\} e^{-\left[\beta^2\alpha(t-\tau)\right]} e^{-j2\pi f(t-\tau)} d(t-\tau) \quad (61)
$$

To evaluate eqn 61, we replace $(t - \tau)$ with γ and eliminate the values of the interval for which the Green's function vanishes $(t - \tau < 0)$ and $(t - \tau > t_G)$, leaving:

$$
\tilde{G}^{si} = \int_0^{t_G} \frac{1}{2\sqrt{\pi\alpha\gamma}} e^{-\beta^2\alpha\gamma} \left\{ e^{\left[-\frac{(z-z')^2}{4\alpha\gamma}\right]} + e^{\left[-\frac{(z+z')^2}{4\alpha\gamma}\right]} \right\} e^{-j2\pi f\gamma} d\gamma
$$

$$
= \int_0^{t_G} \frac{1}{2\sqrt{\pi\alpha\gamma}} e^{-(\beta^2\alpha+j2\pi f)\gamma - \frac{(z-z')^2}{4\alpha\gamma}} d\gamma + \int_0^{t_G} \frac{1}{2\sqrt{\pi\alpha\gamma}} e^{-(\beta^2\alpha+j2\pi f)\gamma - \frac{(z+z')^2}{4\alpha\gamma}} d\gamma \quad (62)
$$

$$
= \int_0^{t_G} \frac{1}{2\sqrt{\pi\alpha\gamma}} e^{-a^2\gamma - \frac{b_-^2}{\gamma}} d\gamma + \int_0^{t_G} \frac{1}{2\sqrt{\pi\alpha\gamma}} e^{-a^2\gamma - \frac{b_+^2}{\gamma}} d\gamma \quad (63)
$$

With $a = \sqrt{\beta^2\alpha + j2\pi f}$, and $b_\pm = \frac{|z \pm z'|}{2\sqrt{\alpha}}$.

We now evaluate two cases of interest:

A.1.1.1   Case 1: $\beta = 0$ and $f = 0$.   In this case $a = 0$; we will deal first with the integral containing b_-. Reduced for $a = 0$:

$$
\tilde{G}^{si}_{b_-}\left(\beta = 0, z, f = 0 | z'\right) = \int_0^{t_G} \frac{1}{2\sqrt{\pi\alpha\gamma}} e^{-\frac{b_-^2}{\gamma}} d\gamma \quad (64)
$$

A change of variable to $x^2 = \frac{1}{\gamma}$, followed by integration by parts yields:

$$
\tilde{G}^{si}_{b_-} = \int_0^{t_G} \frac{1}{2\sqrt{\pi\alpha\gamma}} e^{-\frac{b_-^2}{\gamma}} d\gamma
$$

$$\tilde{G}^{\prime si}_{b_-} = \frac{1}{2\sqrt{\pi\alpha}}\int_{\frac{1}{\sqrt{t_G}}}^{\infty}\frac{2}{x^2}e^{-b_-^2 x^2}dx$$

integrating by parts:

$$= \frac{1}{\sqrt{\pi\alpha}}\left[e^{-\frac{b_-^2}{t_G}}\sqrt{t_G}-(2b_-^2)\int_{\frac{1}{\sqrt{t_G}}}^{\infty}e^{-b_-^2 x^2}dx\right]$$

using a change of variables ($y = b_- x$) on the remaining integral:

$$= \frac{1}{\sqrt{\pi\alpha}}\left[e^{-\frac{b_-^2}{t_G}}\sqrt{t_G}-(2b_-)\int_{\frac{b_-}{\sqrt{t_G}}}^{\infty}e^{-y^2}dy\right]$$

$$= \frac{1}{\sqrt{\pi\alpha}}\left[e^{-\frac{b_-^2}{t_G}}\sqrt{t_G}-(\sqrt{\pi}b_-)\mathrm{erfc}\left(\frac{b_-}{\sqrt{t_G}}\right)\right] \tag{65}$$

The result is similar for the integral using $b_+ = \frac{|z+z'|}{2\sqrt{\alpha}}$, so we can take eqn 65, substitute in b_+ for b_- and add to get the transformed Green's function:

$$\tilde{G}^{\prime si}(\beta=0,z,f=0|z') = \frac{1}{\sqrt{\pi\alpha}}\left[e^{-\frac{b_-^2}{t_G}}\sqrt{t_G}-(\sqrt{\pi}b_-)\mathrm{erfc}\left(\frac{b_-}{\sqrt{t_G}}\right)+\{b_+\to b_-\}\right] \tag{66}$$

A.1.1.2 Case 2: $a\neq 0$ (i.e. $\beta\neq 0$ and/or $f\neq 0$).   Again, we will treat the integral containing the $z-z'$ term in eqn 62 (called here $\mathbb{F}_1$), then substitute $z+z'$ to get the second integral. As in eqn 63 we replace $a = \sqrt{\beta^2\alpha+j2\pi f}$, and use $b_- = \frac{|z-z'|}{2\sqrt{\alpha}}$. The result provides:

$$\mathbb{F}_1 = \int_0^{t_G}\frac{1}{2\sqrt{\pi\alpha\gamma}}e^{-a^2\gamma-\frac{b_-^2}{\gamma}}d\gamma$$

... with the variable change $\mu^2 = \gamma$:

$$\mathbb{F}_1 = \int_0^{\sqrt{t_G}}\frac{1}{\sqrt{\pi\alpha}}e^{-a^2\mu^2-\frac{b_-^2}{\mu^2}}d\mu$$

$$= \frac{1}{\sqrt{\pi\alpha}}\int_0^{\sqrt{t_G}}e^{-a^2\mu^2-\frac{b_-^2}{\mu^2}}d\mu$$

now using the integral formula (eqn 1.3.3.20 vol 1, Prudnikov [40])

$$\int_0^x e^{-a^2 x^2-\frac{b^2}{x^2}}dx = \frac{\sqrt{\pi}}{4a}\left\{e^{2ab}\left[\mathrm{erf}\left(ax+\frac{b}{x}\right)-1\right]+e^{-2ab}\left[\mathrm{erf}\left(ax-\frac{b}{x}\right)+1\right]\right\}$$

inserting $b = b_-$ and $x = \sqrt{t_G}$ provides the integral solution

111

$$\mathbb{F}_1 = \frac{1}{\sqrt{\pi\alpha}}\frac{\sqrt{\pi}}{4a}\left\{e^{2ab_-}\underbrace{\left[\operatorname{erf}\left(a\sqrt{t_G}+\frac{b_-}{\sqrt{t_G}}\right)-1\right]}+e^{-2ab_-}\left[\operatorname{erf}\left(a\sqrt{t_G}-\frac{b_-}{\sqrt{t_G}}\right)+1\right]\right\} \qquad (67)$$

Returning to equation 62 we have the integral containing b_-; to obtain the answer for b_+ we need only substitute $\{b_- \to b_+\}$ into eqn 67 and add, so that:

$$\tilde{G}^{si}(\beta, z, f|z') =$$
$$\frac{1}{4a\sqrt{\alpha}}\left\{e^{-2ab_-}\left[1+\operatorname{erf}\left(a\sqrt{t_G}-\frac{b_-}{\sqrt{t_G}}\right)\right]-e^{2ab_-}\operatorname{erfc}\left(a\sqrt{t_G}+\frac{b_-}{\sqrt{t_G}}\right)+\{b_- \to b_+\}\right\} \quad (68)$$

For $\beta \neq 0$ and/or $f \neq 0$. Note that as the gate time t_G tends toward infinity, $\operatorname{erf}(x) \to 1$, and $\operatorname{erfc}(x) \to 0$, producing:

$$\tilde{G}^{si}(\beta, z, f|z') = \frac{1}{2a\sqrt{\alpha}}\left\{e^{-2ab_-} + e^{-2ab_-}\right\}$$

This is equivalent to McGahan and Cole's solution [34:equation 7a] for the non-truncated Green's function in the substrate.

A.1.2 Finite Layers $\tilde{G}^l(\beta, z', f)$. Working on the Hankel-transformed Green's function for the layers in eqn 34, the Fourier transform takes the form:

$$\mathcal{F}\left\{\tilde{G}^l\right\} = \tilde{G}^l$$
$$= \int_{-\infty}^{\infty}\frac{1}{d}\left[1+2\sum_{m=1}^{\infty}\cos\left(\frac{m\pi z}{d}\right)\cos\left(\frac{m\pi z'}{d}\right)\exp\left(-\frac{\alpha\pi^2 m^2(t-\tau)}{d^2}\right)\right]$$
$$\times\, e^{\left[-\beta^2\alpha(t-\tau)\right]}e^{-j\,2\pi f(t-\tau)}d(t-\tau) \qquad (69)$$

Proceeding as for the substrate case, we evaluate $\tilde{G}^{\prime l}$, replacing $(t-\tau)$ with γ; eliminate the values of the interval for which the Green's function vanishes $(t-\tau < 0)$ and $(t-\tau > t_G)$, and

112

break the integral into parts, leaving:

$$\tilde{G}^l = \frac{1}{d} \int_0^{t_G} e^{-(\beta^2 \alpha + j 2\pi f)\gamma} d\gamma + 2 \sum_{m=1}^{\infty} \cos\left(\frac{m\pi z}{d}\right) \cos\left(\frac{m\pi z'}{d}\right)$$

$$\times \int_0^{t_G} e^{-(\beta^2 \alpha + j 2\pi f)\gamma} e^{\left(-\frac{\alpha \pi^2 m^2 \gamma}{d^2}\right)} d\gamma$$

$$\tilde{G}^l = \frac{1}{d} \int_0^{t_G} e^{-a^2 \gamma} d\gamma + 2 \sum_{m=1}^{\infty} \cos\left(\frac{m\pi z}{d}\right) \cos\left(\frac{m\pi z'}{d}\right) \int_0^{t_G} e^{-a^2 \gamma} e^{\left(-\frac{\alpha \pi^2 m^2 \gamma}{d^2}\right)} d\gamma \qquad (70)$$

... with $a = \sqrt{\beta^2 \alpha + j 2\pi f}$.

A.1.2.1   Case 1: $\beta = 0$ and $f = 0$.   In this case $a = 0$; the integrals are much more easily accomplished than for the substrate case, they produce:

$$\tilde{G}^l(\beta = 0, z, f = 0|z') = \frac{1}{d}\left[t_G + 2\sum_{m=1}^{\infty} \cos\left(\frac{m\pi z}{d}\right) \cos\left(\frac{m\pi z'}{d}\right) \frac{1 - e^{-(\alpha \pi^2 m^2/d^2)t_G}}{\alpha \pi^2 m^2/d^2}\right] \qquad (71)$$

A.1.2.2   Case 2: $\beta = 0$ but $f \neq 0$.   In this case $a^2 = j 2\pi f$ the integrals are still fairly easy, so they won't be expanded here:

$$\tilde{G}^l(\beta = 0, z, f|z') =$$
$$\frac{1}{d}\left[t_G e^{-j\pi f t_G} \operatorname{sinc}(\pi f t_G) + 2\sum_{m=1}^{\infty} \cos\left(\frac{m\pi z}{d}\right) \cos\left(\frac{m\pi z'}{d}\right) \frac{1 - e^{-(j 2\pi f + \alpha \pi^2 m^2/d^2)t_G}}{j 2\pi f + \alpha \pi^2 m^2/d^2}\right] \qquad (72)$$

with $\operatorname{sinc}(x) = \frac{\sin(x)}{x}$.

A.1.2.3   Case 3: $\beta \neq 0$ and $f \neq 0$.

$$\tilde{G}^l(\beta, z, f|z') = \frac{1}{d}\left[\frac{1 - e^{-a^2 t_G}}{a^2} + 2\sum_{m=1}^{\infty} \cos\left(\frac{m\pi z}{d}\right) \cos\left(\frac{m\pi z'}{d}\right) \frac{1 - e^{-(a^2 + \alpha \pi^2 m^2/d^2)t_G}}{a^2 + \alpha \pi^2 m^2/d^2}\right] \qquad (73)$$

113

A.2 Volume Heat

To determine the power absorbed by the multi-layer stack, we follow Jackson [21]. For time harmonic fields, the conservation of energy in the volume V is (Jackson eqn 6.134):

$$\Re \left\{ \underbrace{\frac{1}{2} \int_V (\mathbf{J}^* \cdot \mathbf{E}) d^3 x}_{\text{energy input}} + \underbrace{2i\omega \int_V \frac{1}{16\pi} (\mathbf{E} \cdot \mathbf{D}^* - \mathbf{B} \cdot \mathbf{H}^*) d^3 x}_{\text{energy absorbed}} + \underbrace{\int \mathbf{S} \cdot \hat{n} \, da}_{\text{energy flowing out}} \right\} = 0 \qquad (74)$$

... where $\mathbf{E}$ and $\mathbf{H}$ are the electric and magnetic field vectors and $\mathbf{D}$ and $\mathbf{B}$ are the electric and magnetic flux vectors, ω is the radial frequency of the incident laser; and $\Re$ indicates that the real part of the expression is to be evaluated. So, the energy absorbed per unit volume is:

$$\Re \left\{ \frac{i\omega}{8\pi} (\mathbf{E} \cdot \mathbf{D}^* - \mathbf{B} \cdot \mathbf{H}^*) \right\} = \frac{1}{4\pi} \Re \left\{ \frac{i\omega}{2} (\mathbf{E} \cdot \mathbf{D}^* - \mathbf{B} \cdot \mathbf{H}^*) \right\} \qquad \text{[Gaussian]}$$

$$= \underbrace{\Re \left\{ \frac{i\omega}{2} (\mathbf{E} \cdot \mathbf{D}^* - \mathbf{B} \cdot \mathbf{H}^*) \right\}}_{-\nabla \cdot \langle S \rangle} \qquad \text{[MKS]} \qquad (75)$$

So that the heat source term for a time-dependent intensity inputs is described by:

$$g(r, z, t) = P_0 \chi(t) (-\nabla \cdot \langle S \rangle) \qquad (76)$$

where:

$(-\nabla \cdot \langle S \rangle)$: normalized power absorption in each layer

$\langle S \rangle$: time averaged Poynting Vector

P_0: Mean incident intensity (W/cm^2)

$\chi(t)$: waveform of the time dependent incident intensity (triangle)

A.2.1 Power Absorbed.

To find the divergence of the Poynting vector, we follow Chen [9]. He develops expressions for lossy media for the power absorbed. Chen starts with the negative of the divergence of the Poynting vector ([9] eqn 2.62):

$$-\nabla \cdot \langle S_{med} \rangle = \frac{1}{2} \Re \left\{ i\omega (\mathbf{E} \cdot \mathbf{D}^* - \mathbf{H}^* \cdot \mathbf{B}) \right\} \qquad (77)$$

... where $\langle S_{med} \rangle$ is the time averaged Poynting vector in the medium. For a homogeneous, isotropic medium (can be lossy) (Chen eqns 4.76/7 and 4.83/4 [9]):

$$
\begin{aligned}
\mathbf{D} &= \epsilon_0 \epsilon \mathbf{E} \\
\mathbf{B} &= \mu_0 \mu \mathbf{H}
\end{aligned}
\tag{78}
$$

and the fields may be expressed:

$$
\begin{aligned}
\mathbf{E} &= \mathbf{E}_0\, e^{i\mathbf{k}\cdot\mathbf{r}} = \mathbf{E}_0\, e^{i(\mathbf{k_1}+i\mathbf{k_2})\cdot\mathbf{r}} \\
\mathbf{H} &= \mathbf{H}_0\, e^{i\mathbf{k}\cdot\mathbf{r}} = \mathbf{H}_0\, e^{i(\mathbf{k_1}+i\mathbf{k_2})\cdot\mathbf{r}}
\end{aligned}
\tag{79}
$$

where:

ϵ_0	permittivity (free space)	ϵ	relative permittivity (material)
μ_0	permeability (free space)	μ	relative permeability
k	complex propagation vector	$k_1(k_2)$	real(imaginary) parts of k

Forming the dot products in eqn 77:

$$
\begin{aligned}
\mathbf{E}\cdot\mathbf{D}^* &= \epsilon_0 \epsilon^* |\mathbf{E}_0|^2 e^{-2\mathbf{k_2}\cdot\mathbf{r}} \\
\mathbf{H}^*\cdot\mathbf{B} &= \mu_0 \mu |\mathbf{H}_0|^2 e^{-2\mathbf{k_2}\cdot\mathbf{r}}
\end{aligned}
\tag{80}
$$

For lossy materials, Chen provides the relation:

$$
\begin{aligned}
\mu_0 \mu |\mathbf{H_0}|^2 &= \sqrt{1+\tau^2}\,\epsilon_0 \epsilon |\mathbf{E_0}|^2 \qquad \text{(Chen eqn 4.118)}. \\
&= (1+\tau^2/2)\epsilon_0 \epsilon |\mathbf{E_0}|^2 \qquad \text{for } \tau \ll 1
\end{aligned}
$$

The term τ is called the loss tangent. It is the ratio of the conduction current to the displacement current in the lossy medium: $\tau = \frac{\sigma}{\omega\epsilon_0\epsilon}$ with σ the conductivity of the medium, and ϵ_0, ϵ, and ω as previously defined. Inserting the relations (eqn 80) for the dot products, and substituting in for $\mu_0\mu|\mathbf{H_0}|^2$, as well as $\epsilon = \epsilon_1 - i\epsilon_2$:

$$
\begin{aligned}
-\nabla\cdot\langle S_{med}\rangle &= \frac{1}{2}\Re\left\{ i\omega\left(\epsilon_0(\epsilon_1 - i\epsilon_2)|\mathbf{E_0}|^2 e^{-2\mathbf{k_2}\cdot\mathbf{r}} - \epsilon_0(\epsilon_1 + i\epsilon_2)|\mathbf{E_0}|^2(1+\frac{\tau^2}{2})e^{-2\mathbf{k_2}\cdot\mathbf{r}} \right) \right\} \\
&= \frac{1}{2}\left[\left(2\omega\epsilon_0\epsilon_2|\mathbf{E_0}|^2 + \frac{\tau^2}{2}\omega\epsilon_0\epsilon_2|\mathbf{E_0}|^2 \right)e^{-2\mathbf{k_2}\cdot\mathbf{r}} \right] \\
&\approx \omega\epsilon_2\epsilon_0|\mathbf{E_0}|^2 e^{-2\mathbf{k_2}\cdot\mathbf{r}} \qquad \text{for } \tau \ll 1
\end{aligned}
\tag{81}
$$

115

To determine the normalized power absorption (normalized to a given incident power) we divide by the magnitude of the incident Poynting vector (incident medium (air) is assumed lossless ($k_2 = 0$)):

$$|\langle S_{inc} \rangle| = \frac{k_0 \sqrt{\mu_{inc}\epsilon_{inc}} \left[\frac{1}{2}\left(\sqrt{1+\tau^2}+1\right)\right]^{\frac{1}{2}} e^{-2\mathbf{k_2}\cdot\mathbf{r}} |\mathbf{E_{inc}}|^2}{2\omega\mu_0\mu_{inc}} \quad \text{via Chen eqn 4.122}$$

$$= \frac{k_0|\mathbf{E_{inc}}|^2\sqrt{\epsilon_{inc}}}{2\omega\mu_0} \quad \text{for } \tau << 1 \text{ and } \mu_{inc} = 1 \tag{82}$$

... here $k_0 = 2\pi/\lambda_0$ with λ_0 being the free space wavelength of the incident laser.

Finally, we form the normalized expression for the power absorbed:

$$-\nabla \cdot \langle S \rangle = \frac{-\nabla \cdot \langle S_{med} \rangle}{|\langle S_{inc} \rangle|}$$

$$= \frac{\omega\epsilon_2\epsilon_0\mu_0 2\omega}{k_0\sqrt{\epsilon_{inc}}} \frac{|\mathbf{E_0}|^2}{|\mathbf{E_{inc}}|^2} e^{-2\mathbf{k_2}\cdot\mathbf{r}}$$

$$= \frac{2\epsilon_2\omega/c}{n_{inc}} \frac{|\mathbf{E_0}|^2}{P_0} e^{-2\mathbf{k_2}\cdot\mathbf{r}} \quad \text{with } k_0 = \omega/c, \ P_0 = |\mathbf{E_{inc}}|^2 \text{ and } \sqrt{\epsilon_{inc}} = n_{inc}$$

where:

n_{inc}:   incident medium index of refraction (for this problem air (taking $n_{inc} = 1$))

ϵ_2:   Imaginary part of the dielectric constant for the medium ($Im(\epsilon) = 2nk$)

k: extinction coefficient of the region

n: refractive index of the region

$\mathbf{E(r,z)}$:   electric field vector at the point, $|\mathbf{E(r,z)}|^2 = |\mathbf{E_0}|^2 e^{-2\mathbf{k_2}\cdot\mathbf{r}}$

$\mu_0\epsilon_0 = 1/c^2$:   with c being the speed of light in free space

Inserting $n_{inc} = 1$, $\epsilon_2 = 2nk$, and $k_0 = \omega/c$, we can express the power absorbed at the point (r,z) in the medium,

$$-\nabla \cdot \langle S \rangle = 4k_0 nk \frac{|E(r,z)|^2}{P_0} \tag{83}$$

For a Gaussian input intensity distribution, we can express the field distribution as:

$$\mathbf{E(r,z)} = \frac{1}{\sqrt{2\pi r_h^2}} e^{-r^2/(2r_h^2)} \mathbf{E(z)}$$

116

... so that, in terms of normalized fields ($|E_{norm}(z)|^2 = |\mathbf{E}(\mathbf{z})|^2/P_0$) eqn 83 becomes ($k_0 = 2\pi/\lambda_0$):

$$-\nabla \cdot \langle S \rangle = \frac{8\pi n k}{\lambda_0} \frac{1}{2\pi r_h^2} e^{-r^2/r_h^2} |E_{norm}(z)|^2 \tag{84}$$

A.2.2 Pulse Shape.   In this case we use the triangle waveform described in the previous section. Mathematically, $\chi(t)$ is expressed:

$$
\begin{aligned}
\chi(t) &= \frac{t}{t_r} : \quad 0 \leq t \leq t_r \\
&= 2 - \frac{t}{t_r} : \quad t_r \leq t \leq 2t_r \\
&= 0 : \quad 2t_r \leq t \leq \infty
\end{aligned}
\tag{85}
$$

... with $2t_r$ the duration of the triangle.

A.2.3 Transformed Heat Source ($\tilde{g}(r', z', f)$).   We can now form the heat source term ($g(r, z, t)$) of equation 76. Inserting the expression for $-\nabla \cdot \langle S \rangle$ from eqn 84:

$$g(r, z, t) = P_0 \chi(t) \frac{4nk}{\lambda_0} \frac{1}{r_h^2} e^{-r^2/r_h^2} |E_{norm}(z)|^2 \tag{86}$$

Next we determine $\tilde{g}(\beta, z', f)$ for equation 35. The Fourier transform for $\chi(t)$ yields:

$$\mathcal{F}\{\chi(t)\} = \Gamma(f) = t_r \, e^{-j\,2\pi f t_r} \operatorname{sinc}^2(\pi f t_r) \tag{87}$$

... and again, $\operatorname{sinc}(x) = \frac{\sin(x)}{x}$. This produces the Fourier transform of equation 76:

$$\tilde{g}(r', z', f) = P_0 \Gamma(f) \frac{4nk}{\lambda_0} \frac{1}{r_h^2} e^{-r'^2/r_h^2} |E_{norm}(z')|^2$$

with $\Gamma(f)$ as in eqn 87.

The Hankel transform is next to be determined:

$$
\begin{aligned}
\mathcal{H}(\tilde{g}(r', z', f)) &= \tilde{g}(\beta, z', f) \\
&= \mathcal{H}\left\{P_0\Gamma(f)\frac{4\pi nk}{\lambda_0}\frac{1}{\pi r_h^2}e^{-r'^2/r_h^2}|E_{norm}(z')|^2\right\} \\
&= P_0\Gamma(f)\frac{4\pi nk}{\lambda_0}|E_{norm}(z')|^2\mathcal{H}\left\{\frac{1}{\pi r_h^2}e^{-r'^2/r_h^2}\right\} \\
&= P_0\Gamma(f)\frac{2nk}{\lambda_0}|E_{norm}(z')|^2e^{-\beta^2 r_h^2/4}
\end{aligned}
\tag{88}
$$

A.2.4   Field Calculations.   As with the calculations used in McGahan and Cole [34] we use Crook's method to calculate $E_{norm}(z)$ [10]. The calculation superposes the counter-propagating fields in the stack layers. The normalized field is expressed:

$$
E_{norm}(z) = E_+(z=0)e^{\frac{j2\pi nz}{\lambda_0}}e^{\frac{-2\pi kz}{\lambda_0}} + E_-(z=d)e^{\frac{j2\pi n(d-z)}{\lambda_0}}e^{\frac{-2\pi k(d-z)}{\lambda_0}}
\tag{89}
$$

with n, k, and λ_0 as previously defined, and $E_+(z=0)$ and $E_-(z=d)$ refer to the normalized counter-propagating field amplitudes downward (E_+) into the stack and upward (E_-) reflected from lower layer interfaces. The quantity d is the layer thickness, so that $z = 0$ indicates the top of the layer, and $z = d$ the bottom, with the incident laser entering the top of the stack. Inserting this expression into eqn 90 produces:

$$
\tilde{g}(\beta, z, f) = P_0\Gamma(f)\frac{2nk}{\lambda_0}e^{-\beta^2 r_h^2/4}\left[C_1 e^{-2\gamma z} + C_2 e^{2\gamma z} + C_3 \cos(\delta d - 2\delta z - \phi)\right]
\tag{90}
$$

where:
$C_1 = |E_+(z=0)|^2$ for semi-infinite or layer
$C_2 = |E_-(z=d)|^2 e^{-2\gamma d}$ for layer only
$C_3 = 2|E_+(z=0)E_-^*(z=d)|e^{-\gamma d}$ for layer only
and
$\gamma = 2\pi k/\lambda_0, \delta = 2\pi n/\lambda_0,$ $\phi = arg\left[E_+(z=0)E_-^*(z=d)\right]$

The fields in the stack are determined by a matrix approach as described in chapter II.

A.2.5   Volume Heat Integral: $\tilde{B}(\beta, z', f)$.   The Green's function solution to the temperature distribution in real space and time involved two time integrals, a surface integral and a volumetric integral (see eqn 25). The Hankel/Fourier transformed solution reduces the number of integrations (i. e. computer time) significantly. Repeating eqn 35:

$$\tilde{T}(\beta, z, f) \; = \; \frac{\alpha}{\kappa} \tilde{G}(\beta, z, f | z' = z_s) \tilde{q}(\beta, f) + \underbrace{\frac{\alpha}{\kappa} \int_{z'} \tilde{G}(\beta, z, f | z') \tilde{g}(\beta, z', f) dz'}_{\tilde{B}(\beta, z, f)}$$

Where $\tilde{B}(\beta, z, f)$ represents the volumetric heat integral. The evaluation of this integral in each layer presents the final calculation to completely determine the heat flux distribution (which will be determined by continuity of the flux between layers) and the temperature distribution. Again, we must determine the expression for $\tilde{B}(\beta, z', f)$ for the five cases (two in the substrate, and three in the layers) for which we determined G.

A.2.5.1   Substrate.   The volume heat integral for the substrate takes the form:

$$B^{si}(\beta, z = 0, f) = \frac{\alpha}{\kappa} \int_0^\infty \tilde{G}^{si}(\beta, z, f | z') \tilde{g}(\beta, z', f) dz' \tag{91}$$

In his paper, Shih did not require a solution to this integral, which involves integrals of the error functions contained in $\tilde{G}$. Shih justified this omission because, in his problem, the substrate was non-absorbing, hence, no volume heating occurs. That is not the case in this problem. The GaAs which makes up the substrate in these structures will be highly absorbing at the wavelength we will be using. It is then desirable to have a solution to eqn 91 for the substrate. We can simplify the problem, however, because we are not really interested in the heat distribution in the substrate, because only the substrate/first layer reflection affects the reflectivity we are after. As a result, if we can obtain an expression for $B^{si}(\beta, z = 0, f)$ we can get the required values to complete our reflectivity calculations. If we do desire the heat/temperature distribution in the substrate, we can divide the substrate into as many "layers" as we want, and use the substrate material properties for these layers; then end with a substrate calculation as before.

Case 1: $a = 0$.   In this case, $\beta = 0$ and $f = 0$ so that $B^{si}(\beta, z, f)$ is:

$$B^{si}(\beta = 0, z, f = 0) \;=\; \frac{\alpha}{\kappa\sqrt{\pi\alpha}} \int_0^\infty \left[e^{-\frac{b_-^2}{t_G}} \sqrt{t_G} - (\sqrt{\pi}b_-)\mathrm{erfc}\left(\frac{b_-}{\sqrt{t_G}}\right) + \{b_+ \to b_-\} \right]$$

$$\times P_0 \Gamma(f = 0)\frac{2nk}{\lambda_0}\left[C_1 e^{-2\gamma z'} + C_2 e^{2\gamma z'} + C_3 \cos\left(\delta d - 2\delta z' + \phi\right)\right] dz'$$

(92)

... $\tilde{G}^{si}$ coming from eqn 66 and $\tilde{g}$ coming from eqn 90, with $\beta = 0$. Although we could now evaluate $\Gamma(f = 0) = t_r$ for the triangle-wave input intensity, it is left in this form, so that it is useful with any Fourier transformable input intensity waveform ($\chi(t)$). We can simplify this equation by recognizing that, in the substrate, there is no upward travelling wave, so that $E_-(z) = 0$, which makes $C_2 = 0$ and $C_3 = 0$, and $C_1 = |E_+(z = 0)|^2$. Additionally, for $z = 0$, $b_\pm = \frac{|z \pm z'|}{2\sqrt{\alpha}}$ reduces to $b_\pm = \frac{|\pm z'|}{2\sqrt{\alpha}}$, and, since the integral ranges from $0 < z' < \infty$, z' is always positive, so that $b_\pm = \frac{z'}{2\sqrt{\alpha}}$. Making these changes:

$$B^{si}(0, z, 0) \;=\; \frac{\sqrt{\alpha}}{\kappa\sqrt{\pi}} \int_0^\infty 2\left[e^{-\frac{z'^2}{4\alpha t_G}}\sqrt{t_G} - \frac{\sqrt{\pi}z'}{2\sqrt{\alpha}}\mathrm{erfc}\left(\frac{z'}{2\sqrt{\alpha t_G}}\right)\right]$$

$$\times P_0\Gamma(f = 0)\frac{2nk}{\lambda_0}\left[|E_+(z = 0)|^2 e^{-2\gamma z'}\right] dz'$$

$$\text{now letting: } \mathbb{A} = \frac{P_0\Gamma(f = 0)\sqrt{\alpha}}{\kappa\sqrt{\pi}}\frac{4nk}{\lambda_0}|E_+(z = 0)|^2 \quad \text{leaves :}$$

$$= \;\mathbb{A}\int_0^\infty \left[e^{-\frac{z'^2}{4\alpha t_G}}\sqrt{t_G} - \frac{\sqrt{\pi}z'}{2\sqrt{\alpha}}\mathrm{erfc}\left(\frac{z'}{2\sqrt{\alpha t_G}}\right)\right] e^{-2\gamma z'}dz'$$

$$= \;\mathbb{A}\left[\underbrace{\int_0^\infty e^{-\frac{z'^2}{4\alpha t_G}}\sqrt{t_G}\,e^{-2\gamma z'}dz'}_{\mathbb{I}_1} - \underbrace{\int_0^\infty \frac{\sqrt{\pi}z'}{2\sqrt{\alpha}}\mathrm{erfc}\left(\frac{z'}{2\sqrt{\alpha t_G}}\right)e^{-2\gamma z'}dz'}_{\mathbb{I}_2}\right] \quad (93)$$

Integrating $\mathbb{I}_1$ first:

$$\mathbb{I}_1 \;=\; \int_0^\infty e^{-\frac{z'^2}{4\alpha t_G}}\sqrt{t_G}\,e^{-2\gamma z'}dz' = \sqrt{t_G}\int_0^\infty e^{-\frac{z'^2}{4\alpha t_G} - 2\gamma z'}dz'$$

using integral formula (eqn $2.3.15.4$ vol 1, Prudnikov [40])

$$\int_0^\infty e^{-px^2 - qx}dx = \frac{1}{2}\sqrt{\frac{\pi}{p}}\exp\left(\frac{q^2}{4p}\right)\mathrm{erfc}\left(\frac{q}{2\sqrt{p}}\right) \qquad \cdots [\Re\{p\} > 0]$$

inserting $p = \frac{1}{4\alpha t_G}$, and $q = 2\gamma$, yields:

$$\mathbb{I}_1 = t_G\sqrt{\pi\alpha}\,\exp\left(4\gamma^2\alpha t_G\right)\,\mathrm{erfc}\left(2\gamma\sqrt{\alpha t_G}\right) \tag{94}$$

Now integrating $\mathbb{I}_2$:

$$\mathbb{I}_2 = \int_0^\infty \frac{\sqrt{\pi}z'}{2\sqrt{\alpha}}\mathrm{erfc}\left(\frac{z'}{2\sqrt{\alpha t_G}}\right)e^{-2\gamma z'}dz' = \frac{\sqrt{\pi}}{2\sqrt{\alpha}}\int_0^\infty z'\mathrm{erfc}\left(\frac{z'}{2\sqrt{\alpha t_G}}\right)e^{-2\gamma z'}dz'$$

integral formula (eqn 2.8.5.4 vol 2, Prudnikov [40])

$$\int_0^\infty x^n e^{-px}\mathrm{erfc}(cx)dx = -\frac{2c^2-p^2}{2c^2p^2}e^{\left(\frac{p^2}{4c^2}\right)}\mathrm{erfc}\left(\frac{p}{2c}\right)+\frac{1}{p^2}-\frac{1}{\sqrt{\pi}cp} \qquad \cdots [|\arg c| < \pi/4]$$

inserting $p = 2\gamma$, and $n = 1, c = \frac{1}{2\sqrt{\alpha t_G}}$, yields:

$$\mathbb{I}_2 = \frac{\sqrt{\pi}}{2\sqrt{\alpha}}\left\{\left[2\alpha t_G - \frac{1}{4\gamma^2}\right]e^{4\alpha t_G\gamma^2}\mathrm{erfc}\left(2\gamma\sqrt{\alpha t_G}\right)+\frac{1}{4\gamma^2}-\frac{\sqrt{\alpha t_G}}{\sqrt{\pi}\gamma}\right\} \tag{95}$$

Using eqns 94, 95, and substituting in for $\mathbb{A}$, we get:

$$B^{si}(0,z,0) = \frac{P_0\Gamma(f=0)\sqrt{\alpha}}{\kappa\sqrt{\pi}}\frac{4nk}{\lambda_0}|E_+(z=0)|^2\left[t_G\sqrt{\pi\alpha}\,\exp\left(4\gamma^2\alpha t_G\right)\,\mathrm{erfc}\left(2\gamma\sqrt{\alpha t_G}\right)\right]$$

$$-\frac{P_0\Gamma(0)\sqrt{\alpha}}{\kappa\sqrt{\pi}}\frac{4nk}{\lambda_0}|E_+(z=0)|^2\frac{\sqrt{\pi}}{2\sqrt{\alpha}}\left[\left[2\alpha t_G-\frac{1}{4\gamma^2}\right]e^{4\gamma^2\alpha t_G}\mathrm{erfc}\left(2\gamma\sqrt{\alpha t_G}\right)+\frac{1}{4\gamma^2}-\frac{\sqrt{\alpha t_G}}{\sqrt{\pi}\gamma}\right]$$

which reduces to:

$$= \frac{P_0\Gamma(0)\sqrt{\alpha}}{\kappa\sqrt{\pi}}\frac{4nk}{\lambda_0}|E_+(z=0)|^2\left[\frac{\sqrt{\pi}}{8\gamma^2\sqrt{\alpha}}e^{4\gamma^2\alpha t_G}\mathrm{erfc}\left(2\gamma\sqrt{\alpha t_G}\right)-\frac{\sqrt{\pi}}{8\gamma^2\sqrt{\alpha}}+\frac{\sqrt{t_G}}{2\gamma}\right]$$

So that:

$$B^{si}(0,z,0) = \frac{P_0\Gamma(0)nk}{\kappa\lambda_0}\frac{1}{2\gamma^2}|E_+(z=0)|^2\left[e^{4\gamma^2\alpha t_G}\mathrm{erfc}\left(2\gamma\sqrt{\alpha t_G}\right)-1+\frac{4\gamma\sqrt{\alpha t_G}}{\sqrt{\pi}}\right] \tag{96}$$

Case 2: $a \neq 0$. With $\tilde{G}^{si}$ coming from eqn 68 and $\tilde{g}$ from eqn 90, and the volume heat integral takes the form:

$$B^{si}(\beta,z,f) =$$

$$\frac{\alpha}{\kappa 4a\sqrt{\alpha}}\int_0^\infty\left\{e^{-2ab_-}\left[1+\mathrm{erf}\left(a\sqrt{t_G}-\frac{b_-}{\sqrt{t_G}}\right)\right]-e^{2ab_-}\mathrm{erfc}\left(a\sqrt{t_G}+\frac{b_-}{\sqrt{t_G}}\right)+\{b_-\to b_+\}\right\}$$

$$\times P_0\Gamma(f)\frac{2nk}{\lambda_0}e^{-\beta^2 r_h^2/4}\left[C_1 e^{-2\gamma z'}+C_2 e^{2\gamma z'}+C_3\cos\left(\delta d-2\delta z'+\phi\right)\right]dz'$$

121

simplifying as before: $b_{\pm} = \frac{z'}{2\sqrt{\alpha}}$, $C_2 = C_3 = 0$:

$$B^{si}(\beta, z, f) = \frac{\alpha P_0 \Gamma(f)}{\kappa a \sqrt{\alpha}} \frac{nk}{\lambda_0} |E_+(z=0)|^2 e^{-\beta^2 r_h^2/4} \int_0^\infty e^{-2\gamma z'}$$

$$\times \left\{ e^{-\frac{2az'}{2\sqrt{\alpha}}} \left[1 + \text{erf}\left(a\sqrt{t_G} - \frac{z'}{2\sqrt{\alpha t_G}} \right) \right] - e^{\frac{2az'}{2\sqrt{\alpha}}} \text{erfc}\left(a\sqrt{t_G} + \frac{z'}{2\sqrt{\alpha t_G}} \right) \right\} dz'$$

$$= \mathbb{B} \int_0^\infty e^{-2\gamma z'} \left\{ e^{-\frac{az'}{\sqrt{\alpha}}} \left[1 + \text{erf}\left(a\sqrt{t_G} - \frac{z'}{2\sqrt{\alpha t_G}} \right) \right] - e^{\frac{az'}{\sqrt{\alpha}}} \text{erfc}\left(a\sqrt{t_G} + \frac{z'}{2\sqrt{\alpha t_G}} \right) \right\} dz'$$

$$= \mathbb{B} \int_0^\infty e^{-(2\gamma + \frac{a}{\sqrt{\alpha}})z'} dz' + \mathbb{B} \int_0^\infty e^{-(2\gamma + \frac{a}{\sqrt{\alpha}})z'} \text{erf}\left(a\sqrt{t_G} - \frac{z'}{2\sqrt{\alpha t_G}} \right) dz'$$

$$- \mathbb{B} \int_0^\infty e^{-(2\gamma - \frac{a}{\sqrt{\alpha}})z'} \text{erfc}\left(a\sqrt{t_G} + \frac{z'}{2\sqrt{\alpha t_G}} \right) dz'$$

$$= \mathbb{B} \left[\mathbb{J}_1 + \mathbb{J}_2 - \mathbb{J}_3 \right] \tag{97}$$

Solving the integrals individually:

$$\mathbb{J}_1 = \int_0^\infty e^{-(2\gamma + \frac{a}{\sqrt{\alpha}})z'} dz' = \frac{1}{2\gamma + \frac{a}{\sqrt{\alpha}}} = \frac{\sqrt{\alpha}}{a + 2\gamma\sqrt{\alpha}} \tag{98}$$

$$\mathbb{J}_2 = \int_0^\infty e^{-(2\gamma + \frac{a}{\sqrt{\alpha}})z'} \text{erf}\left(a\sqrt{t_G} - \frac{z'}{2\sqrt{\alpha t_G}} \right) dz'$$

$$= -\int_0^\infty e^{-(2\gamma + \frac{a}{\sqrt{\alpha}})z'} \text{erf}\left(\frac{z'}{2\sqrt{\alpha t_G}} a\sqrt{t_G} - a\sqrt{t_G} \right) dz'$$

integral formula (eqn 2.8.9.1a vol 2, Prudnikov [40])

$$\int_0^\infty x^n e^{-px} \text{erf}(cx + b) dx =$$

$$(-1)^n \frac{\partial^n}{\partial p^n} \left[\frac{1}{p} \text{erf}(b) + \frac{1}{p} e^{\left(\frac{p^2 + 4pbc}{4c^2} \right)} \text{erfc}\left(b + \frac{p}{2c} \right) \right] \quad \ldots [\Re p > 0; \, |\arg c| < \pi/4] \tag{99}$$

inserting $n = 0$, $p = 2\gamma + \frac{a}{\sqrt{\alpha}}$, $b = a\sqrt{t_G}$, and $c = -\frac{1}{2\sqrt{\alpha t_G}}$

$$\mathbb{J}_2 = \frac{\sqrt{\alpha}}{2\gamma\sqrt{\alpha} + a} \left[\text{erf}(a\sqrt{t_G}) + \exp\left(t_G \left(4\gamma^2\alpha - a^2 \right) \right) \text{erfc}(2\gamma\sqrt{t_G\alpha}) \right] \tag{100}$$

$$\mathbb{J}_3 = \int_0^\infty e^{-(2\gamma - \frac{a}{\sqrt{\alpha}})z'} \text{erfc}\left(a\sqrt{t_G} + \frac{z'}{2\sqrt{\alpha t_G}} \right) dz'$$

integral formula (eqn 2.8.9.1b vol 2, Prudnikov [40])

$$\int_0^\infty x^n e^{-px} \text{erfc}(cx + b) dx =$$

$$(-1)^n \frac{\partial^n}{\partial p^n} \left[\frac{1}{p} \text{erfc}(b) - \frac{1}{p} e^{\left(\frac{p^2 + 4pbc}{4c^2} \right)} \text{erfc}\left(b + \frac{p}{2c} \right) \right] \quad \ldots [\Re p > 0; \, |\arg c| < \pi/4]$$

inserting $n = 0$, $p = 2\gamma - \frac{a}{\sqrt{\alpha}}$, $b = a\sqrt{t_G}$, and $c = \frac{1}{2\sqrt{\alpha t_G}}$

$$\mathbb{J}_3 = \frac{\sqrt{\alpha}}{2\gamma\sqrt{\alpha} - a} \left[\text{erfc}(a\sqrt{t_G}) - \exp\left(t_G \left(4\gamma^2\alpha - a^2 \right) \right) \text{erfc}(2\gamma\sqrt{\alpha t_G}) \right] \quad \ldots [2\gamma > \frac{a}{\sqrt{\alpha}}] \tag{101}$$

122

If $2\gamma < \frac{a}{\sqrt{\alpha}}$, we can still get an analytic solution to the integral, but need to manipulate it slightly. Since $2\cosh(bx) - e^{-bx} = e^{bx}$ we can use:

$$
\begin{aligned}
\mathbb{J}_3 &= \int_0^\infty \left[2\cosh\left(\left(\frac{a}{\sqrt{\alpha}} - 2\gamma\right)z'\right) - e^{-\left(\frac{a}{\sqrt{\alpha}} - 2\gamma\right)z'} \right] \mathrm{erfc}\left(a\sqrt{t_G} + \frac{z'}{2\sqrt{\alpha t_G}}\right) dz' \\
&= \int_0^\infty 2\cosh\left(\left(\frac{a}{\sqrt{\alpha}} - 2\gamma\right)z'\right) \mathrm{erfc}\left(a\sqrt{t_G} + \frac{z'}{2\sqrt{\alpha t_G}}\right) dz' \\
&\qquad - \int_0^\infty e^{-\left(\frac{a}{\sqrt{\alpha}} - 2\gamma\right)z'} \mathrm{erfc}\left(a\sqrt{t_G} + \frac{z'}{2\sqrt{\alpha t_G}}\right) dz'
\end{aligned}
$$

we can now use the integral formula above on the second integral,

and (eqn $2.8.15.4b$ vol 2, Prudnikov [40]) on the first

$$
\int_0^\infty \cosh(px)\mathrm{erfc}(cx+b)dx = \frac{1}{2p}e^{\left(\frac{p^2}{4c^2}\right)}\left[-e^{bp/c}\mathrm{erfc}\left(b + \frac{p}{2c}\right) + e^{-bp/c}\mathrm{erfc}\left(b - \frac{p}{2c}\right)\right] \quad \cdots [|\arg c| < \pi/4]
$$

with $p = \frac{a}{\sqrt{\alpha}} - 2\gamma$, $b = a\sqrt{t_G}$, and $c = \frac{1}{2\sqrt{\alpha t_G}}$, inserting these, and solving

the second integral (replace $p \to -p$ in eqn 99) and subtracting:

$$
\mathbb{J}_3 = \frac{\sqrt{\alpha}}{2\gamma\sqrt{\alpha} - a}\left[\mathrm{erfc}(a\sqrt{t_G}) - e^{\left[t_G\left(4\gamma^2\alpha - a^2\right)\right]}\mathrm{erfc}(2\gamma\sqrt{\alpha t_G})\right]
$$

... which is the same as eqn 101, a fortunate result, which we could have derived from the two integral formulas, upon retrospect. Using some algebra we can combine the three results, so that:

$$
[\mathbb{J}_1 + \mathbb{J}_2 - \mathbb{J}_3] = \frac{2\sqrt{\alpha}}{4\gamma^2\alpha - a^2}\left[2\gamma\sqrt{\alpha}\left(\mathrm{erf}(a\sqrt{t_G}) + e^{t_G(4\gamma^2\alpha - a^2)}\mathrm{erfc}(2\gamma\sqrt{t_G\alpha})\right) - a\right]
$$

so we can form eqn 97 by inserting this equation and $\mathbb{B}$ to produce the solution for $B^{si}(\beta, z, f)$ for $\beta \neq 0$ and/or $f \neq 0$.

$$
\begin{aligned}
B^{si}(\beta, z, f) &= \frac{\alpha P_0 \Gamma(f)}{\kappa a}\frac{2nk}{\lambda_0}|E_+(z=0)|^2 e^{-\beta^2 r_h^2/4}\frac{1}{4\gamma^2\alpha - a^2} \\
&\qquad \times \left[2\gamma\sqrt{\alpha}\left(\mathrm{erf}(a\sqrt{t_G}) + e^{t_G(4\gamma^2\alpha - a^2)}\mathrm{erfc}(2\gamma\sqrt{t_G\alpha})\right) - a\right] \quad (102)
\end{aligned}
$$

A.2.5.2   Mirror Layers.   The last set of integrals before the calculations can be done determines the volumetric heat generation in the mirror layers. The solution for the layers takes the

same form (eqn 91) as that of the substrate:

$$B^l(\beta, z, f) = \frac{\alpha}{\kappa} \int_0^d \tilde{G}^l(\beta, z, f | z') \tilde{g}(\beta, z', f) dz'$$

The integrals in this case are less exotic, thankfully, than the substrate. The integration limits are those of the layer ($0 < z' < d$), where d is defined for each layer. Again, in this convention, also used by Shih [42] and McGahan [34], the top of the layer is at $z = 0$.

Case 1: $\beta = 0$ and $f = 0$.   In this case, $a = 0$ so that $B^l(\beta, z, f)$ is:

$$
\begin{aligned}
B^l(\beta = 0, z, f = 0) \quad = \quad & \frac{\alpha}{\kappa d} \int_0^d \left[t_G + 2 \sum_{m=1}^\infty \cos\left(\frac{m\pi z}{d}\right) \cos\left(\frac{m\pi z'}{d}\right) \frac{1 - e^{-(\alpha \pi^2 m^2/d^2) t_G}}{\alpha \pi^2 m^2/d^2} \right] \\
& \times P_0 \Gamma(f = 0) \frac{2nk}{\lambda_0} \left[C_1 e^{-2\gamma z'} + C_2 e^{2\gamma z'} + C_3 \cos\left(\delta d - 2\delta z' + \phi\right) \right] dz'
\end{aligned}
$$

... $\tilde{G}^l$ coming from eqn 71 and $\tilde{g}$ coming from eqn 90, with $\beta = 0$. We now have counter-propagating waves, so we must retain C_1, C_2 and C_3, unlike in the substrate analysis. Separating into two integrals:

$$
\begin{aligned}
B^l(\beta = 0, z, f = 0) \quad = \quad & \frac{\alpha}{\kappa d} P_0 \Gamma(0) \frac{nk}{2\pi \lambda_0} t_G \int_0^d \left[C_1 e^{-2\gamma z'} + C_2 e^{2\gamma z'} + C_3 \cos\left(\delta d - 2\delta z' + \phi\right) \right] dz' \\
& + \frac{\alpha}{\kappa d} P_0 \Gamma(0) \frac{2nk}{\lambda_0} 2 \sum_{m=1}^\infty \cos\left(\frac{m\pi z}{d}\right) \frac{1 - e^{-(m^2 \pi^2 \alpha/d^2) t_G}}{m^2 \pi^2 \alpha/d^2} \int_0^d \cos\left(\frac{m\pi z'}{d}\right) \\
& \qquad \left[C_1 e^{-2\gamma z'} + C_2 e^{2\gamma z'} + C_3 \cos\left(\delta d - 2\delta z' + \phi\right) \right] dz'
\end{aligned}
$$

Letting $\mathbb{A}_1 = \frac{\alpha}{\kappa d} P_0 \Gamma(f) \frac{2nk}{\lambda_0}$ and $\mathbb{A}_2 = \frac{\alpha}{\kappa d} P_0 \Gamma(f) \frac{2nk}{\lambda_0} 2 \sum_{m=1}^\infty \cos\left(\frac{m\pi z}{d}\right) \frac{1 - e^{-(\alpha \pi^2 m^2/d^2) t_G}}{\alpha \pi^2 m^2/d^2}$ we have:

$$
\begin{aligned}
B^l(0, z, 0) \quad = \quad & \mathbb{A}_1 t_G \int_0^d \left[C_1 e^{-2\gamma z'} + C_2 e^{2\gamma z'} + C_3 \cos\left(\delta d - 2\delta z' + \phi\right) \right] dz' \\
& + \mathbb{A}_2 \int_0^d \cos\left(\frac{m\pi z'}{d}\right) \left[C_1 e^{-2\gamma z'} + C_2 e^{2\gamma z'} + C_3 \cos\left(\delta d - 2\delta z' + \phi\right) \right] dz' \quad (103)
\end{aligned}
$$

None of the integrals in eqn 103 are difficult. The result is:

$$B^l(0,z,0) = \frac{2nkP_0}{\lambda_0\kappa d}\Gamma(f=0)\alpha\left[\mathbb{C}_1 t_G + 2\sum_{m=1}^{\infty}\mathbb{C}_m\cos{(m\pi z/d)}\frac{1-e^{-(\alpha\pi^2 m^2/d^2)t_G}}{\alpha\pi^2 m^2/d^2}\right] \tag{104}$$

where:

$$\mathbb{C}_1 = \frac{C_1}{2\gamma}\left[1-e^{-2\gamma d}\right] + \frac{C_2}{2\gamma}\left[e^{2\gamma d}-1\right] + \frac{C_3}{\delta}\sin{(\delta d)}\cos{(\phi)}$$

$$\mathbb{C}_m = \frac{2\gamma}{4\gamma^2 + m^2\pi^2/d^2}\left\{C_1\left[1-(-1)^m e^{-2\gamma d}\right] + C_2\left[(-1)^m e^{2\gamma d}-1\right]\right\}$$

$$+ C_3\left(\frac{4\delta}{4\delta^2 - m^2\pi^2/d^2}\right)\times\left\{\begin{array}{ll}\sin{(\delta d)}\cos{(\phi)} & m = \text{even} \\ \cos{(\delta d)}\sin{(\phi)} & m = \text{odd}\end{array}\right\} \tag{105}$$

The development of the integrals for $B^l(\beta = 0, z, f \neq 0)$ and $B^l(\beta \neq 0, z, f \neq 0)$ are similar. The results of these are:

$$B^l(0,z,f) = \frac{2nkP_0}{\lambda_0\kappa d}\Gamma(f)\alpha$$

$$\times\left[\mathbb{C}_1 t_G e^{-j\pi f t_G}\text{sinc}(\pi f t_G) + 2\sum_{m=1}^{\infty}\mathbb{C}_m\cos{(m\pi z/d)}\frac{1-e^{-(j2\pi f + \frac{\alpha\pi^2 m^2}{d^2})t_G}}{j2\pi f + \frac{\alpha\pi^2 m^2}{d^2}}\right] \tag{106}$$

and:

$$B^l(\beta,z,f) = \frac{2nkP_0\Gamma(f)e^{-\beta^2 r_h^2/4}}{\lambda_0\kappa d}\alpha$$

$$\times\left[\mathbb{C}_1\frac{1-e^{-a^2 t_G}}{a^2} + 2\sum_{m=1}^{\infty}\mathbb{C}_m\cos{(m\pi z/d)}\frac{1-e^{-(a^2 + \frac{\alpha\pi^2 m^2}{d^2})t_G}}{a^2 + \frac{\alpha\pi^2 m^2}{d^2}}\right] \tag{107}$$

125

Appendix B. **Equipment Specifications**

The configuration for thermal bistability experiments is shown in figure 18, and for the carrier generated measurements in figure 52. Equipment used are listed in table 4 below

Table 4. Relevant Equipment Specifications for Thermal Bistability Measurements

Ar^+ Laser	Model	Coherent Innova 400
	Wavelength	Multi-Line Visible Spectrum (MLVS)
	Output Power	30 W(max)
TiS Laser	Model	Coherent Mira 900
	Wavelength	Tunable 780 - 930 nm
	Avg Output Power(CW)	3 W(max)
	Fsec Pulsewidth	<200 fsec (avg power 1.1 W)
	Fsec Peak Power	111 kW
	Psec Pulsewidth	<2 psec (avg power 1.3 W)
	Psec Peak Power	8.8 kW
	Repetition Rate	76 MHz
	Beam Diameter	0.8 mm
	Beam Mode	TEM_{00} Horizontally Polarized
	Beam Divergence	1.5 mrad
Optical Multichannel Analyzer	Mfr	EG & G
	Monochromator	Jarrell Ash Monospec 27
	Detector Array	EG & G 1453A Silicon Diode Detector Array
	Grating 1	1200 grooves/mm
	Resolution	3 $\overset{\circ}{A}$
	Wavelength Range	$\sim 600 - 1000$ nm
	Grating 2	600 grooves/mm Blaze 600 nm
	Resolution	6 $\overset{\circ}{A}$
	Wavelength Range	$\sim 600 - 1100$ nm
Optical Isolator	Model	Optics for Research Model IO-5-TIS2
	Input Power	150 $MWcm^2$/20 nsec pulse
	Bandwidth	Tunable
Pulse Picker	Model	Conoptics Model 350-160
	Counter	Conoptics Model 305
	Voltage Driver	Conoptics Model 35D
	Pulse Rejection	200:1
	Pulse Selection	single pulse 1:2 to $1:10^7$, or gated
	Jitter	<100 psec
Detector	Model	EG & G model FND-100
	Rise time	1 nsec
	Wavelength range	300-1100 nm

Table 5. Relevant Equipment Specifications for Thermal Bistability Measurements(cont)

Autocorrelator	Model	Inrad model 514BX
	Crystal	KDP @ 45º
	Wavelength range	700-1000 nm
Acousto-Optic Modulator	Model	Intraction model AOM 40N
	Signal Processor	Intraction model ME
	RF out	40 MHz (AM or CW), 5 W max
	Modulation Input	10 MHz (max), 1 V_{peak}
Function Generator	Model	HP model 33120A
	Output	50 mV - 10V_{p-p}
	Arb Waveform Freq	to 200 kHz
	Arb Waveform Resolution	to 16k points
Translation Stage	Model	Linetool model 102 RH
	Resolution	0.1 μm
Delay Stage	Model	Klinger MD4 Motor Driver
	Translation Stage	Microcontrole model MT 160-250-1μ
	(Motorized)	
	Resolution	0.1 μm
Power Meter	Model	Coherent Fieldmaster
	Detector	LM-2 Silicon Sensor
Focusing Lens	Mfr	Melles Griot
	f_0	14.5 mm
	Spot size	2.75 μm
	Working distance	6.7 mm
Polarizing Beamsplitters	Model	Newport model 10FC16PB.5
	Glass	SF.2
Turning Mirrors	Model	New Focus model 5103 (silver)
Beamsplitter	Model	Melles Griot model 03BTF033 (70/30)
		Melles Griot model 03BTF033 (50/50)

Bibliography

1. Acklin, B., et al. "Bistable switching in a nonlinear Bragg reflector," *Applied Physics Letters*, *63*(16):2177–79 (October 1993).

2. Adachi, S. "GaAs, AlAs, and $Al_xGa_{1-x}As$: Material parameters for use in research and device applications," *Journal of Applied Physics*, *58*(23):R1–R29 (August 1985).

3. Afromowitz, M. A. "Refractive Index of $Ga_{1-x}Al_xAs$," *Solid State Communications*, *15*:59–63 (1974).

4. Babic, D. I. and S. W. Corzine. "Analytic Expression for the Reflection Delay, Penetration Depth, and Absorptance of Quarter-Wave Dielectric Mirrors," *IEEE Journal of Quantum Electronics*, *28*(2):514–524 (February 1992).

5. Beck, J. V., et al. *Heat Conduction Using Green's Functions.* New York: Hemisphere, 1992.

6. Brice, J. C. *Properties of Gallium Arsenide.* London: INSPEC, 1986.

7. Brown, S. L. *Characterization of Nonlinear Effects in Optically Pumped Vertical Cavity Surface Emitting Lasers*. MS thesis, Air Force Institute of Technology, 1993.

8. Casey, H. C. and M. B. Panish. *Heterostructure Lasers, Part A: Fundamental Principles.* Quantum Electronics: Principles and Applications, Orlando: Academic Press, Inc., 1978.

9. Chen, H. C. *Theory of Electromagnetic Waves.* New York: McGraw-Hill, 1983.

10. Crook, A. W. "The Reflection and Transmission of Light by Any System of Parallel Isotropic Films," *Journal of the Optical Society of America*, *38*(11):954–964 (November 1948).

11. Dudley, J. J., et al. "Temperature Dependence of the Properties of DBR Mirrors Used in Surface Normal Optoelectronic Devices," *IEEE Photonics Technology Letters*, *4*(4):311–314 (April 1992).

12. Dumke, W. P. "Optical Transitions Involving Impurities in Semiconductors," *Physical Review*, *132*(5):1998–2002 (December 1963).

13. Erdélyi, A., editor. *Tables of Integral Transforms*, *II*. New York: McGraw-Hill, Inc., 1954.

14. Gaskill, J. D. *Linear Systems, Fourier Transforms, and Optics*. New York: John Wiley & Sons, 1978.

15. Gibbs, H. M. *Optical Bistability: Controlling Light with Light.* Quantum Electronics-Principles and Applications, Orlando, Fla.: Academic Press, Inc., 1985.

16. Gibbs, H. M., et al. "Optical bistability in semiconductors," *Applied Physics Letters*, *35*:451–53 (1979).

17. Grosse, P. and R. Wynands. "Simulation of Photoacoustic IR Spectra of Multilayer Structures," *Applied Physics B*, *48*:59–65 (1989).

18. Haug, H., editor. *Optical Nonlinearities and Instabilities in Semiconductors.* Boston: Academic Press, Inc, 1988.

19. He, J. and M. Cada. "Optical Bistability in Semiconductor Periodic Structures," *IEEE Journal of Quantum Electronics*, *27*(5):1182–1188 (May 1991).

20. Hultgren, C. T. *FemtoSecond Nonlinearities in AlGaAs Diode Laser Amplifiers.* PhD dissertation, Massachusetts Institute of Technology, 1994.

21. Jackson, J. D. *Classical Electrodynamics* (2nd Edition). New York: John Wiley & Sons, 1975.

22. Jenkins, D. W. "Optical Constants of $Al_xGa_{1-x}As$," *Journal of Applied Physics*, *68*(4):1848–52 (August 1990).

23. Karin, J. R., et al. "Generation of picosecond pulses with a gain-switched GaAs surface-emitting laser," *Applied Physic Letters*, *57*(10):963–965 (September 1990).

24. Koyama, F., et al. "1.5-1.6 μm GaInAsP/InP dynamic-single-mode (DSM) lasers with distributed Bragg reflector," *IEEE Journal of Quantum Electronics*, *QE-19*:1042–1051 (June 1983).

25. Kuszelewicz, et al. "Monolithic GaAs/AlAs optical bistable etalons with improved switching characteristics," *Applied Physics Letters*, *53*(22):2138–2140 (November 1988).

26. Lasher, G. and F. Stern. "Spontaneous and Stimulated Recombination Radiation in Semiconductors," *Physical Review*, *133*(2a):a553–a563 (1964).

27. Lasher, G.J. "Analysis of a proposed bistable injection laser," *Solid State Electronics*, *7*:707–716 (1964).

28. Lax, M. *Laser Solid Interactions and Laser Processing*, 149. New York: American Institute of Physics, 1978.

29. Lax, M. "Temperature rise induced by a laser beam II. The nonlinear case," *Applied Physics Letters*, *33*(8):786–788 (October 1978).

30. Lu, Yong-Feng. "Laser-induced temperature distribution in substrates with periodic multilayer structures," *Journal of Applied Physics*, *74*(9):5761–5766 (November 1993).

31. MacLeod, H.A. *Thin Film Optical Filters* (2nd Edition). New York: MacMillan Publishing Company, 1986.

32. Maracas, G. N. "Unpublished Ellipsometry Measurements of the Temperature Variation of the Optical Constants for GaAs." August 1994.

33. McCall, S. L., et al. *Technical Digest of the Conference on Lasers and Electro-Optics (CLEO).* 364. 1986.

34. McGahan, W.A. and K.D. Cole. "Solutions of the heat conduction equation in multilayers for photothermal deflection experiments," *Journal of Applied Physics*, *72*(4):1362–1373 (August 1992).

35. Moody, J. E. and R. H. Hendel. "Temperature profiles induced by a scanning cw laser beam," *Jorunal of Applied Physics*, *53*(6):4364–4371 (June 1982).

36. Nathan, M.I., et al. "GaAs injection laser with novel mode control and switching properties," *Journal of Applied Physics*, *36*(2):473–480 (February 1965).

37. Newell, A.C. and J.V. Moloney. *Nonlinear Optics*. Advanced Topics in Interdisciplinary Mathematical Sciences, Redwood City, CA: Addison-Wesley Publishing Company, 1992.

38. Palik, E. D. *Handbook of Optical Constants of Solids*. Orlando: Academic Press, 1985.

39. Pankove, J. I. *Optical Processes in Semiconductors*. New York: Dover Publications, Inc, 1971.

40. Prudnikov, A. P., et al. *Integrals and Series*, *1,2*. New York: Gordon and Breach Science Publishers, 1986.

41. Sheik-Bahae, M., et al. "Dispersion of Bound Electronic Nonlinear Refraction in Solids," *IEEE Journal of Quantum Electronics*, *27*(6):1296–1308 (June 1991).

42. Shih, O. W. "A multilayer heat conduction solution for magneto-optical disk recording," *Journal of Applied Physics*, *75*(9):4382–4395 (May 1994).

43. Wemple, S. H. and Jr. M. DiDomenico. "Behavior of the Electronic Dielectric Constant in Covalent and Ionic Materials," *Physical Review B*, *3*(4):1338–1351 (February 1971).

44. Winful, H. G., et al. "Theory of bistability in nonlinear distributed feedback structures," *Applied Physics Letters*, *35*(5):379–81 (September 1979).

45. Yamada, M. "Temperature Distributions Produced in Multilayer Structures by a Scanning CW Laser Beam," *Japanese Journal of Applied Physics*, *30*(7):1418–1427 (July 1991).

46. Yamada, M., et al. "Nonlinear calculation of a temperature profile produced in a two layer structure by a scanning cw elliptical laser or electron beam," *Journal of Applied Physics*, *57*(3):965–967 (February 1985).

47. Yariv, A. *Optical Electronics* (3rd Edition). New York: Holt, Rinehart, and Winston, 1985.

Vita

Major Richard J. Bagnell graduated from Raritan High School, Hazlet, N.J. in 1977. He received a Bachelor of Arts degree in Physics from the College of St. Thomas in St. Paul, Minnesota in 1982 on a Reserve Officers Training Corps scholarship. After commissioning, his first assignment was in the Air Force Institute of Technology's Undergraduate Engineering Conversion Program at the University of New Mexico. He graduated from UNM in 1984 with a Bachelor of Science degree in Electrical Engineering. Next assigned to the 6906th Electronic Security Squadron, Electronic Security Command, at Brooks AFB, TX, he was a project officer involved in planning, performing, and reporting on TEMPEST evaluations of Air Force mission critical equipments. TEMPEST is the unclassified term for the study of electromagnetic emanations from classified processing equipments. He then transferred to Hanscom AFB Massachusetts, where he led the test integration effort for the Space and Missile Warning System Program Office. Major Bagnell entered the Air Force Institute of Technology in May of 1991 and received his Master of Science in Electrical Engineering in December 1992. He was subsequently extended into the Doctoral program. His next assignment will be at Phillips Laboratory PL/LI, Kirtland AFB, NM.

Major Bagnell is a member of the Eta Kappa Nu and Tau Beta Pi engineering Societies

Permanent address: 75A Amherst Lane
Jamesburg, NJ 08831